Computational methods for designing semiconductor quantum dot devices

Jacob Manalo

Supervisor: Prof. Pawel Hawrylak

Thesis submitted to
the University of Ottawa
in partial fulfilment of the requirements
for the Doctoral Degree in Physics

Department of Physics
Faculty of Sciences
University of Ottawa

To my son Ino and my wife Mariam,

And to my mother Josie and father Pino.

Abstract

Quantum computers have the potential to solve certain problems in minutes that would otherwise take classical computers thousands of years due to the exponential speed-up certain quantum algorithms have over classical algorithms. In order to leverage such quantum algorithms, it is necessary for them to run on quantum devices. Examples of such devices include, but are not limited to, semiconductor and superconducting qubits, and semiconductor single and entangled photon emitters.

The conventional method of constructing a semiconductor qubit is to apply gates on a semiconductor surface to localize electrons, where the electronic spin states are mapped to a qubit basis. Examples of this include the spin qubit were the spin-$\frac{1}{2}$ states of a single electron is the qubit basis and the gated singlet-triplet qubit where the states of two coupled electrons are mapped to a qubit basis [1, 2]. In general, gated semiconductor spin qubits are subject to decoherence from the environment which alters the electronic wavefunction by entanglement with the nuclear spins and phonons in the lattice compromising the stability of the qubit.

Semiconductor nanostructures can also be designed as photon emitters. Self-assembled quantum dots are an example of such nanostructures and have been shown to emit single photons through exciton recombination and entangled photons through biexciton-exciton cascade. The difficulty in designing photon sources using self-assembled quantum dots is that the size and shape varies from dot to dot implying that the electronic and magnetic properties also vary.

In this thesis, I present the design of a single photon emitter using an InAsP quantum dot embedded in an InP nanowire and the design of a singlet-triplet qubit

that is topologically protected from decoherence using an array of such quantum dots embedded in an InP nanowire. The advantage of using quantum dot nanowires over self-assembled quantum dots as photon emitters is that the quantum dot thickness, radius and composition can be controlled deterministically using a technique known as vapour-liquid-solid epitaxy which allows the emission spectrum to be engineered. Using a microscopic model, I simulated an InAsP quantum dot embedded in a nanowire with upwards of millions of atoms and showed that the emission spectrum came in agreement with the actual InAsP/InP quantum dot nanowires that were fabricated at the National Research Council of Canada. Moreover, I showed that altering the distribution of As atoms in the quantum dot can cause dramatic change in the emission spectrum. For the design of the topologically protected singlet-triplet qubit, I demonstrated that the ground state of an array of such quantum dots embedded in an InP nanowire, with four electrons in each dot, is four-fold degenerate and is topologically protected from higher energy states, making the ground state robust against perturbations. This state is known as the Haldane phase and can be understood in terms of two spin-$\frac{1}{2}$ quasiparticles at each edge of the array. Though the spectral gap in my simulation was of the order of 1 meV, this work provides insight into the potential design of a room temperature operating Haldane qubit where the spectral gap is of the order of room temperature.

Acknowledgements

First, I would like to thank my advisor, Prof. Pawel Hawrylak for providing guidance and understanding throughout my journey in graduate studies. He has formed a great part of my scientific thinking by enforcing a high level of rigor and skepticism which I will carry with me for the rest of my life and in many areas outside of physics. He has also been compassionate of the family situations of his graduate students being a family oriented person himself, which I appreciate invaluably.

I also give special thanks to my colleagues Abdulmenaf Altintas, Daniel Miravet and Yasser Saleem. Abdulmenaf is a reliable research partner and post-doc who helped me write my first two papers. In addition to being helpful with the technical parts of the research, his wisdom of the life of an academic has always provided me insight as well as assurance at times when I needed it. Daniel Miravet has worked with me for the latter part of my PhD career. I cannot thank him enough for his exemplary skills as a researcher and his sense of teamwork; he always knew what I needed and when. Working with Daniel was a pleasure and I sincerely hope to work with him in the future. Although I have not worked on a project with Yasser Saleem, he has been a great friend throughout my academic journey in this research group. He really makes the research group feel like a family and without him, my graduate studies would not be nearly as enjoyable.

I would like to thank my mother Josefina Manalo and father Josefino Manalo for their unlimited and unconditional support. From childhood, my mother always encouraged my creative pursuits; she even let me draw on the walls! As for my father, throughout his life he has instilled in me a strong work ethic and the ability

to persevere through the toughest of times. He has and always will be a guiding force in my life.

Next, I would like to thank my wife Mariam Al-Ansary for her immense support. She has always believed in me, even when I did not believe in myself. I cannot thank her enough for the sacrifices she has made in order for me to study. Finally, I would like to thank my son Josefino Manalo for being my inspiration.

Abbreviations

CI	Configuration interaction
DFT	Density functional theory
DMRG	Density matrix renormalization group
MPO	Matrix product operator
MPS	Matrix product state
SVD	Singular value decomposition
TB	Tight-binding
TMD	Transition metal dichalcogenide

Contents

List of Figures

List of Tables

Chapter 1

Introduction

Quantum computing is about engineering quantum mechanical systems to process information. There are certain problems that a quantum computer can solve potentially in minutes that a classical computer with the same number of bits would take thousands of years to solve due to the exponential speed-up quantum algorithms offer. Examples of such algorithms are Shor's prime factoring algorithm which is a quantum algorithm that finds the prime factors of a given number and Grover's search algorithm which searches for a binary string x such that $f(x) = 1$ where $f(x)$ is an oracle. Quantum computers are necessary for running quantum algorithms such as the ones aforementioned. An ensamble of many different quantum devices, examples of which could be semiconductor qubits and photon emitters, are the components that make up a quantum computer. In order to produce such devices, experimental methods are necessary for fabrication and computational methods are necessary for design. This work will focus on the design of quantum devices using InAsP quantum dots embedded in an InP nanowire and the computational techniques used in the design. The first device is a single photon emitter made of a single quantum dot in a nanowire and the second device is a topologically protected singlet-triplet qubit made of an array of quantum dots filled with electrons in a nanowire.

1.1 InAsP Quantum Dots in a Nanowire

The InP/InAsP quantum dot nanowire nanostructure shows potential as a quantum information processing and quantum communication device in part due to the wavelength of photon emission being in the telecom range at ∼1.5 μm [3–6]. Fig.1.1(a) shows a schematic of the quantum dot nanowire. Here, the quantum dot, illustrated in blue, is of a hexagonal disc-like structure and is embedded in the centre of the nanowire which is illustrated in yellow. Fig.1.1(b) shows a TEM picture of the InP/InAsP quantum dot nanowire, which was fabricated at the National Research Council of Canada. This TEM photograph was taken from Ref. [3].

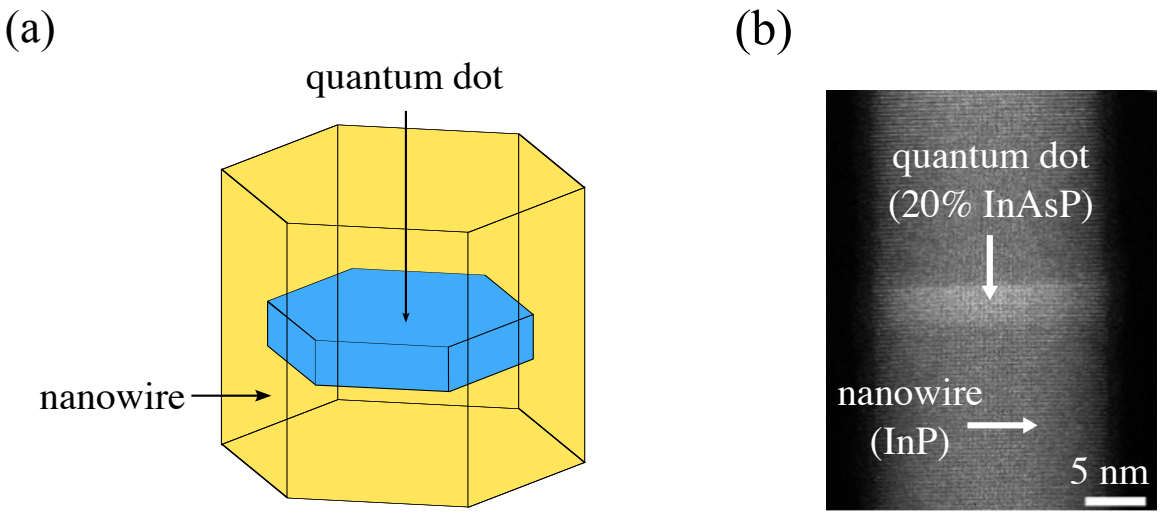

Figure 1.1: (a) Schematic of a semiconductor quantum dot embedded in a nanowire. Quantum dot is in blue and the nanowire is in yellow. (b) A transmission electron microscopy (TEM) photo of an InAsP quantum dot in an InP nanowire fabricated in the National Research Council of Canada. Photo was taken from Ref. [3]

.

Though there are many different types of semiconductor quantum dots that show promise as devices for quantum information processing and quantum communication such as lens shaped self assembled quantum dots and gate confining quantum dots [7–10], the advantage of InAsP quantum dots embedded in an InP nanowire is that the radius, height and composition of the quantum dots are well controlled [3, 11, 12]. This in turn allows for the control of the emission spectrum since the height of the quantum dot controls the spacing of the conduction band energies due to quantum

confinement [4], the radius and As concentration controls the band gap [4], and the distribution of As controls the ordering of the emission lines [3, 4]. This level of control is especially useful in engineering single and entangled photon emitters since the emission of a single photon comes from the recombination of an exciton and the emission of entangled photons comes from the biexciton-exciton cascade [11, 13, 14].

Furthermore, these quantum dot nanowires exhibit the behaviour of single atoms. As shown in Fig.1.2, the charge distribution of the conduction band states of an InAsP quantum dot exhibit distinct s and p like shell structure, making these structures viable candidates for quantum information processing since having well defined electronic energy levels can provide a means to process quantum information. For example, a basis comprised of linear combinations of many-electron configurations on these well defined single electron energy levels could in principle be mapped to a logical qubit basis.

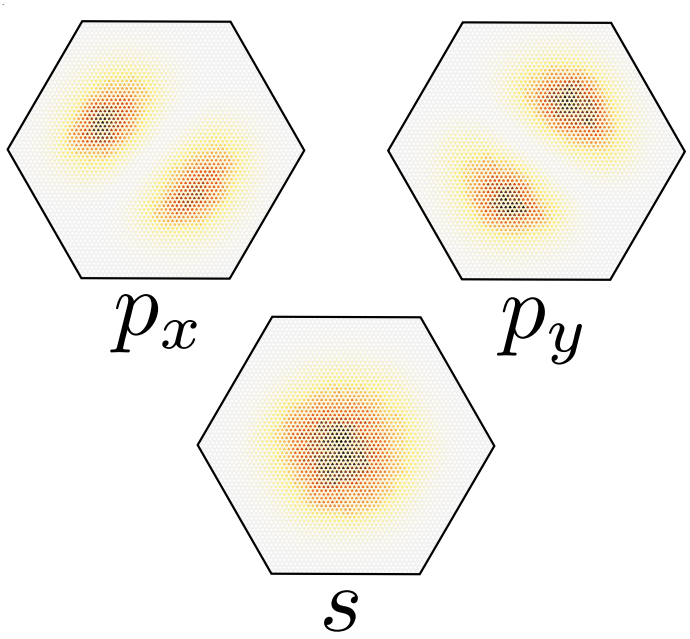

Figure 1.2: Top view of the charge distribution of conduction band levels of InAsP quantum dot.

In principle, a qubit can be made with an array of quantum dots in a nanowire as shown in Fig.1.3 [15, 16].

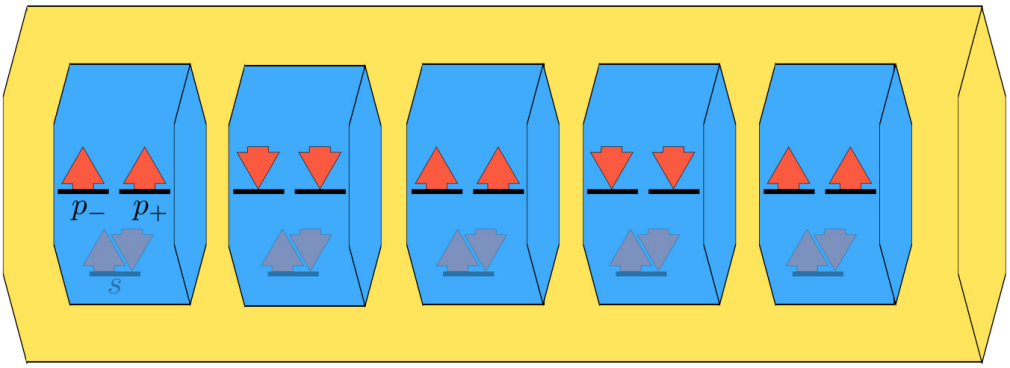

Figure 1.3: Schematic of an array on InAsP quantum dots (blue) in an InP nanowire (yellow). The red arrows represent spin up and spin down electrons and the black lines represent the quantum dot orbitals. The translucence of the electrons on the s shell indicate that those electrons are "frozen" and do not couple to any other conduction band levels.

Here, 4 electrons are injected into each quantum dot. Two of the electrons reside in the s shell and do not couple to any other conduction band states leaving the remaining two electrons on the p shells to couple ferromagnetically and form a synthetic spin-1 object. It has been proposed that a synthetic chain of spin-1 objects can be constructed using an array of these quantum dots [5, 15, 16].

Haldane as well as Affleck, Kennedy, Lieb and Tasaki demonstrated that a chain of spin-1 particles has a four-fold degenerate ground state that is robust to perturbations, i.e. is topologically protected, because of a finite energy gap separating the ground state from higher energy states [17, 18]. The existence of the edge states implies that this state is topologically nontrivial. Due to the stability of the four-fold degenerate ground state, this system can be made to be a qubit where the qubit basis consists of the singlet and triplet states. This four-fold degenerate ground state can be understood in terms of two spin-$\frac{1}{2}$ quasiparticles at the edges of the chain forming degenerate singlet and triplet states. In the next section I will discuss how this topological phase, which is characterized by the existence of edge spin-1/2 quasiparticles and a spectral gap, arises from a chain of spin-1 particles with nearest neighbour coupling.

1.2 Heisenberg Spin-1 Chain and the Haldane Phase

In order to understand the properties of a chain of spin-1 particles, it is important to understand the spectrum of two spin-$\frac{1}{2}$ particles. The Hamiltonian for two coupled spin-$\frac{1}{2}$s is given by

$$H = J\mathbf{s}_1 \cdot \mathbf{s}_2 \tag{1.1}$$

where J is the coupling coefficient for two spin-$\frac{1}{2}$ particles and $\mathbf{s}_i \equiv \frac{1}{2}\left(\sigma_i^x \hat{\mathbf{x}} + \sigma_i^y \hat{\mathbf{y}} + \sigma_i^z \hat{\mathbf{z}}\right)$ is the spin-$\frac{1}{2}$ operator where σ_i^α is the Pauli spin operator on site i in the α^{th} direction.

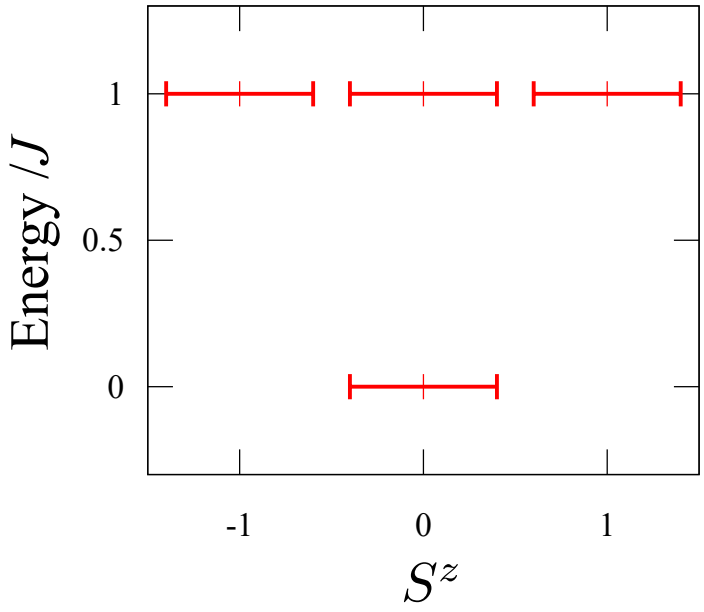

Figure 1.4: Spectrum of two coupled spin-$\frac{1}{2}$ particles with a constant energy shift of $\frac{3}{4}$.

As shown in Fig. 1.4, the spectrum consists of a ground state singlet followed by excited triplet states.

Now consider a chain of spin-1 particles described by the Heisenberg Hamiltonian given by

$$H = J\sum_{i=1}^{L-1} \mathbf{S}_i \cdot \mathbf{S}_{i+1} \tag{1.2}$$

where now, $\mathbf{S}_i$ is the spin-1 operator. For the case of a chain of 14 spins, the low energy spectrum also consists of a ground state singlet followed by a first excited state triplet as shown in Fig. 1.5.

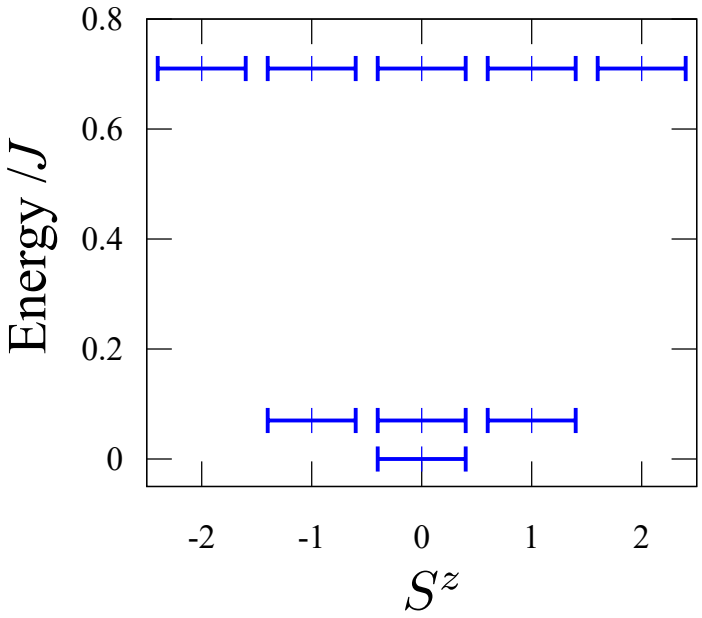

Figure 1.5: Spectrum of the Heisenberg Hamiltonian for 14 sites.

Additionally, the low energy spectrum of the spin-1 chain contains quintuplet states which are higher in energy than the triplet states.

As long as there are an even number of sites, the low energy spectrum will always consist of a ground state singlet followed by first excited state triplets and second excited state quintuplets as shown in Fig. 1.6.

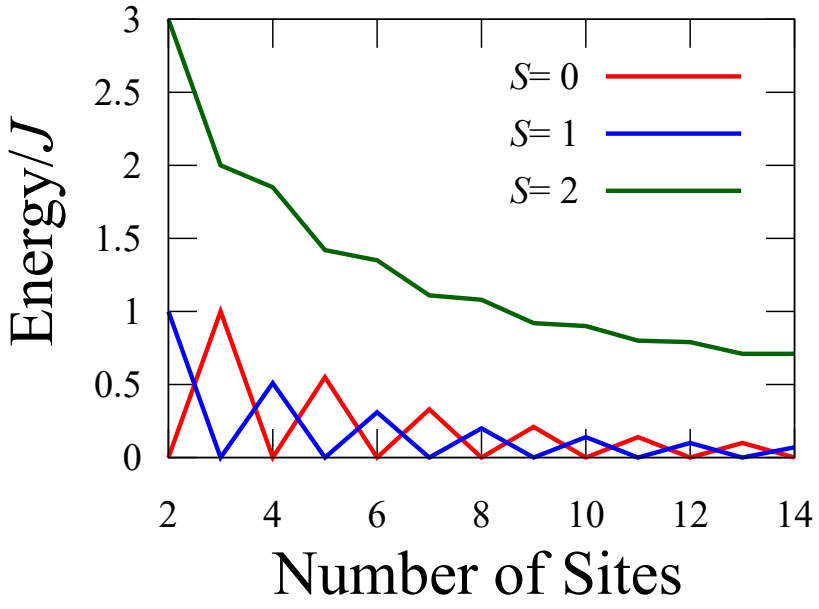

Figure 1.6: Low energy spectrum of the Heisenberg spin-1 chain as a function of chain length.

For systems with an odd number of sites, the triplet is the ground state and the first excited state is the singlet while the quintuplet remains the second excited state. As the chain length increases, the singlet and triplet approach degeneracy while the gap between the quintuplet and singlet states approaches a finite value of $0.41J$. In the thermodynamic limit where the singlet and triplet are exactly degenerate and the spectral gap is $0.41J$, the system is in a topological phase known as the Haldane phase [17, 18].

The Haldane phase, which is defined by the singlet-triplet degenerate ground state and the spectral gap separating the singlet from the quintuplet states, can be understood in terms of two spin-$\frac{1}{2}$ quasiparticles at the edges of the spin-1 chain [17, 18].

Although the ground state of a Heisenberg spin-1 chain in the limit of an infinitely long chain with open boundary conditions exhibits the Haldane phase, a similar system described by a Hamiltonian with the additional biquadratic term $(\mathbf{S}_i \cdot \mathbf{S}_{i+1})^2$ also exhibits the Haldane phase, but with any number of sites, thus a long chain is not necessary, deeming this system a useful tool in understanding the Heisenberg spin-1 chain. The Hamiltonian for said system, known as the AKLT Hamiltonian, which

was proposed by Affleck, Kennedy, Lieb and Tasaki [18], is given by

$$H = J \sum_i \left(\mathbf{S}_i \cdot \mathbf{S}_{i+1} + \frac{1}{3} (\mathbf{S}_i \cdot \mathbf{S}_{i+1})^2 + \frac{2}{3} \right) \tag{1.3}$$

Similar to the Heisenberg chain, the ground state of the AKLT Hamiltonian also consists of four-fold degenerate singlet and triplet states except here, the singlet and triplet states are not only exactly degenerate, but are exactly degenerate for any number of spin-1 sites.

Affleck, Kennedy, Lieb and Tasaki showed that the ground state of the AKLT Hamiltonian, and therefore the ground state of the Heisenberg spin-1 chain, can be understood in terms of two spin-$\frac{1}{2}$ quasiparticles at the edges of the chain by projecting each individual spin-1 onto a spin-$\frac{1}{2}$ subspace [18]. In this representation of the ground state, the spin-$\frac{1}{2}$s between neighbouring sites are singlet bonded as shown schematically in Fig.1.7, leaving two unbonded spin-$\frac{1}{2}$ quasiparticles dangling at each edge of the chain.

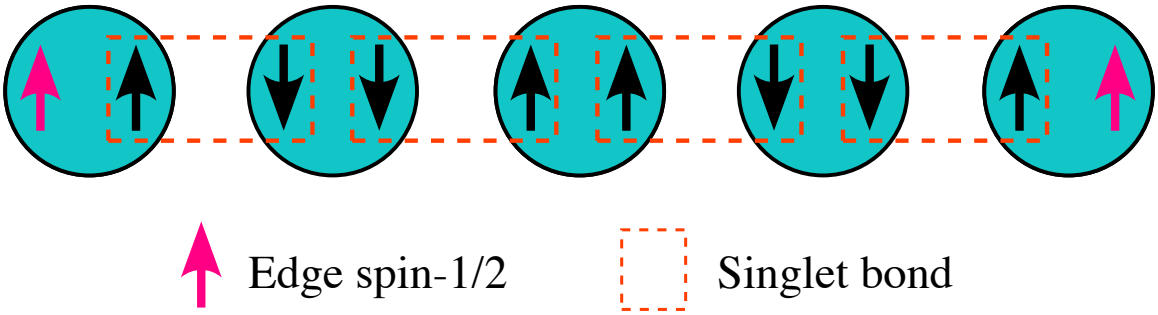

Figure 1.7: Schematic of an antiferromagnetic spin-1 chain where each spin-1 is projected onto two spin-$\frac{1}{2}$s. The up arrow represents a spin-up particle and the down arrow represents a spin-down particle. The singlet bonds between sites are illustrated by a dashed red line. The spin-$\frac{1}{2}$ edge particles are coloured in fuchsia.

The spin-1 chain is a viable candidate for a topologically protected qubit since the ground state is protected by a finite energy gap from higher energy states [15,16]. In this system, the qubit basis would be the $S^z = 0$ singlet and $S^z = 0$ triplet states. Unlike many superconducting [19–21], photonic [22–24] and trapped ion [25,26] qubits currently in production, such a qubit has the potential to operate at room temperature if the spectral gap is of that order of magnitude, which is roughly 25 meV.

In this work, we focus on the design of a single photon emitter and a synthetic spin-1 chain using an array of InAsP quantum dots embedded in a nanowire. In this synthetic spin-1 chain, each synthetic spin-1 is formed by injecting electrons so that the p-shell in each quantum dot is half-filled. Though the spectral gap for a long chain was computed to be far from room temperature at about 1 meV, this work outlines the steps necessary in order to realize the Haldane phase in a semiconductor quantum dot array.

1.3 Thesis Contributions.

Chapters 1 and 2 of this thesis are reviews of well established theory of computational tools developed and used in this work. The remaining chapters are based on the publications and manuscripts listed below.

1. Laferrière, P., Yeung, E., Korkusinski, M., Poole, P. J., Williams, R. L., Dalacu, D., Manalo, J., Cygorek, M., Altintas, A., Hawrylak, P. (2021). *Systematic study of the emission spectra of nanowire quantum dots.* Applied Physics Letters, **118**(16), 161107.

2. Manalo, J., Cygorek, M., Altintas, A., Hawrylak, P. (2021). *Electronic and magnetic properties of many-electron complexes in charged InAsP quantum dots in InP nanowires.* Phys. Rev. B, **104**(12), 125402.

3. Manalo, J., Miravet, D., Hawrylak, P. (2022). *Microscopic design of a topologically protected singlet-triplet qubit in an InAsP quantum dot array.* arXiv. (Also submitted to Phys. Rev. B).

In all three papers, I was the lead graduate student theorist and performed all of the simulations and numerical calculations. Furthermore, in the two papers where I am lead author, I also generated all of the figures. For the first paper listed, the experiments and the text and figures pertaining to the experiments were done by the research group at the National Research Council.

1.4 Thesis Outline.

The rest of the thesis is organized as follows.

- Chapter 2 presents the different methodologies used in the simulation of the quantum dot nanowires studied in this thesis. The first part of this chapter discusses the techniques used in the in-house computational tool QNANO for simulating nanostructures containing upwards of millions of atoms. These techniques include using a parameterized tight-binding model and configuration interaction. The following section of this chapter discusses a technique for simulating many-body systems that uses a form of the wavefunction known as a matrix product state to perform the density matrix renormalization group algorithm.

- Chapter 3 presents a joint experimental and theory paper on the study of the emission spectra of an InAsP quantum dot in a nanowire. Using both experimental techniques and theory, the peaks in the emission spectrum are characterized. Furthermore, the design of the quantum dot with different concentrations of As for the purpose of engineering single and entangled photon emitters is explored. This paper was published in Applied Physics Letters.

- Chapter 4 presents a paper on the electronic and magnetic properties of a single InAsP quantum dot and two InAsP quantum dots in an InP nanowire. Using the tight-binding and configuration interaction methods to simulate the quantum dot, we show that when the p-shells of the quantum dots are half-filled, a single quantum dot behaves like a spin-1 object and that two quantum dots behave like two coupled spin-1 objects, opening up the possibility of using these quantum dot nanowires as a synthetic spin-1 chain and hence the possibility of constructing a topologically protected qubit. We then derive parameters for an effective multi-orbital Hubbard model in order to compute longer quantum dot arrays for future calculations. This paper was published in Physical Review B.

- Chapter 5 presents a paper on the steps enabling the design of a topologically protected singlet-triplet qubit using an array of InAsP quantum dots in a nanowire. Using the parameters obtained from microscopic calculations, the spectrum of a long chain of quantum dots was computed using the multi-orbital Hubbard model. The behaviour of the system under an applied magnetic field was studied to determine similarities in behaviour to two spin-$\frac{1}{2}$ particles at the edges of the chain, which is an indication of a topologically protected state. Finally, regions in the multi-orbital Hubbard parameter space in which the topologically protected phase exists were mapped. This paper has been submitted to arXiv and has been submitted to Physical Review B.

- Chapter 6 discusses the conclusions and future work.

Chapter 2

Methodology

There are several computational techniques that are employed in the simulation of the quantum dot nanowires in this work. First, a single InAsP quantum dot in an InP nanowire was modelled microscopically using a tight-binding model, with up to a million atoms, where the parameters were obtained from density functional theory (DFT) band structures [4]. Using the basis of single-particle states from the tight-binding model, the many-body spectrum of both excitonic complexes and N electron complexes was computed with a technique known as configuration interaction. Essentially, the Hamiltonian was diagonalized in the basis of excitonic configurations using numerical diagonalization. The techniques used for the microscopic calculations were also applied to a system of two InAsP quantum dots in an InP nanowire.

To compute the spectra of InAsP quantum dot arrays containing many quantum dots, an effective multi-orbital Hubbard model was used instead of the microscopic model. For large enough quantum dot arrays, the number of configurations is so large that computing the spectra is insurmountable with exact diagonalization. Instead, for such systems, a technique known as Density Matrix Renormalization Group (DMRG) was used. The DMRG technique is a variational method of obtaining the ground state of a many-body system. At the heart of this technique is the expression of each wavefunction coefficient as a product of tensors, where each tensor corresponds to the occupation of an orbital. For a system with 10 orbitals, instead of using $O(2^{10})$ coefficients to describe the ground state, only $O(m^2 10)$ numbers are needed, where the

dimension of each tensor is m. In order to gain an advantage in saving computational resources, the dimension of each tensor m must be sufficiently small, but also large enough that the wavefunction is still an excellent approximation. The wavefunction in the form where each coefficient is a product of tensors is known as a Matrix Product State (MPS).

2.1 QNANO: Microscopic computational platform for the electronic and optical properties of million atom semiconductor nanostructures

The microscopic calculations for the nanostructures in this work are done using the QNANO computational tool which can simulate nanostructures containing up to millions of atoms [27, 28]. First, the nanostructure is defined by the positions of each atom. Examples of such nanostructures are CdSe nanocrystals, InAs/GaAs lens shaped quantum dots and the nanostructure that is the focus of this work, InAsP quantum dots in a InP nanowire [3, 5, 28, 29]. The total elastic energy of the system is then minimized to obtain new equilibrium positions. Using a basis of localized atomic s, p, d and $s*$ orbitals, a tight-binding Hamiltonian is constructed with tunelling parameters obtained from ab-initio calculations. The single particle states from this tight-binding Hamiltonian are then used to compute the manybody spectrum of N electrons or excitonic complexes using configuration interaction (CI). Using Fermi's Golden Rule, emission spectra can be computed using the spectra of excitonic complexes.

2.1.1 Tight-binding Model

The generation of single-particle states which are then used to compute the many-body spectrum begins with creating an atomistic structure defined by atomic positions in an ideal wurtzite lattice. First, a nanowire of InP atoms is constructed, and within

this volume, a quantum dot volume is defined in which random P atoms are replaced with As atoms at a given concentration. To avoid surface states from going into the region of energies close to the band gap, the surface is passivated by increasing the dangling sp^3 bonds to energies much higher than the band gap. Since we are dealing with a nanostructure composed of two different materials with different lattice constants, strain will cause the atoms to relax to new equilibrium positions which are obtained minimizing the total elastic energy according to the Keating valence force field model given by [30]

$$U = \frac{1}{2}\sum_{i=1}^{N_a}\{\sum_{j=1}^{nn(i)} \frac{3\alpha_{i,j}}{4(d_{i,j}^0)^2}\left[(\mathbf{R}_j - \mathbf{R}_i)^2 - (d_{i,j}^0)^2\right]^2 + \sum_{j=1}^{nn(i)}\sum_{k<j}^{nn(i)} \frac{3\beta_{i,j,k}}{4d_{i,j}^0 d_{j,k}^0}\left[(\mathbf{R}_j - \mathbf{R}_i)\cdot(\mathbf{R}_k - \mathbf{R}_i) - d_{i,j}^0 d_{i,k}^0 \cos\theta_{i,j,k}\right]^2\}, \quad (2.1)$$

where N_a is the number of atoms, $nn(i)$ denotes the nearest neighbours of atom i, $\mathbf{R}_i$ is the position of atom i, $d_{i,j}^0$ is the unstrained lattice constant, $\theta_{i,j,k}$ is the bond angle between bonds i,j and j,k and the coefficients $\alpha_{i,j}$ and $\beta_{i,j,k}$ are material parameters known as the Keating parameters.

The structure generation and the computation of the relaxed atomic positions are prerequisite to solving the tight-binding Hamiltonian, which is given by

$$H_{TB} = \sum_{i=1}^{N_a}\sum_{\alpha=1}^{N_{\text{orb}}} \varepsilon_{i,\alpha} c_{i,\alpha}^\dagger c_{i,\alpha} + \sum_{i=1}^{N_a}\sum_{\alpha,\beta=1}^{N_{\text{orb}}} \lambda_{i,\alpha,\beta} c_{i,\alpha}^\dagger c_{i,\beta} + \sum_{i=1}^{N_a}\sum_{j=1}^{nn(i)}\sum_{\alpha,\beta=1}^{N_{\text{orb}}} t_{i,\alpha,j,\beta} c_{i,\alpha}^\dagger c_{j,\beta}, \quad (2.2)$$

where N_{orb} is the number of orbitals per atom, α and β denote atomic orbital, $\varepsilon_{i,\alpha}$ is the onsite energy at orbital α on atom i, $t_{i,\alpha,j,\beta}$ is the tunelling matrix element between orbital α on atom i and orbital β on atom j, $\lambda_{i,\alpha,\beta}$ describes the spin-orbit interaction and $c_{i,\alpha}^\dagger$ ($c_{i,\alpha}$) are the creation (annihilation) operators for an electron on atom i and orbital α. Here, spin indices are implicit (i.e. $c_{i,\alpha}^\dagger = c_{i,\alpha,\uparrow}^\dagger + c_{i,\alpha,\downarrow}^\dagger$).

The tight-binding parameters in Eq. 2.2 for the unstrained structure are obtained by fitting the Hamiltonian to band structures obtained from ab-initio calculations for InP and InAs. With the fitting procedure, detailed in Ref. [4], two sets of tight-

binding parameters, one for InP and one for InAs are obtained. The parameters used in this work, which are listed in Ref. [4] are also listed below.

Table 2.1: Tight-binding parameters for InP and InAs in the wurtzite phase.

Tight-binding parameter	InP	InAs
E_s^a	-3.9798	-5.3673
E_s^c	-1.9268	-0.9905
E_p^a	2.3067	2.3917
E_p^c	6.8862	6.6883
E_{pz}^a	2.3389	2.6082
E_{pz}^c	6.2922	6.0555
E_d^a	13.4134	13.7658
E_d^c	12.2801	12.5896
$E_{s^*}^a$	19.2302	19.5859
$E_{s^*}^c$	19.1728	18.3726
Δ_{so}^a	0.0217	0.1482
Δ_{so}^c	0.1675	0.0645
$V_{ss\sigma}$	-2.6537	-3.5352
$V_{sp\sigma}^{ac}$	3.3428	4.3074
$V_{sp\sigma}^{ca}$	3.3557	3.5224
$V_{pp\sigma}$	3.8437	3.5053
$V_{pp\pi}$	-1.2305	-1.2792
$V_{ss^*\sigma}^{ac}$	-1.3517	-2.5597
$V_{ss^*\sigma}^{ca}$	-3.8673	-5.5423
$V_{s^*s^*\sigma}$	-4.3416	-5.7421
$V_{s^*p\sigma}^{ac}$	2.6263	2.2262
$V_{s^*p\sigma}^{ca}$	3.1080	3.5650
$V_{sd\sigma}^{ac}$	-3.2625	-4.7604
$V_{sd\sigma}^{ca}$	-2.4241	-2.9015
$V_{pd\sigma}^{ac}$	-1.8250	-1.6637
$V_{pd\sigma}^{ca}$	-1.3002	-1.2407
$V_{pd\pi}^{ac}$	1.4239	1.3719
$V_{pd\pi}^{ca}$	1.6504	2.2598
$V_{s^*d\sigma}^{ac}$	-0.7779	-1.2618
$V_{s^*d\sigma}^{ca}$	-0.6759	-1.1917
$V_{dd\sigma}$	-1.8423	-2.3460
$V_{dd\pi}$	3.2696	2.4663
$V_{dd\delta}$	-0.5511	-0.9812

Here, E refers to the onsite energy, Δ refers to the spin-orbit splitting and V refers to hopping elements. The superscripts a and c denote anion and cation, which in the case of InAs or InP are In and As or P respectively. The subscripts denote the orbital, except for the spin-orbit parameters, where the subscript *so* refers to "spin-orbit". For example, E_s^c is the onsite energy of an electron on the s shell of In. Another

example would be $V^{ca}_{pd\pi}$, which refers to the hopping energy of an electron going from the p-shell of In to the d-shell of P where π indicates a π bond formed between the p and d shells.

To incorporate strain, the tight-binding parameters must be adjusted with the relaxed atomic positions. The hopping elements $t_{i,\alpha,j,\beta}$ are rescaled by a factor $\left(\frac{d_{i,j}}{d^0_{i,j}}\right)^{\eta_{\alpha,\beta}}$ as per Harrison's law, where $d_{i,j}$ and $d^0_{i,j}$ are the strained and ideal bond lengths respectively and the power $\eta_{\alpha,\beta}$ is a material dependent parameter [31]. Furthermore, the onsite energies $\varepsilon_{i,\alpha}$ are adjusted using the following formula

$$\varepsilon_{i,\alpha} = \varepsilon^0_{i,\alpha} + \sum_{j=1}^{nn(i)} C_{i,\alpha,j,\beta} \frac{(t_{i,\alpha,j,\beta})^2 - (t^0_{i,\alpha,j,\beta})^2}{(\varepsilon^0_{i,\alpha} - \varepsilon_{\text{ref}}) + (\varepsilon^0_{j,\beta} - \varepsilon_{\text{ref}})} \tag{2.3}$$

where $\varepsilon^0_{i,\alpha}$ is the unstrained onsite energy, ε_{ref} is a reference energy set to be 27 meV, $t^0_{i,\alpha,j,\beta}$ is the unstrained hopping element and $C_{i,\alpha,j,\beta}$ is a material dependent parameter [32].

With the tight-binding parameters adjusted for strain, the tight-binding Hamiltonian in Eq. 2.2 can be diagonalized to obtain single particle states which are of the form

$$\langle \mathbf{r}|i\rangle = \sum_k \sum_\alpha C_{i,k,\alpha}\phi_\alpha(\mathbf{r} - \mathbf{R}_k) \tag{2.4}$$

where $\phi_\alpha(\mathbf{r} - \mathbf{R}_k)$ is the local atomic orbital wavefunction for orbital α of atom k at location $\mathbf{R}_k$. The local atomic orbitals are assumed to be Slater orbitals given by

$$\phi_\alpha(\mathbf{r}) = Ar^a e^{-br} Y^m_l(\theta,\phi)\chi_\sigma \tag{2.5}$$

The single particle states are obtained using exact diagonalization. With the single particle states computed, the many-body spectrum of any electronic or excitonic complex can be obtained and thus, emission spectra can also be computed.

2.1.2 Configuration Interaction

The many-body spectra of electronic and excitonic complexes are computed using the configuration interaction method. Essentially, the spectrum is obtained by diagonalizing a many-body Hamiltonian with Coulomb interactions in the basis comprised of all possible configurations with N_e electrons and N_h holes across a truncated set of single particle states. The many-body Hamiltonian is given by

$$\begin{aligned} H = &\sum_i E_i^{(e)} c_i^\dagger c_i + \sum_p E_p^{(h)} h_p^\dagger h_p + \frac{1}{2}\sum_{i,j,k,l} \langle i,j|V_{ee}|k,l\rangle c_i^\dagger c_j^\dagger c_k c_l \\ &+ \frac{1}{2}\sum_{p,q,r,s} \langle p,q|V_{hh}|r,s\rangle h_p^\dagger h_q^\dagger h_r h_s \\ &- \sum_{i,q,r,l} \left(\langle i,q|V_{eh}^d|r,l\rangle - \langle i,q|V_{eh}^x|l,r\rangle\right) c_i^\dagger h_q^\dagger h_r c_l \end{aligned} \tag{2.6}$$

where h_p is the hole operator (defined as $h_p \equiv c_p^\dagger$), $E_i^{(e)}$ is the energy of the i^{th} electronic single particle state and $E_p^{(h)}$ is the energy of the p^{th} hole state. Electronic energies are taken from the conduction band and hole energies are the negative of the valence band energies. Furthermore, the many-body Hamiltonian contains the Coulomb interaction terms, which are the electron-electron (V_{ee}), hole-hole (V_{hh}) and direct (V_{eh}^d) and exchange (V_{eh}^x) electron-hole interactions. When computing eigenstates of electronic complexes, the terms involving the hole operators are ignored.

The general formula for the Coulomb matrix element in the basis of linear combinations of atomic orbitals is given by [27]

$$\begin{aligned} \langle i,j|V|k,l\rangle = &\sum_{a_1,\alpha}\sum_{a_2,\beta}\sum_{a_3,\gamma}\sum_{a_4,\delta} C_{i,a_1,\alpha}^* C_{j,a_2,\beta}^* C_{k,a_3,\gamma} C_{l,a_4,\delta} \\ &\frac{e^2}{4\pi}\int d^3r_1 d^3r_2 \frac{\phi_\alpha^*(\mathbf{r}_1-\mathbf{R}_{a_1})\phi_\beta^*(\mathbf{r}_2-\mathbf{R}_{a_2})\phi_\gamma(\mathbf{r}_2-\mathbf{R}_{a_3})\phi_\delta(\mathbf{r}_1-\mathbf{R}_{a_4})}{\epsilon(\mathbf{R}_{a_1},\mathbf{R}_{a_2})|\mathbf{r}_1-\mathbf{r}_2|} \end{aligned} \tag{2.7}$$

where e is the elementary charge and $\epsilon(\mathbf{R}_{a_1},\mathbf{R}_{a_2})$ is the distance dependent dielectric constant. Since the complexity of the Coulomb matrix element in Eq. 2.8 is N_a^4 and the nanowire structures are of the order of 10^6 atoms, approximations must be made in order for the computation to be feasible.

First, only two-centre integrals are considered, which are integrals that involve at most scattering between two atoms. Second, each Coulomb matrix element consists of only long-range and on-site terms

$$\langle i,j|V|k,l\rangle = \langle i,j|V^{\mathrm{OS}}|k,l\rangle + \langle i,j|V^{\mathrm{LR}}|k,l\rangle. \tag{2.8}$$

Here, we introduce the following approximation of the distance dependent dielectric constant given by

$$\epsilon(\mathbf{r}_1,\mathbf{r}_2) = \begin{cases} \epsilon_0 & \text{if} \quad |\mathbf{r}_1-\mathbf{r}_2| = 0 \\ \epsilon_0\epsilon_{LR} & \text{otherwise} \end{cases}. \tag{2.9}$$

In this approximation, scattering involving orbitals of one atom is unscreened while the scattering involving orbitals of two atoms is screened by the bulk dielectic constant ϵ_{LR}.

The on-site term only consists of integrals where scattering occurs between orbitals within a single atom.

$$\begin{aligned}\langle i,j|V^{\mathrm{OS}}|k,l\rangle = \frac{e^2}{4\pi\epsilon_0}\sum_{a\in N_{\mathrm{a}}}\sum_{\alpha,\beta,\gamma,\delta} C^*_{i,a,\alpha}C^*_{j,a,\beta}C_{ka\gamma}C_{l,a,\delta} \\ \times\int \frac{\phi^*_\alpha(\mathbf{r}_1)\phi^*_\beta(\mathbf{r}_2)\phi_\gamma(\mathbf{r}_2)\phi_\delta(\mathbf{r}_1)}{|\mathbf{r}_1-\mathbf{r}_2|}d^3r_1d^3r_2\end{aligned} \tag{2.10}$$

The long-range term consists of integrals where scattering occurs between nearest neighbour atoms. In the long-range approximation, the charge densities are assumed to be point charges which leads to an orthogonalization condition that results in an expression that is equivalent to a weighted sum of the classical Coulomb interactions between two point charges.

To see this more clearly, we begin with the expression for the long-range Coulomb

term.

$$\begin{aligned}\langle i,j|V^{\mathrm{LR}}|k,l\rangle =& \frac{e^2}{4\pi\epsilon_0\epsilon_{\mathrm{LR}}}\sum_{b\neq a}\sum_{\alpha\beta} C^*_{i,a,\alpha}C_{l,a,\alpha}C^*_{j,b,\beta}C_{k,b,\beta} \\ &\times \int \frac{\phi^*_\alpha(\mathbf{r}_1-\mathbf{R}_a)\phi_\alpha(\mathbf{r}_1-\mathbf{R}_a)\phi^*_\beta(\mathbf{r}_2-\mathbf{R}_b)\phi_\beta(\mathbf{r}_2-\mathbf{R}_b)}{|\mathbf{r}_1-\mathbf{r}_2|}d^3r_1d^3r_2\end{aligned} \tag{2.11}$$

The orthogonalization condition arising from the point charge distributions is shown below

$$\begin{aligned}I &\equiv \int \frac{\left[\phi^*_\alpha(\mathbf{r}_1-\mathbf{R}_a)\phi_\alpha(\mathbf{r}_1-\mathbf{R}_a)\right]\left[\phi^*_\beta(\mathbf{r}_2-\mathbf{R}_b)\phi_\beta(\mathbf{r}_2-\mathbf{R}_b)\right]}{|\mathbf{r}_1-\mathbf{r}_2|}d^3r_1d^3r_2 \\ &= \int \frac{\delta^3(\mathbf{r}_1-\mathbf{R}_a)\delta^3(\mathbf{r}_2-\mathbf{R}_b)}{|\mathbf{r}_1-\mathbf{r}_2|}d^3r_1d^3r_2 \\ &= \frac{1}{|\mathbf{R}_a-\mathbf{R}_b|}\end{aligned} \tag{2.12}$$

Substituting Eq. 2.12 into Eq. 2.11 gives the expression for the long-range term as a sum of weighted classical Coulomb interactions between point charges.

$$\langle i,j|V^{\mathrm{LR}}|k,l\rangle = \sum_{b\neq a}\sum_{\alpha\beta}\frac{e^2}{4\pi\epsilon_0\epsilon_{\mathrm{LR}}|\mathbf{R}_a-\mathbf{R}_b|}C^*_{i,a,\alpha}C_{l,a,\alpha}C^*_{j,b,\beta}C_{k,b,\beta} \tag{2.13}$$

With the Coulomb matrix elements and single particle states computed, the spectra of any excitonic complex can be computed. For example, to compute the excitonic spectrum, a basis of all possible excitonic configurations $|i,p\rangle = c_i^\dagger h_p^\dagger|0\rangle$ is constructed out of a truncated set of valence band states p and conduction band sates i, where $|0\rangle$ is the semiconductor ground state, which is the configuration with a full valence band and an empty conduction band. From diagonalization of the many-body Hamiltonian in the exciton basis, the excitonic states are obtained, which have the form

$$|X_\alpha\rangle = \sum_{i,p} A^\alpha_{i,p}|i,p\rangle. \tag{2.14}$$

Experimentally, the spectra of excitonic complexes are probed by measuring the

emission spectra [3, 11, 33]. The emission spectrum can be computed using Fermi's Golden Rule.

One of the ingredients of implementing Fermi's Golden Rule is the dipole matrix element given by

$$D_{i,p}(\boldsymbol{\epsilon}) = \langle i|\mathbf{r}\cdot\boldsymbol{\epsilon}|p\rangle, \tag{2.15}$$

where $|i\rangle$ and $|p\rangle$ are single particle electron and hole states respectively and $\boldsymbol{\epsilon}$ is the polarization vector of the external electric field.

Eq. 2.15 is used to define the polarization operator

$$P(\boldsymbol{\epsilon}) = \sum_{i,p} D_{i,p} c_i h_p \tag{2.16}$$

which removes an electron-hole pair from the system.

The polarization operator is then used in Fermi's Golden Rule to obtain the emission spectrum as a function of energy E.

$$F(E,\boldsymbol{\epsilon}) = \sum_{i,f} |\langle i|P(\boldsymbol{\epsilon})|f\rangle|^2 \delta(E-(E_f-E_i)) n_i(1-n_f) \tag{2.17}$$

Here, i and f denote the initial and final many-body states and n_i (n_f) denote the occupation of the initial (final) state.

Since we are interested in the total emission spectrum, all polarizations are included. The total emission spectrum is obtained by summing over the polarizations along the three spatial coordinates.

$$F(E) = F(E,\hat{\mathbf{i}}) + F(E,\hat{\mathbf{j}}) + F(E,\hat{\mathbf{k}}) \tag{2.18}$$

In essence, the implementation of configuration interaction that is used in the computations in this thesis begins with a chosen set of single particle states. With these single particle states, the Coulomb matrix elements are computed using sev-

eral approximations. First, only two-centre integrals are computed and second, each Coulomb matrix element is decomposed into two terms; one on-site term and one long-range term. The former only includes integrals where electrons are scattered within an atom and the latter involves an approximation where the charge distributions are point charges, which turns the integral over $d^3r_1d^3r_2$ into an orthonormalization relation. Once the Coulomb matrix elements are computed, the many-body spectrum of a given excitonic complex is computed by diagonalizing the many-body Hamiltonian in the basis of configurations. For optical spectra, Fermi's Golden Rule is implemented where the initial and final states are many-body states.

The method of obtaining the manybody spectrum using CI, where the single particle states are from a parameteried TB Hamiltonian, is an accurate way to compute electronic properties of nanostructures, but since these simulations tend to involve millions of atoms, other methods must be employed if one wants to compute much larger structures. For one, if the system contains an ensemble of smaller systems where the spectra has already been computed, an effective model can be constructed where the parameters are obtained from the microscopic calculations. Such an approach was taken in Chapter 4, where parameters for an effective model describing a chain of InAsP quantum dots were obtained from microscopic calculations of a single quantum dot. In some cases, it is possible to still use the configuration interaction method to obtain the spectrum of the effective model, however these calculations are still limited to small systems. To obtain the spectrum of large systems that would otherwise be computationally infeasible with configuration interaction, a method known as Density Matrix Renormatlization Group may provide exponential savings in computational resources. The Density Matrix Renormalization Group Algorithm is a variational method of obtaining the ground state of a large many-body system. The approximation process that turns the complexity of the wavefunction from exponential in L to linear in L involves keeping only significant configurations while discarding the rest.

2.2 The Density Matrix Renormalization Group Using a Tensor Network

The Hilbert Space of a many-body system grows exponentially with the number of allowed single-particle states. If the system is large enough, it would be impossible even for the largest supercomputing clusters to compute the ground state if exact diagonalization is used. For example, to store the ground state of a Heisenberg chain of 50 spin-1 particles where the number of configurations is $O(3^{50}) \approx 7 \times 10^{23}$, it would require ≈ 1.2 million Exabytes, which is roughly the size of the entire internet. In practice, the ground state of a many-body system usually only contains relatively few significant configurations. The density matrix renormalization group (DMRG) algorithm [34–36] is a method to obtain an approximate ground state using only a small corner of the Hilbert Space, which allows one to compute the ground state of spin-1 chains much greater than 50 spins for example. Though this method is not efficient for every many-body system, it is useful for low entanglement systems such as 1-dimensional chains with short-range interactions.

2.2.1 Entropy Area Law

A many-body system can be divided into two subsystems A and B where $A \subseteq B$. The entropy area law states that the entanglement entropy S grows at most linearly with respect to the size of the boundary between A and B [37].

$$S \propto \partial A \tag{2.19}$$

In general, many-body systems do not satisfy the entropy area law, but the systems that do are ones with short range interactions [38–40]. This can be intuitively understood by the fact that with such systems, only degrees of freedom that are cut by the boundary ∂S are entangled.

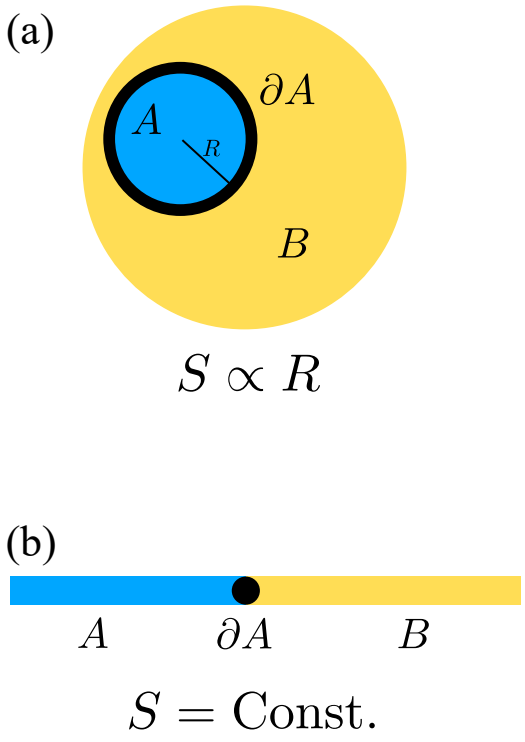

Figure 2.1: Two diagrams of systems with shortrange interactions that are divided into two subsystems A and B with the boundary ∂A labelled. (a) is a two dimensional system with disc geometry and (b) is a one dimensional system.

Fig. 2.1 shows examples of systems that are divided into subsystems A and B where shortrange interactions are assumed. In Fig. 2.1 (a), the entanglement entropy grows proportionally to the size of the radius of disc A. In Fig. 2.1 (b), the boundary between A and B is a point, thus the entanglement entropy is constant with respect to the size of A, making such systems ideal candidates for attaining solutions efficiently using DMRG. Moreover, it has been proven in Ref. [38] that one dimensional gapped systems obey an entropy area law.

Consider such a one dimensional system that obeys the entropy area law, i.e. a system where the entanglement entropy is constant with respect to the size of the partition A. The many-body wavefunction can be expressed in Schmidt form given by

$$|\Psi\rangle = \sum_i \lambda_i |A\rangle_i |B\rangle_i \tag{2.20}$$

where $|A\rangle$ and $|B\rangle$ are configurations in A and B respectively. This form of the wavefunction can be obtained using Singular Value Decomposition. It is expected

that for this system, a majority of the wavefunction coefficients λ_i are negligible, which allows for the computation of the approximate ground state to be feasible. In practice, a threshold for λ_i can be set and an approximate wavefunction can be formed where the configurations in which λ_i is below this threshold are neglected. This implies that such a system is of low entanglement entropy where the entanglement entropy is defined as

$$S = -\sum_i \lambda_i^2 \log \lambda_i^2 \tag{2.21}$$

In the following section, I will introduce the formalism in which the DMRG algorithm is carried out. Essentially, to obtain the ground state, a trial wavefunction is constructed as a matrix product state (MPS) where each wavefunction coefficient is a product of orbital dependent tensors. The operator is constructed as a matrix product operator (MPO) where each matrix element is a product of orbital dependent tensors analogous to the matrix product state. Finally, an expectation value is constructed by combining the MPS and MPO to form what is known as a tensor network, which is a more general object containing many tensors. This tensor network construction of the expectation value of the Hamiltonian is then minimized with respect to each individual tensor element using a variational method to obtain the ground state.

2.2.2 Matrix Product States

Consider a many-body Hamiltonian given by

$$H = \sum_{i,j} \varepsilon_{i,j} c_i^\dagger c_j + \frac{1}{2} \sum_{i,j,k,l} \langle i,j|V|k,l\rangle c_i^\dagger c_j^\dagger c_k c_l \tag{2.22}$$

where i, j, k and l refer to single particle states.

The ground state of the Hamiltonian in Eq. 2.22 is given by the following general many-body electron wavefunction

$$|\Psi\rangle = \sum_{n_1,n_2,\ldots,n_L=0,0,\ldots 0}^{1,1,\ldots 1} \psi_{n_1,n_2,\ldots,n_L} |n_1, n_2, \ldots, n_L\rangle \tag{2.23}$$

where each $n_i \in \{0, 1\}$ is an electron occupation quantum number for single particle state i and L is the total number of single particle states. For now, we will consider the general case where the number of electrons are not conserved. For many large systems of interest, it is computationally infeasible to obtain this ground state since there are 2^L configurations. Through the use of singular value decomposition which we will show in the next section, we can express Eq. 2.23 as a matrix product state (MPS) given by

$$|\Psi\rangle = \sum_{n_1,n_2,\ldots,n_L=0,0,\ldots 0}^{1,1,\ldots 1} M^{[1]n_1} M^{[2]n_2} \cdots M^{[L]n_L} |n_1, n_2, \ldots, n_L\rangle \tag{2.24}$$

where each $M^{[k]n_k}$ is a matrix and the maximum dimension of all of the $M^{[k]n_k}$ matrices is χ_{MAX}. In practice, we will drop the superscript $[k]$ since it is implied by the order in which M^{n_k} appears in the product $M^{[1]n_1} M^{[2]n_2} \cdots M^{[L]n_L}$ as shown by

$$|\Psi\rangle = \sum_{n_1,n_2,\ldots,n_L=0,0,\ldots 0}^{1,1,\ldots 1} M^{n_1} M^{n_2} \cdots M^{n_L} |n_1, n_2, \ldots, n_L\rangle.$$

We can make an approximation to Eq. 2.24 by setting a maximum dimension $m \ll \chi_{\text{MAX}}$. With this approximation, the number of configurations $O(2m^2L)$ is linear in L which greatly reduces the Hilbert space.

2.2.3 Singular Value Decomposition

Before we get into the details on how MPS and DMRG lead to an approximation of the ground state that utilizes only a small portion of the total Hilbert space of the system, it is imperative to show that an arbitrary many-body wavefunction as shown in Eq. 2.23 can be expressed as an MPS as shown in Eq. 2.24 without any approximations. The process of obtaining an MPS from a wavefunction involves expressing the coefficients of the wavefunction as a $2 \times 2^{L-1}$ tensor and iteratively applying singular value decomposition until you have a product of L tensors.

The $2 \times 2^{L-1}$ tensor that describes the coefficients of the wavefunction in Eq. 2.23 is given by

$$\hat{\Psi} = \begin{pmatrix} \psi_{0,(0\ldots0)} & \psi_{0,(0\ldots1)} & \cdots & \psi_{0,(1\ldots1)} \\ \psi_{1,(0\ldots0)} & \psi_{1,(0\ldots1)} & \cdots & \psi_{1,(1\ldots1)} \end{pmatrix} \tag{2.25}$$

where the n_1 is the row index and $(n_2 \ldots n_L)$ with no comma separation between the quantum numbers is a composite index denoting column.

The matrix $\hat{\Psi}$ can be decomposed into three matrices as shown below

$$\hat{\Psi} = \begin{pmatrix} U_{0,1} & U_{0,2} \\ U_{1,1} & U_{1,2} \end{pmatrix} \begin{pmatrix} S_{1,1} & 0 \\ 0 & S_{2,2} \end{pmatrix} \begin{pmatrix} V_{1,(0\ldots0)} & \cdots & V_{1,(1\ldots1)} \\ V_{2,(0\ldots0)} & \cdots & V_{2,(1\ldots1)} \end{pmatrix} \tag{2.26}$$

$$\equiv USV \tag{2.27}$$

where U is a unitary matrix, meaning $U^\dagger U = 1$, $\hat{S}$ is diagonal and V, also a unitary matrix, is a matrix pertaining to the orbitals $2, \ldots, L$. This method of factoring a matrix is known as singular value decomposition [41]. To clarify the indices of each matrix, the matrix element of U is U_{n_1,i_1}, the matrix element of the diagonal matrix S is S_{i_1,i_1} and the matrix element of V is $V_{i_1,(n_2\ldots n_L)}$. For the next iteration of SVD, the matrices S and V are multiplied together, where the corresponding matrix element is given by $(SV)_{i_1,(n_2\ldots n_L)}$, and reshaped into a matrix whose elements are given by $(SV)_{(i_1 n_2),(n_3\ldots n_L)}$. SVD is then applied to the reshaped SV matrix.

To illustrate the process of obtaining an MPS more concretely, the iterative singular value decomposition will also be applied to a simple many-body system of two electrons on three orbitals in addition to the general case.

Consider the many-body wavefunction of a three orbital system.

$$|\Phi\rangle = \sum_{\mathbf{n}=(0,0,0)}^{(1,\ldots,1)} \phi_{n_1,n_2,n_3} |n_1, n_2, n_3\rangle \tag{2.28}$$

The tensor of wavefunction coefficients for this system with all possible electron numbers is given by

$$\hat{\Phi} = \begin{pmatrix} \phi_{0,(00)} & \phi_{0,(01)} & \phi_{0,(10)} & \phi_{0,(11)} \\ \phi_{1,(00)} & \phi_{1,(01)} & \phi_{1,(10)} & \phi_{1,(11)} \end{pmatrix} \tag{2.29}$$

Here, indices in the subscripts are grouped to denote row and column and have no effect on the actual value of the coefficient itself, i.e. $\phi_{n_1,(n_2n_3)} = \phi_{n_1,n_2,n_3}$. The row index corresponds to the occupation of the first orbital, where the first row contains configurations with the first orbital being empty and the second row contains configurations where the first orbital is occupied. The column index is a composite index starting from (00) that is a two digit binary number that corresponds to the occupations of the second and third orbitals. For example, the index (10), which is the third column, refers to configurations where the second orbital is occupied and the third orbital is empty.

Since we will focus on the two electron case, all other coefficients will be set to zero except for the ones corresponding to two electron configurations. The coefficient tensor for two electrons is given by

$$\hat{\Phi} = \begin{pmatrix} 0 & 0 & 0 & \phi_{0,(11)} \\ 0 & \phi_{1,(01)} & \phi_{1,(10)} & 0 \end{pmatrix} \tag{2.30}$$

which can be decomposed using singular value decomposition as shown below

$$\hat{\Phi} = \begin{pmatrix} 1 & 0 \\ 0 & 1 \end{pmatrix} \begin{pmatrix} |\phi_{011}| & 0 \\ 0 & \sqrt{|\phi_{101}|^2 + |\phi_{110}|^2} \end{pmatrix} \times \begin{pmatrix} 0 & 0 & 0 & \phi_{011}/|\phi_{011}| \\ 0 & \frac{\phi_{101}}{\sqrt{|\phi_{101}|^2+|\phi_{110}|^2}} & \frac{\phi_{110}}{\sqrt{|\phi_{101}|^2+|\phi_{110}|^2}} & 0 \end{pmatrix} \equiv U'S'V' \tag{2.31}$$

Each matrix element of the general many-body wavefunction tensor $\hat{\Psi}$ can be expressed in terms of sums of products of individual matrix elements of U, S and V

$$\psi_{n_1,(n_2\ldots n_L)} = \sum_{i_1=1}^{\chi_1} U_{n_1,i_1} S_{i_1,i_1} V_{i_1,(n_2\ldots n_L)}. \tag{2.32}$$

We can redefine the tensor U as two row vectors A^{n_1} with entries $A^{n_1}_{i_1}$ and multiply the S and V matrices together to obtain the following expression

$$\psi_{n_1,(n_2\ldots n_L)} = \sum_{i_1=1}^{\chi_1} A^{n_1}_{i_1} \psi_{i_1,(n_2\ldots n_L)} \tag{2.33}$$

where $\psi_{i_1,(n_2\ldots n_L)} \equiv S_{i_1,i_1} V_{i_1,(n_2\ldots n_L)}$.

The same expression applied to the two electrons on three orbitals case is given by

$$\begin{aligned} \phi_{n_1,(n_2n_3)} &= \sum_{i_1=1}^{2} A^{n_1\prime}{}_{i_1} \phi_{i_1,(n_2n_3)} \\ &= A^{n_1\prime}{}_1 \phi_{1,(n_2n_3)} + A^{n_1\prime}{}_2 \phi_{2,(n_2n_3)} \end{aligned} \tag{2.34}$$

where the tensor $A^{n_1\prime}$ is the tensor U' reshaped in the same way A^{n_1} is U reshaped from the general case. As an example, the expression for $\phi_{0,(11)}$ using Eq. 2.34 is given by

$$\phi_{0,(11)} = 1 \times \phi_{011} + 0 \times 0 \tag{2.35}$$

which is trivial given the simplicity of the system.

We now have the first tensor in the general MPS A^{n_1} and the two electron MPS $A^{n_1\prime}$. To obtain the other A^{n_k} tensors where $k \in \{2, \ldots, L\}$, singular value decomposition is performed iteratively on $\psi_{i_1,(n_2 \ldots n_L)}$. First, the $2 \times 2^{L-1}$ matrix $\psi_{i_1,(n_2 \ldots n_L)}$ is reshaped into $\psi_{(i_1 n_2),(n_3 \ldots n_L)}$ which is a $4 \times 2^{L-2}$ matrix. For the two electron case, the reshaping of $\phi_{i_1,(n_2 n_3)}$ to $\phi_{(i_1 n_2),n_3}$ is illustrated below

$$\begin{pmatrix} \phi_{0,(00)} & \phi_{0,(01)} & \phi_{0,(10)} & \phi_{0,(11)} \\ \phi_{1,(00)} & \phi_{1,(01)} & \phi_{1,(10)} & \phi_{1,(11)} \end{pmatrix} \xrightarrow{reshape} \begin{pmatrix} \phi_{(00),0} & \phi_{(00),1} \\ \phi_{(01),0} & \phi_{(01),1} \\ \phi_{(10),0} & \phi_{(10),1} \\ \phi_{(11),0} & \phi_{(11),1} \end{pmatrix} \tag{2.36}$$

It is important to note that the first index is i_1 which is the row index of $S'V'$ and not the occupation of the first orbital n_1. However, in this specific example, the indices i_1 and n_1 happen to be equivalent as a consequence of U' in the first singular value decomposition being the identity, which in general is not the case.

The decomposition of $\psi_{(i_1 n_2),(n_3 \ldots n_L)}$ is given by

$$\begin{aligned} \psi_{(i_1 n_2),(n_3 \ldots n_L)} &= \sum_{i_2=1}^{\chi_2} U_{(i_1 n_2),i_2} S_{i_2,i_2} V_{i_2,n_3 \ldots n_L} \\ &= \sum_{i_2=1}^{\chi_2} A^{n_2}_{i_1,i_2} \psi_{(i_2 n_3),(n_4 \ldots n_L)} \end{aligned} \tag{2.37}$$

For the two electron case, the decomposition of $\phi_{(i_1 n_2),n_3}$ is given by

$$\begin{aligned}\begin{pmatrix} \phi_{(00),0} & \phi_{(00),1} \\ \phi_{(01),0} & \phi_{(01),1} \\ \phi_{(10),0} & \phi_{(10),1} \\ \phi_{(11),0} & \phi_{(11),1} \end{pmatrix} &= \begin{pmatrix} 0 & 0 \\ \frac{\phi_{011}}{\sqrt{|\phi_{011}|^2+|\phi_{101}|^2}} & 0 \\ \frac{\phi_{101}}{\sqrt{|\phi_{011}|^2+|\phi_{101}|^2}} & 0 \\ 0 & \phi_{110}/|\phi_{110}| \end{pmatrix} \\ &\times \begin{pmatrix} \sqrt{|\phi_{011}|^2+|\phi_{101}|^2} & 0 \\ 0 & \sqrt{|\phi_{011}|^2+|\phi_{101}|^2} \end{pmatrix} \begin{pmatrix} 0 & 1 \\ 1 & 0 \end{pmatrix} \end{aligned} \tag{2.38}$$

$$\equiv U'' S'' V'' \tag{2.39}$$

where the coefficients $\phi_{n_1 n_2 n_3}$ on the right hand side of the equation with no commas in the subscript are the original coefficients of $|\Phi\rangle$. Again, $U''_{(i_1 n_2),i_2}$ is redefined as two matrices $A^{n_2=0'}$ and $A^{n_2=1'}$ with entries $A^{n_2}_{i_1,i_2}{}'$. For this three orbital system, the iterative singular value decomposition stops here. The final tensor $A^{n_3\prime}$ can be obtained by reshaping the product $S''V''$. We have now obtained the MPS for a system of two electrons on three orbitals, which is given by

$$|\Phi\rangle = \sum_{\mathbf{n}} A^{n_1\prime} A^{n_2\prime} A^{n_3\prime} |n_1, n_2, n_3\rangle \tag{2.40}$$

where the $A^{n_k\prime}$ tensors are

$$\begin{aligned} A^{n_1=0'} &= (1 \quad 0), \qquad A^{n_1=1'} = (0 \quad 1) \\ A^{n_2=0'} &= \begin{pmatrix} 0 & 0 \\ \frac{\phi_{101}}{\sqrt{|\phi_{101}|^2+|\phi_{110}|^2}} & 0 \end{pmatrix}, \quad A^{n_2=1'} = \begin{pmatrix} \frac{\phi_{011}}{\sqrt{|\phi_{101}|^2+|\phi_{110}|^2}} & 0 \\ 0 & \phi_{110}/|\phi_{110}| \end{pmatrix} \\ A^{n_3=0'} &= \begin{pmatrix} 0 \\ |\phi_{110}| \end{pmatrix}, \quad A^{n_3=1'} = \begin{pmatrix} \sqrt{|\phi_{101}|^2+|\phi_{110}|^2} \\ 0 \end{pmatrix} \end{aligned}$$

For the general case, the singular value decomposition continues to iterate until

all orbital dependent tensors A^{n_k} are obtained. As in the case for two electrons on three orbitals, $U_{(i_1 n_2),i_2}$ is redefined as two matrices A^{n_2} with entries $A^{n_2}_{i_1,i_2}$ in the same way. Likewise as in Eq. 2.33, the S and V matrices is multiplied and then reshaped for another singular value decomposition.

$$\psi_{i_2,(n_3 \ldots n_L)} \xrightarrow{reshape} \psi_{(i_2 n_3),(n_4 \ldots n_L)}$$

$$\psi_{(i_2 n_3),(n_4 \ldots n_L)} = \sum_{i_3=1}^{\chi_3} U_{(i_2 n_3),(i_3)} S_{i_3,i_3} V_{i_3,(n_4 \ldots n_L)} \tag{2.41}$$

$$= \sum_{i_3=1}^{\chi_3} A^{n_3}_{i_2,i_3} \psi_{(i_3 n_4),(n_5 \ldots n_L)} \tag{2.42}$$

Substituting Eqns. 2.37 and 2.42 into Eq. 2.33, we get the following expression for the wavefunction coefficient

$$\psi_{n_1,n_2 \ldots n_L} = \sum_{i_1=1}^{\chi_1} \sum_{i_2=1}^{\chi_2} \sum_{i_3=1}^{\chi_3} A^{n_1}_{i_1} A^{n_2}_{i_1,i_2} A^{n_3}_{i_2,i_3} \psi_{(i_3 n_4),(n_5 \ldots n_L)} \tag{2.43}$$

Through iterative application of the singular value decomposition, we arrive at a general expression for the matrix product state

$$|\Psi\rangle = \sum_{\mathbf{n}} \sum_{i_1=1}^{\chi_1} \cdots \sum_{i_k=1}^{\chi_k} \cdots \sum_{i_{L-1}=1}^{\chi_{L-1}} A^{n_1}_{i_1} \cdots A^{n_k}_{i_{k-1},i_l} \cdots A^{n_L}_{i_{L-1}} |n_1, \ldots, n_L\rangle$$

$$= \sum_{\mathbf{n}} A^{n_1} \cdots A^{n_L} |n_1, \ldots, n_L\rangle \tag{2.44}$$

The form of the MPSs in Eqs. 2.44 and 2.40 is known as left-canonical form. In this form, each tensor A^{n_k} in $|\Psi\rangle$, as well as $A^{n_k\prime}$ in $|\Phi\rangle$, has the following normalization feature

$$\sum_{n_k} A^{n_k \dagger} A^{n_k} = I \tag{2.45}$$

because the A^{n_k} tensors are reshaped unitaries from the SVD. Of course, the right most tensor A^{n_L} does not satisfy this condition, but can be made to if a normalization constant is factored out.

It is important to note that MPS representations are non-unique. For example, the identity in the form of $XX^{-1} = 1$ can be inserted between tensors A^{n_k} and $A^{n_{k+1}}$ leading to new tensors $M^{n_k} \equiv A^{n_k}X$ and $M^{n_{k+1}} \equiv X^{-1}A^{n_{k+1}}$ to be defined. These types of transformations introduce a gauge degree of freedom. Due to this non-uniqueness, the wavefunction can be expressed as an MPS that does not assume any type of canonicalization, i.e. does not assume a normalization condition of the type in Eq. 2.45. A more general expression of an MPS that is still equivalent to Eq. 2.23 is given by

$$\begin{aligned} |\Psi\rangle &= \sum_{\mathbf{n}} M^{n_1} \cdots M^{n_L} |n_1, \ldots, n_L\rangle \\ &= \sum_{\mathbf{n}} \sum_{i_1=1}^{\chi_1} \cdots \sum_{i_{L-1}=1}^{\chi_{L-1}} M^{n_1}_{i_1} \cdots M^{n_k}_{i_{k-1},i_k} \cdots M^{n_L}_{i_{L-1}} |n_1, \ldots, n_L\rangle \end{aligned} \tag{2.46}$$

The advantage of expressing the wavefunction as a product of orbital dependent tensors, i.e. expressing the wavefunction as an MPS, is that the wavefunction is encoded in L tensors instead of 2^L complex numbers. To show the reduction in complexity using MPS, say a threshold for singular values ε is set such that any $S_{i_k,i_k} < \varepsilon$ are discarded. This brings the maximum dimension of all of the M^{n_k} tensors, which we will call m to be much less than the maximum dimension χ_{MAX} which is the maximum without any truncation. The term for this maximum dimension m is the bond dimension of the MPS. With this approximation, the number of terms in the wavefunction is now $O(2m^2L)$ instead of $O(2^L)$ which is linear in the number of orbitals instead of exponential, greatly reducing the storage required for the wavefunction.

Another ingredient in the DMRG algorithm is to transform a general MPS into left-canonicalized form and another form that has yet to be introduced, the right-canonicalized form.

To bring Eq. 2.46 into left-canonicalized form, SVD can be applied iteratively on each M^{n_k} starting from the left most tensor and sweeping through to the right as shown below, starting with the reshaping of row vector $M^{n_1}_{i_1}$ into the matrix M_{n_1,i_1}.

$$
\begin{aligned}
\psi_{n_1,\ldots,n_L} &= \sum_{i_1,\ldots} M_{n_1,i_1} M^{n_2}_{i_1,i_2} M^{n_3}_{i_2,i_3} \ldots \\
&= \sum_{i_1,\ldots} \left(\sum_{j_1} U_{n_1,j_1} S_{j_1,j_1} V_{j_1,i_1} \right) M^{n_2}_{i_1,i_2} M^{n_3}_{i_2,i_3} \ldots \\
&= \sum_{i_2,\ldots} \sum_{j_1} A^{n_1}_{j_1} \left(\sum_{i_1} S_{j_1,j_1} V_{j_1,i_1} M^{n_2}_{i_1,i_2} \right) M^{n_3}_{i_2,i_3} \ldots \\
&= \sum_{i_2,\ldots} \sum_{j_1} A^{n_1}_{j_1} N^{n_2}_{j_1,i_2} M^{n_3}_{i_2,i_3} \ldots \\
&= \sum_{i_2,\ldots} \sum_{j_1} A^{n_1}_{j_1} \left(\sum_{j_2} U_{(n_2 j_1),j_2} S_{j_2,j_2} V_{j_2,i_2} \right) M^{n_3}_{i_2,i_3} \ldots \\
&= \sum_{i_3,\ldots} \sum_{j_1} \sum_{j_2} A^{n_1}_{j_1} A^{n_2}_{j_1,j_2} \left(\sum_{i_2} S_{j_2,j_2} V_{j_2,i_2} M^{n_3}_{i_2,i_3} \right) \ldots \\
&= \sum_{i_3,\ldots} \sum_{j_1} \sum_{j_2} A^{n_1}_{j_1} A^{n_2}_{j_1,j_2} N^{n_3}_{j_2,i_3} \ldots \\
&\qquad\qquad \ldots \\
&= \sum_{\mathbf{j}} A^{n_1}_{j_1} A^{n_2}_{j_1,j_2} \cdots A^{n_L}_{j_{L-1}}
\end{aligned}
\tag{2.47}
$$

The result is an MPS in left-canonicalized form, which means that the normalization condition in Eq. 2.45 is satisfied. To obtain the right-canonicalized form, the process is similar except the SVD sweep goes from right to left as shown below. The process begins with reshaping the matrix $M^{n_L}_{i_{L-1}}$ to M_{i_{L-1},n_L}.

$$
\begin{aligned}
\psi_{n_1,\ldots,n_L} &= \sum_{\ldots,i_{L-1}} \ldots M^{n_{L-2}}_{i_{L-3},i_{L-2}} M^{n_{L-1}}_{i_{L-1},i_{L-2}} M_{i_{L-1},n_L} \\
&= \sum_{\ldots,i_{L-1}} \ldots M^{n_{L-2}}_{i_{L-3},i_{L-2}} M^{n_{L-1}}_{i_{L-1},i_{L-2}} \left(\sum_{j_{L-1}} U_{i_{L-1},j_{L-1}} S_{j_{L-1},j_{L-1}} V_{j_{L-1},n_L} \right) \\
&= \sum_{\ldots,i_{L-2}} \sum_{j_{L-1}} \ldots M^{n_{L-2}}_{i_{L-3},i_{L-2}} \left(\sum_{i_{L-1}} M^{n_{L-1}}_{i_{L-1},i_{L-2}} U_{i_{L-1},j_{L-1}} S_{j_{L-1},j_{L-1}} \right) B^{n_L}_{j_{L-1}} \\
&= \sum_{\ldots,i_{L-2}} \sum_{j_{L-1}} \ldots M^{n_{L-2}}_{i_{L-3},i_{L-2}} N^{n_{L-1}}_{i_{L-2},j_{L-1}} B^{n_L}_{j_{L-1}} \\
&= \sum_{\ldots,i_{L-2}} \sum_{j_{L-1}} \ldots M^{n_{L-2}}_{i_{L-3},i_{L-2}} \left(\sum_{j_{L-2}} U_{i_{L-2},j_{L-2}} S_{j_{L-2},j_{L-2}} V_{j_{L-2},(n_{L-1} j_{L-1})} \right) B^{n_L}_{j_{L-1}} \\
&= \sum_{\ldots,i_{L-3}} \sum_{j_{L-1}} \sum_{j_{L-2}} \ldots N^{n_{L-2}}_{i_{L-3},j_{L-2}} B^{n_{L-1}}_{j_{L-2},j_{L-1}} B^{n_L}_{j_{L-1}} \\
&\qquad\qquad \ldots \\
&= \sum_{\mathbf{j}} B^{n_1}_{j_1} B^{n_2}_{j_1,j_2} \cdots B^{n_L}_{j_{L-1}}
\end{aligned}
\tag{2.48}
$$

Eq. 2.48 is the MPS in right-canonicalized form where a normalization condition similar to Eq. 2.45 is satisfied as shown below

$$
\sum_{n_k} B^{n_k} B^{n_k \dagger} = I \tag{2.49}
$$

where the complex conjugate is multiplied on the right instead of the left. Again, the left most tensor B^{n_1} can be made to satisfy this condition if a normalization constant is factored out.

The next part is expressing the Hamiltonian as a matrix product operator (MPO) just as the wavefunction was expressed as an MPS.

2.2.4 Matrix Product Operators

A matrix product operator (MPO) is a form of an operator whereby each matrix element is expressed as a product of orbital dependent tensors in the same way an MPS is a form of a wavefunction where each coefficient is expressed as a product of orbital dependent tensors. The matrix element of an MPO is given by

$$\langle n'_1 \dots n'_L | O | n_1 \dots n_L \rangle = \sum_{\mathbf{i}} G_{i_1}^{n_1,n'_1} G_{i_1,i_2}^{n_2,n'_2} \dots G_{i_{L-1}}^{n_L,n'_L} \tag{2.50}$$

where each $G_{i_{k-1},i_k}^{n_k,n'_k}$ is a matrix element of a matrix G^{n_k,n'_k} pertaining to the k^{th} orbital. The G^{n_k,n'_k} matrices in the MPO matrix element are analogous to the M^{n_k} matrices in the MPS wavefunction coefficients Eq. 2.46.

To begin the derivation of the MPO, we will use a two-body operator in second quantization as a starting point given by

$$O = \sum_{i=1}^{L} \sum_{j=1}^{L} \sum_{k=1}^{L} \sum_{l=1}^{L} \langle i,j|O|k,l\rangle c_i^\dagger c_j^\dagger c_k c_l \tag{2.51}$$

where i, j, k and l denote orbitals and there are L orbitals in total. First, it is standard practice in the MPO formalism to express each term as a tensor product of site operators [36, 42]. For example, in a bosonic Hamiltonian in the basis of L single particle states, the term $a_1^\dagger a_4$ expressed as a tensor product of site operators is given by

$$a_1^\dagger a_4 = a^\dagger \otimes I \otimes I \otimes a \otimes I \otimes \dots \otimes I \tag{2.52}$$

where $a^\dagger$ (a) is the bosonic creation (annihilation) operator and I is the identity operator.

Since we are dealing with fermionic operators, we need to introduce a negative analogue to the identity, I^-, so the anticommutation relations are satisfied. To do

this, the following definitions are made.

$$|0\rangle \equiv \begin{pmatrix} 0 \\ 1 \end{pmatrix} \qquad \text{and} \qquad |1\rangle \equiv \begin{pmatrix} 1 \\ 0 \end{pmatrix} \tag{2.53}$$

where $|0\rangle$ and $|1\rangle$ represent an occupied and unoccupied orbital respectively.

This representation of the occupation basis leads to the following representations of the fermionic operators

$$c = \begin{pmatrix} 0 & 1 \\ 0 & 0 \end{pmatrix} \qquad c^\dagger = \begin{pmatrix} 0 & 0 \\ 1 & 0 \end{pmatrix}. \tag{2.54}$$

The definition of the fermion analogue to the identity I^- is given by

$$I^- \equiv \begin{pmatrix} 1 & 0 \\ 0 & -1 \end{pmatrix}. \tag{2.55}$$

Using these definitions, the fermion operator for site k is given by

$$\begin{aligned} c_k^{(\dagger)} &= I^- \otimes \cdots \otimes I^- \otimes c^{(\dagger)} \otimes I \otimes \cdots \otimes I \\ &= \left(\bigotimes_{i=1}^{k-1} I^- \right) \otimes c^{(\dagger)} \otimes \left(\bigotimes_{i=k+1}^{L} I \right) \end{aligned} \tag{2.56}$$

where $c^{(\dagger)}$ is in the k^{th} position of the tensor product.

We can now express a term in Eq. 2.51, say $c_1^\dagger c_3^\dagger c_4 c_6$, as a tensor product or site operators

$$c_1^\dagger c_3^\dagger c_4 c_6 = c^\dagger I^- \otimes I^- \otimes c^\dagger \otimes c \otimes I^- \otimes c \otimes I \otimes \cdots \otimes I \tag{2.57}$$

The sum of two MPOs can also be expressed as product of orbital dependent tensors. For an operator $R = A + B$, where $A = A_1 \otimes A_2 \otimes \cdots \otimes A_L$ and $B =$

$B_1 \otimes B_2 \otimes \cdots \otimes B_L$, the sum can be expressed as

$$R = \begin{pmatrix} A_1 & B_1 \end{pmatrix} \begin{pmatrix} A_2 & 0 \\ 0 & B_2 \end{pmatrix} \cdots \begin{pmatrix} A_{L-1} & 0 \\ 0 & B_{L-1} \end{pmatrix} \begin{pmatrix} A_L \\ B_L \end{pmatrix} \tag{2.58}$$

where A_i (B_i) is the orbital dependent tensor for orbital i [42].

To obtain the MPO for Eq. 2.51, we start with the first two terms

$$\begin{aligned} T_1 &= \langle 1,1|O|1,1\rangle c^\dagger c^\dagger cc + \langle 1,1|O|1,2\rangle c^\dagger c^\dagger cc \\ &= \langle 1,1|O|1,1\rangle \left(c^\dagger c^\dagger cc \otimes I \otimes I \ldots\right) + \langle 1,1|O|1,2\rangle \left(c^\dagger c^\dagger cI^- \otimes c \otimes I \ldots\right) \\ &= \begin{pmatrix} \langle 1,1|O|1,1\rangle c^\dagger c^\dagger cc & \langle 1,1|O|1,2\rangle c^\dagger c^\dagger cI^- \end{pmatrix} \begin{pmatrix} I & 0 \\ 0 & c \end{pmatrix} \begin{pmatrix} I & 0 \\ 0 & I \end{pmatrix} \cdots \\ &= W_1^{[1]} W_1^{[2]} \ldots W_1^{[L]} \end{aligned} \tag{2.59}$$

where

$$W_1^{[1]} = \begin{pmatrix} \langle 1,1|O|1,1\rangle c^\dagger c^\dagger cc & \langle 1,1|O|1,2\rangle c^\dagger c^\dagger cI^- \end{pmatrix},$$
$$W_1^{[2]} = \begin{pmatrix} I & 0 \\ 0 & c \end{pmatrix}$$

and

$$W_1^{[3]} = \begin{pmatrix} I & 0 \\ 0 & c \end{pmatrix} \qquad \text{for} \qquad 3 \leq k \leq L \tag{2.60}$$

Since each site specific fermionic operator, as well as the identity, can be represented as a 2×2 matrix in the occupation basis, the matrix element of T_1 in the basis of

configurations is given by

$$\langle \mathbf{n}' | T_1 | \mathbf{n} \rangle = W_1^{n_1,n_1'} W_1^{n_2,n_2'} \dots W_1^{n_L,n_L'} \tag{2.61}$$

where $n_k(n_k') \in \{0,1\}$ for $1 \leq k \leq L$. Note that we have now dropped the superscripts in the square brackets from Eq. 2.59 since the tensor element $W_1^{n_k,n_k'}$ is defined by the order in which it appears in the multiplication.

So far, we have obtained an MPO for the first two terms of the Hamiltonian. We must now deal with the remaining terms. For every two terms, a T_i MPO can be constructed which would result in $\frac{L}{2}$ T_i MPOs. The same addition process can be applied, but now for the $T_i^{(1)}$ tensors. The first step would be to construct a $T_1^{(1)}$ tensor where $T_1^{(1)} = T_1 + T_2$, but now, each tensor has a larger bond dimension. At this stage, the iterative SVD can be applied from left to right, from $T_1^{(1);n_1,n_1'}$ to $T_1^{(1);n_L,n_L'}$ to lower the bond dimension by discarding negligible singular values in the exact same way it was done for the MPS in Eq. 2.47. Of course, for every singular value S_{q_k,q_k} that is removed, a column and row from the $U^{n_k'}_{(n_k q_{k-1}),q_k}$ and V_{q_k,i_k} matrices respectively must also be removed. The iterative SVD process for the tensor $T_1^{(1);n_L,n_L'}$ is shown below

$$
\begin{aligned}
\langle \mathbf{n}|T_1^{(1)}|\mathbf{n}'\rangle &= \sum_{i_1,i_2,\ldots} W_{i_1}^{(1);n_1,n_1'} W_{i_1,i_2}^{(1);n_2,n_2'} \ldots W_{i_{L-1}}^{(1);n_L,n_L'} \\
&= \sum_{i_1\ldots} W_{n_1,i_1}^{(1);n_1'} W_{i_1,i_2}^{(1);n_2,n_2'} \ldots W_{i_{L-1}}^{(1);n_L,n_L'} \\
&= \sum_{i_1\ldots}\sum_{q_1} \left(U_{n_1,q_1}^{n_1'} S_{q_1} V_{q_1,i_1}\right) W_{i_1,i_2}^{(1);n_2,n_2'} \ldots \\
&= \sum_{i_2\ldots}\sum_{q_1} X_{q_1}^{n_1,n_1'} \left(\sum_{i_1} S_{q_1} V_{q_1,i_1} W_{i_1,i_2}^{(1);n_2,n_2'}\right) \ldots \\
&= \sum_{i_2\ldots}\sum_{q_1} X_{q_1}^{n_1,n_1'} \left(\sum_{q_2} U_{(n_2q_1),q_2}^{n_2'} S_{q_2,q_2} V_{q_2,i_2}\right) W_{i_2,i_3}^{(1);n_3,n_3'} \ldots \\
&= \sum_{i_3\ldots}\sum_{q_1}\sum_{q_2} X_{q_1}^{n_1,n_1'} X_{q_1,q_2}^{n_2,n_2'} \left(\sum_{i_2} S_{q_2,q_2} V_{q_2,i_2} W_{i_2,i_3}^{(1);n_3,n_3'}\right) \ldots \\
&\qquad\qquad \ldots \\
&= \sum_{q_1,\ldots,q_{L-1}} X_{q_1}^{n_1,n_1'} X_{q_1,q_2}^{n_2,n_2'} \ldots X_{q_{L-1}}^{n_L,n_L'}
\end{aligned}
\tag{2.62}
$$

This iterative SVD process is applied to all of the $T_j^{(1)}\ \forall\ j$ tensors and then once again, every two terms are added using the MPO sum method, which would lead to $T_j^{(2)}$ terms where, for example, $T_1^{(2)} = T_1^{(1)} + T_2^{(1)}$ and $T_2^{(2)} = T_3^{(1)} + T_4^{(1)}$. The iterative SVD is applied once again, but now to the $T_j^{(2)}$ tensors. This process of adding MPOs and then applying iterative SVD to the "chain" of orbitals is iteratated until all of the terms are added. The final result is an MPO with a complexity much lower than the full many-body operator, which is given below

$$
O = \sum_{\mathbf{n},\mathbf{n}'}\sum_{\mathbf{i}}^{\vec{\chi}} G_{i_1}^{n_1,n_1'} G_{i_1,i_2}^{n_2,n_2'} \ldots G_{i_{L-1}}^{n_L,n_L'} |\mathbf{n}\rangle\langle\mathbf{n}'| \tag{2.63}
$$

where $\vec{\chi} \equiv (\chi_1, \ldots, \chi_{L-1})$ and $\chi_{\text{MAX}} = m$ is the bond dimension. The number of matrix elements reduces drastically from $2^L \times 2^L$ for the full many-body operator to $O(4m^2L)$ for the final MPO, provided m is relatively small.

So far, we have obtained an MPS approximation of a wavefunction and an MPO

approximation of a many-body operator. The implementation of the DMRG algorithm to obtain the ground state requires both of these ingredients, which will be discussed in the next section.

2.2.5 The Tensor Network Formalism of Density Matrix Renormalization Group

So far, it has been shown using SVD that an MPS approximation of a wavefunction scales linearly with system size as $O(2m^2L)$. Likewise, it has been shown that an MPO approximation of an operator also scales linearly with the system size as $O(4m^2L)$. The density matrix renormalization group (DMRG) algorithm exploits this linear scaling of the Hilbert space of low-entropy systems in order to obtain the ground state of large many-body systems variationally.

The aim of the DMRG algorithm is to solve the following equation using the variational method

$$\langle\Psi|H|\Psi\rangle - E\langle\Psi|\Psi\rangle = 0 \tag{2.64}$$

Before we outline this process, we will introduce the graphical representation of tensor networks.

2.2.6 Graphical Representation of Tensor Networks

A tensor network is a tensor that is factorized into a product of a network of tensors. Matrix product states and matrix product operators are both examples of tensor networks. I will introduce a graphical notation for tensor networks popularized by Chan and Schollwock [36, 43]. The graphical notation helps keep track of which indices are summed over since tensor network expressions usually contain products of many tensors and many indices. It is also useful when taking derivatives of a tensor network. Before we apply the graphical notation to MPS and MPOs, I will go over

the rules.

First, a single tensor is represented as a node with legs, where each leg represents an index and hence, the number of legs equals the rank of the tensor as shown in Fig. 2.2. The actual shape and colour of the node and the placement of legs on the node do not matter.

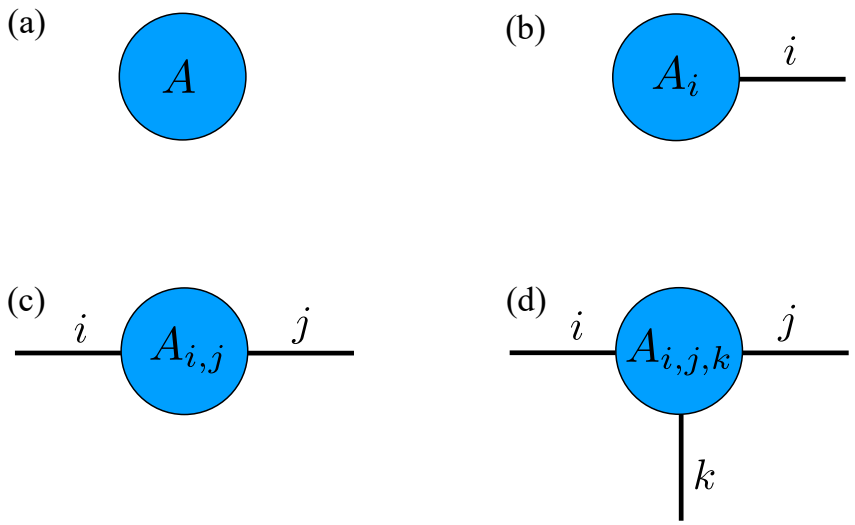

Figure 2.2: Graphical representations of tensors of different ranks: A scalar (rank 0) (a), a vector (rank 1) (b), a matrix (rank 2) (c) and a rank 3 tensor (d). Indices are labeled.

The multiplication of tensors is represented by the connection of legs. When legs are connected, the index corresponding to that leg is summed over. The example in Fig. 2.3 shows the multiplication of two matrices $A_{i,j}$ and $B_{i,j}$.

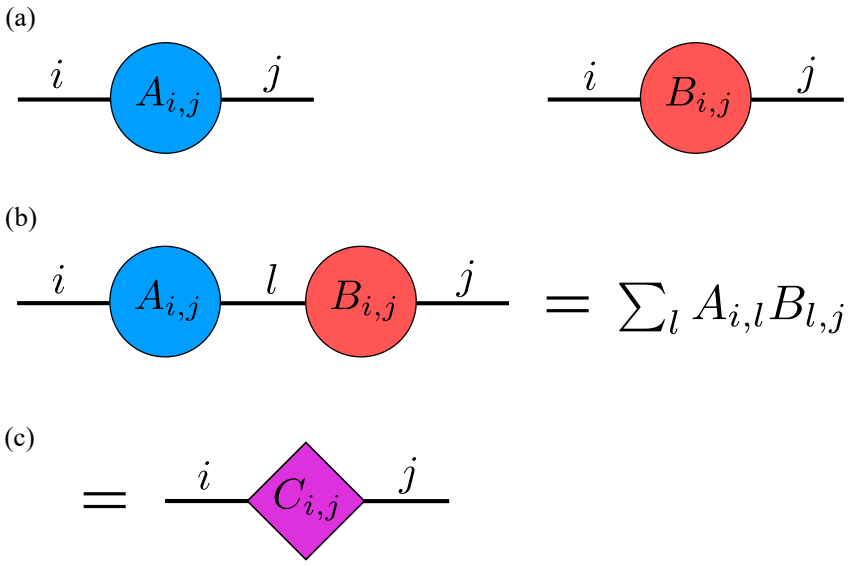

Figure 2.3: Multiplication and contraction of two matrices. Two matrices A and B (a). Matrix product AB (b). The contraction of tensors $C = AB$ (c).

Furthermore, if tensors have a closed connection between them such as in Fig. 2.3 (b), the tensors can be contracted into a single tensor as shown in Fig. 2.3 (c).

We can apply these rules to construct a graphical representations of an MPS and an MPO as shown in Fig. 2.4.

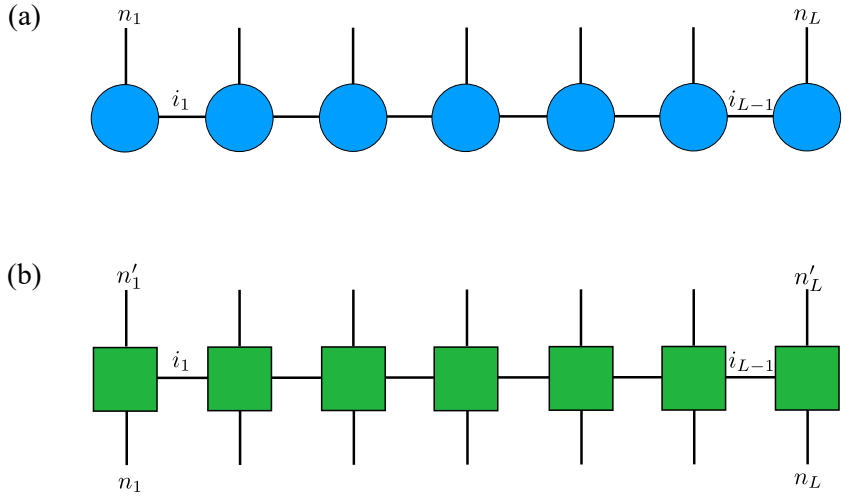

Figure 2.4: Graphical representations of tensor networks. Matrix product state (a) and a matrix product operator (b)

Although the placement of legs does not affect the mathematical expression of the tensor network, it is convention to have the physical indices, that is the indices corresponding to quantum numbers, pointing vertically, while the bond indices are horizontal. The graphical representation helps keep track of which indices are summed

over, since those indices are represented by connected legs.

It also helps with writing expressions for derivatives of tensor networks. Consider the example of $\langle\Psi|O|\Psi\rangle$. The tensor network representation is obtained by combining Eqs. 2.46 and 2.63 and is given by

$$\begin{aligned}\langle\Psi|O|\Psi\rangle &= \left(\sum_{\mathbf{n}'}\langle\mathbf{n}'|M^{n'_L\dagger}\dots M^{n'_1\dagger}\right)\left(\sum_{\mathbf{m},\mathbf{m}'} G^{m'_1,m_1}\dots G^{m'_L,m_L}|\mathbf{m}\rangle\langle\mathbf{m}'|\right)\times \\ &\quad \left(\sum_{\mathbf{n}} M^{n_1}\dots M^{n_L}|\mathbf{n}\rangle\right) \\ &= \sum_{\mathbf{n},\mathbf{n}'}\sum_{\mathbf{i}'}\sum_{\mathbf{j}}\sum_{\mathbf{i}} M^{n'_1*}_{i'_1}\dots M^{n'_L*}_{i'_{L-1}} G^{n'_1,n_1}_{j_1}\dots G^{n'_L,n_L}_{j_{L-1}} M^{n_1}_{i_1}\dots M^{n_L}_{i_{L-1}}. \end{aligned} \tag{2.65}$$

The derivative of the expectation value of O with respect to a tensor element $M^{n'_k*}_{i'_{k-1},i'_k}$ is given by the following expression.

$$\begin{aligned}\frac{\partial}{\partial M^{n'_k*}_{i'_{k-1},i'_k}}\langle\Psi|O|\Psi\rangle &= \sum_{\tilde{\mathbf{n}}',\tilde{\mathbf{i}}'}\sum_{\mathbf{n},\mathbf{j},\mathbf{i}} M^{n'_1*}_{i'_1}\dots M^{n'_{k-1}*}_{i'_{k-2},i'_{k-1}} M^{n'_{k+1}*}_{i'_k,i'_{k+1}}\dots M^{n'_L*}_{i'_{L-1}}\times \\ &\quad G^{n'_1,n_1}_{j_1}\dots G^{n'_k,n_k}_{j_{k-1},j_k}\dots G^{n'_L,n_L}_{j_{L-1}} M^{n_1}_{i_1}\dots M^{n_L}_{i_{L-1}}\end{aligned} \tag{2.66}$$

Here, $\tilde{\mathbf{n}}' \equiv \mathbf{n}' - \{n'_k\}$, $\tilde{\mathbf{i}}' \equiv \mathbf{i}' - \{i'_{k-1}, i'_k\}$ and $\mathbf{j} \equiv \{j_p \quad | \quad 1 \leq p \leq L\}$.

Since Eq. 2.66 is a long expression with many indices, it is difficult to keep track of which ones are not summed over. Graphically, taking the derivative is equivalent to removing a node from the diagram in Fig. 2.5(a) which is shown in Fig. 2.5(b).

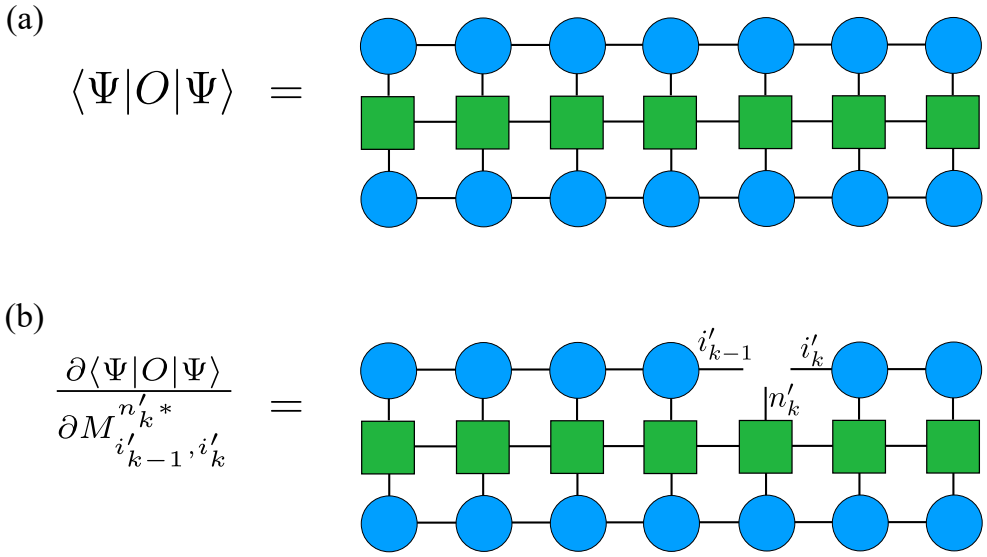

Figure 2.5: Graphical representations of the expectation value of O (a) and its derivative with respect to orbital k (b).

So far, we have learned how to create an MPS and MPO using iterative SVD. We have also learned about the graphical representation of tensor networks and how to take a derivative of a tensor network with respect to a tensor element. All of these concepts will be put together in the DMRG algorithm when computing the ground state.

2.2.7 The DMRG Algorithm

Recall that the variational method of obtaining the ground state consists of minimizing Eq. 2.64 with respect to tensor elements $M^{n'_k *}_{i_{k-1},i_k}$. The goal of the algorithm is obtain a solution to the following system of equations

$$\frac{\partial}{\partial M^{n'_k *}_{i_{k-1},i_k}} \left(\langle\Psi|H|\Psi\rangle - E\langle\Psi|\Psi\rangle\right) = 0 \tag{2.67}$$

for all tensor elements of $\{M^{n_k} \quad | \quad 1 \leq k \leq L\}$. Doing so will result in an eigenvalue problem that can be solved using a traditional diagonalization routine such as Lanczos. Before explaining the steps of the algorithm, I will demonstrate how to reduce Eq. 2.67 to an eigenvalue problem. Recall that the expression for the derivative of $\langle\Psi|H|\Psi\rangle$ was already obtained in Eq. 2.66, where the operator O in this

case is the Hamiltonian H. All of the nodes in this tensor network except for the node $M^{n_k}_{i_{k-1},i_k}$ can be contracted into a single node which we will call the superblock Hamiltonian whose tensor element is $\tilde{H}^{n'_k,n_k}_{i'_{k-1},i'_k,i_{k-1},i_k}$. The graphical representation of the $\frac{\partial}{\partial M^{n'_k*}_{i'_{k-1},i'_k}}\langle\Psi|H|\Psi\rangle$ is given by

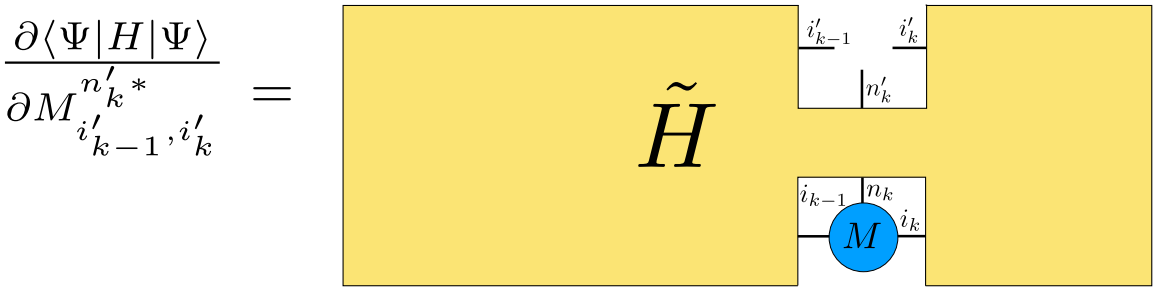

Figure 2.6: $\frac{\partial}{\partial M^{n'_k*}_{i'_{k-1},i'_k}}\langle\Psi|H|\Psi\rangle$ in terms of the superblock $\tilde{H}$ and site k.

which is equivalent to the following expression

$$\frac{\partial}{\partial M^{n'_k*}_{i'_{k-1},i'_k}}\langle\Psi|H|\Psi\rangle = \sum_{n_k}\sum_{i_{k-1},i_k}\tilde{H}^{n'_k,n_k}_{i'_{k-1},i'_k,i_{k-1},i_k}M^{n_k}_{i_{k-1},i_k} \tag{2.68}$$

The expression for the superblock Hamiltonian is given by

$$\begin{aligned}\tilde{H}^{n'_k,n_k}_{i'_{k-1},i'_k,i_{k-1},i_k} \equiv \sum_{\tilde{\mathbf{n}}',\tilde{\mathbf{n}}}\sum_{\tilde{\mathbf{i}}',\tilde{\mathbf{i}}}\sum_{\mathbf{j}} M^{n'_1*}_{i'_1}\ldots M^{n'_{k-1}*}_{i'_{k-2},i'_{k-1}}M^{n'_{k+1}*}_{i'_k,i'_{k+1}}\ldots M^{n'_L*}_{i'_{L-1}}\times \\ G^{n'_1,n_1}_{j_1}\ldots G^{n'_L,n_L}_{j_{L-1}}M^{n_1}_{i_1}\ldots M^{n_{k-1}}_{i_{k-2},i_{k-1}}M^{n_{k+1}}_{i_k,i_{k+1}}\ldots M^{n_L}_{i_{L-1}}\end{aligned} \tag{2.69}$$

where $\tilde{\mathbf{i}} \equiv \mathbf{i} - \{i_{k-1}, i_k\}$ and $\tilde{\mathbf{i}}' = \mathbf{i}' - \{i'_{k-1}, i'_k\}$. The superblock Hamiltonian is equivalent to removing the M^{n_k} and $M^{n'_k*}$ nodes from the $\langle H\rangle$ tensor network.

To compute the overlap derivative $\frac{\partial}{\partial M^{n'_k*}_{i'_{k-1},i'_k}}\langle\Psi|\Psi\rangle$, the tensors left of the M^{n_k} node are contracted to a tensor L and the tensors right of said node to a tensor R as shown graphically in Fig. 2.7.

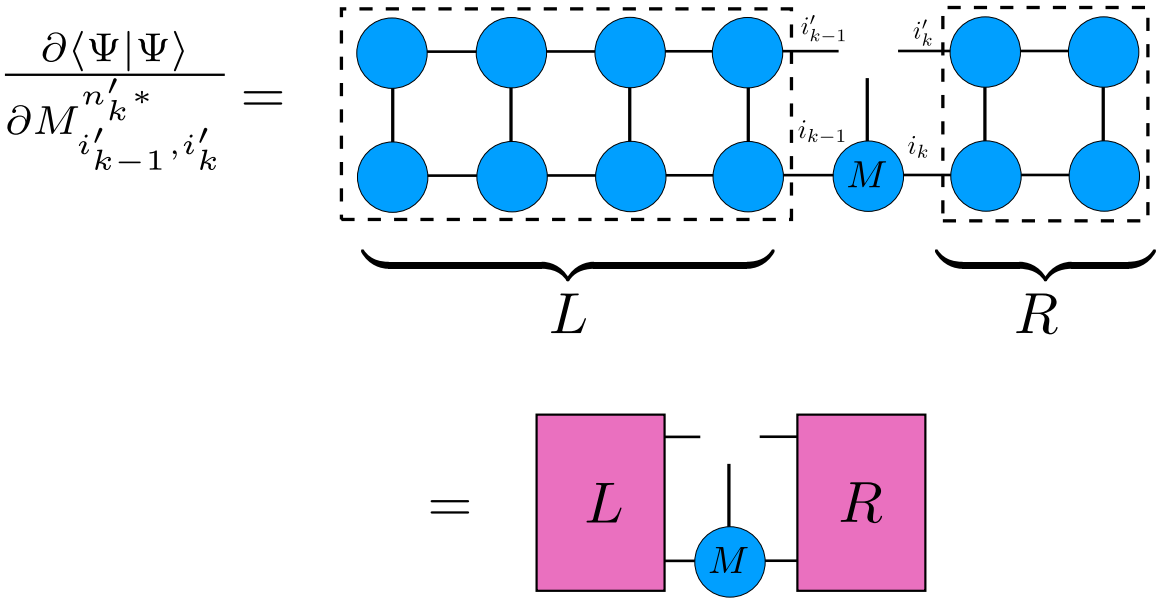

Figure 2.7: Derivative of the overlap. The tensors to the left of M^{n_k} are contracted to a tensor L and the ones to the right are contracted to a tensor R.

The expression of the overlap derivative in terms of L and R is given by

$$\frac{\partial}{\partial M^{n'_k *}_{i'_{k-1},i'_k}}\langle\Psi|\Psi\rangle = \sum_{i_{k-1},i_k} L_{i'_{k-1},i_{k-1}} M^{n_k}_{i_{k-1},i_k} R_{i'_k,i_k} \tag{2.70}$$

where $L_{i'_{k-1},i_{k-1}}$ is given by

$$L_{i'_{k-1},i_{k-1}} = \sum_{n_1,\ldots,n_{k-1}} \sum_{i_1,\ldots,i_{k-2}} \sum_{i'_1,\ldots,i'_{k-2}} M^{n_1 *}_{i'_k} M^{n_1}_{i_k} \ldots M^{n_k *}_{i'_{k-2},i'_{k-1}} M^{n_k}_{i_{k-2},i_{k-1}} \tag{2.71}$$

and $R_{i'_k,i_k}$ is given by

$$R_{i'_k,i_k} = \sum_{n_{k+1},\ldots,n_L} \sum_{i_k,\ldots,i_{L-1}} \sum_{i'_k,\ldots,i'_{L-1}} M^{n_{k+1} *}_{i'_{k-2},i'_{k-1}} M^{n_{k+1}}_{i_{k-2},i_{k-1}} \ldots M^{n_L *}_{i'_{L-1}} M^{n_L}_{i_{L-1}} \tag{2.72}$$

Let us assume that the tensors in L are all left-normalized as in Eq. 2.45 and the tensors in R are right-normalized as in Eq. 2.48. Then both L and R become identity matrices. The proof of $L = I$ is given below. Because the M tensors in L are

left-normalized, they are replaced with A tensors.

$$
\begin{aligned}
L_{i'_{k-1},i_{k-1}} &= \sum_{n_2,\ldots,n_{k-1}} \sum_{i_1,\ldots,i_{k-2}} \sum_{i'_1,\ldots,i'_{k-2}} \left(\sum_{n_1} A^{n_1 *}_{i'_1} A^{n_1}_{i_1} \right) A^{n_2 *}_{i'_1,i'_2} A^{n_2}_{i_1,i_2} \ldots A^{n_{k-1} *}_{i'_{k-2},i'_{k-1}} A^{n_{k-1}}_{i_{k-2},i_{k-1}} \\
&= \sum_{n_2,\ldots,n_{k-1}} \sum_{i_1,\ldots,i_{k-2}} \sum_{i'_1,\ldots,i'_{k-2}} \delta_{i'_1,i_1} A^{n_2 *}_{i'_1,i'_2} A^{n_2}_{i_1,i_2} \ldots A^{n_{k-1} *}_{i'_{k-2},i'_{k-1}} A^{n_{k-1}}_{i_{k-2},i_{k-1}} \\
&= \sum_{n_3,\ldots,n_{k-1}} \sum_{i_2,\ldots,i_{k-2}} \sum_{i'_2,\ldots,i'_{k-2}} \left(\sum_{n_2,i_1} A^{n_2 *}_{i_1,i'_2} A^{n_2}_{i_1,i_2} \right) A^{n_3 *}_{i'_2,i'_3} A^{n_3}_{i_2,i_3} \ldots A^{n_{k-1} *}_{i'_{k-2},i'_{k-1}} A^{n_{k-1}}_{i_{k-2},i_{k-1}} \\
&= \sum_{n_3,\ldots,n_{k-1}} \sum_{i_2,\ldots,i_{k-2}} \sum_{i'_2,\ldots,i'_{k-2}} \delta_{i'_2,i_2} A^{n_3 *}_{i'_2,i'_3} A^{n_3}_{i_2,i_3} \ldots A^{n_{k-1} *}_{i'_{k-2},i'_{k-1}} A^{n_{k-1}}_{i_{k-2},i_{k-1}} \\
&= \sum_{n_4,\ldots,n_{k-1}} \sum_{i_3,\ldots,i_{k-2}} \sum_{i'_3,\ldots,i'_{k-2}} \left(\sum_{n_3,i_2} A^{n_3 *}_{i_2,i'_3} A^{n_3}_{i_2,i_3} \right) A^{n_4 *}_{i'_3,i'_4} A^{n_3}_{i_3,i_4} \ldots A^{n_{k-1} *}_{i'_{k-2},i'_{k-1}} A^{n_{k-1}}_{i_{k-2},i_{k-1}} \\
&\qquad\qquad \ldots \\
&= \sum_{n_{k-1}} \sum_{i'_{k-2}} \sum_{i_{k-2}} \left(\sum_{n_{k-2},i_{k-3}} A^{n_{k-2} *}_{i_{k-3},i'_{k-2}} A^{n_{k-2}}_{i_{k-3},i_{k-2}} \right) A^{n_{k-1} *}_{i'_{k-2},i'_{k-1}} A^{n_{k-1}}_{i_{k-2},i_{k-1}} \\
&= \sum_{n_{k-1}} \sum_{i_{k-2}} A^{n_{k-1} *}_{i_{k-2},i'_{k-1}} A^{n_{k-1}}_{i_{k-2},i_{k-1}} \\
&= \delta_{i'_{k-1},i_{k-1}}
\end{aligned}
\tag{2.73}
$$

The proof for $R = I$ is similar except the process begins with contracting $M^{n_L} M^{n_L \dagger}$ to the identity starting from the right of the tensor network instead of the left and utilizing the right-normalization condition instead of the left-normalization condition. The M tensors in R are replaced with B matrices.

$$
\begin{aligned}
R_{i'_k,i_k} &= \sum_{n_{k+1},\ldots,n_{L-1}} \sum_{i'_{k+1},\ldots,i'_{L-1}} \sum_{i_{k+1},\ldots,i_{L-1}} B^{n_{k+1}*}_{i'_k,i'_{k+1}} \ldots B^{n_{L-1}}_{i_{L-2},i_{L-1}} \left(\sum_{n_L} B^{n_L*}_{i'_{L-1}} B^{n_L}_{i_{L-1}} \right) \\
&= \sum_{n_{k+1},\ldots,n_{L-2}} \sum_{i'_{k+1},\ldots,i'_{L-2}} \sum_{i_{k+1},\ldots,i_{L-2}} B^{n_{k+1}*}_{i'_k,i'_{k+1}} \ldots B^{n_{L-2}}_{i_{L-3},i_{L-2}} \left(\sum_{n_{L-1},i_{L-1}} B^{n_{L-1}*}_{i'_{L-2},i_{L-1}} B^{n_{L-1}}_{i_{L-2},i_{L-1}} \right) \\
&= \sum_{n_{k+1},\ldots,n_{L-3}} \sum_{i'_{k+1},\ldots,i'_{L-3}} \sum_{i_{k+1},\ldots,i_{L-3}} B^{n_{k+1}*}_{i'_k,i'_{k+1}} \ldots B^{n_{L-3}}_{i_{L-4},i_{L-3}} \left(\sum_{n_{L-2},i_{L-2}} B^{n_{L-2}*}_{i'_{L-3},i_{L-2}} B^{n_{L-2}}_{i_{L-3},i_{L-2}} \right) \\
&\quad \ldots \\
&= \sum_{n_{k+1}} \sum_{i'_{k+1}} \sum_{i_{k+1}} B^{n_{k+1}*}_{i'_k,i'_{k+1}} B^{n_{k+1}}_{i_k,i_{k+1}} \left(\sum_{n_{k+2},i_{k+2}} B^{n_{k+2}*}_{i'_{k+1},i'_{k+2}} B^{n_{k+2}}_{i_{k+1},i_{k+2}} \right) \\
&= \sum_{n_{k+1},i_{k+1}} B^{n_{k+1}*}_{i'_k,i_{k+1}} B^{n_{k+1}}_{i_k,i_{k+1}} \\
&= \delta_{i'_k,i_k}
\end{aligned} \tag{2.74}
$$

With the contraction of the L and R tensors to identity matrices, the expression for the overlap derivative simply becomes the M tensor for orbital k.

$$
\begin{aligned}
\frac{\partial}{\partial M^{n'_k*}_{i'_{k-1},i'_k}} \langle \Psi | \Psi \rangle &= \sum_{i_{k-1},i_k} \delta_{i'_{k-1},i_{k-1}} M^{n_k}_{i_{k-1},i_k} \delta_{i'_k,i_k} \\
&= M^{n_k}_{i_{k-1},i_k}
\end{aligned} \tag{2.75}
$$

Substituting Eqs. 2.68 and 2.75 into Eq. 2.67, the minimization problem becomes

$$
\sum_{n_k} \sum_{i_{k-1},i_k} \tilde{H}^{n'_k,n_k}_{i'_{k-1},i'_k,i_{k-1},i_k} M^{n_k}_{i_k,i_{k-1}} = E M^{n'_k}_{i'_{k-1},i'_k} \tag{2.76}
$$

By constructing composite indices $\alpha \equiv (n'_k i'_{k-1} i'_k)$ and $\beta \equiv (n_k i_{k-1} i_k)$, the superblock Hamiltonian is reshaped into a matrix (rank-2 tensor) and M tensor is reshaped into a row vector, resulting in Eq. 2.76 turning into the following eigenvalue problem.

$$
\sum_{\beta} \tilde{H}_{\alpha,\beta} M_\beta = E M_\alpha \tag{2.77}
$$

As mentioned before, the ground state can be obtained by solving the eigenvalue problem above (Eq. 2.77) for all tensor elements $\{M^{n_k}_{i_{k-1},i_k} \mid 1 \leq k \leq L\}$. Since Eq. 2.77 pertains to the tensor elements of a single MPS tensor M^{n_k}, obtaining all MPS tensors requires obtaining a solution for all eigenvalue problems simultaneously in a self consistent way since the solution to one eigenvalue problem is used as input for another eigenvalue problem. The DMRG algorithm is a systematic way of solving the large number of eigenvalue problems by solving a specific eigenvalue problem pertaining to a tensor M^{n_k} while keeping the other tensor elements belonging to other sites constant and then moving to the next tensor $M^{n_{k+1}}$ and repeating the process, sweeping back and forth through the chain until the new tensors are equal to the tensors of the previous iteration. The algorithm is as follows.

1. Generate a random MPS and set the bond dimension m to a value small enough for computational feasibility. Apply iterative SVD until the MPS is right-normalized, i.e. consists of all B tensors.

2. Starting from site $k = 1$, construct the superblock Hamiltonian, reshape it and then diagonalize using an iterative method such as Lanczos diagonalization.

3. Using SVD, left-normalize the tensor M^{n_k} that was obtained from the diagonalization. Multiply the S and V matrices to the tensor to the right, which is $M^{n_{k+1}}$

4. Repeat steps 2 and 3 until $k = L - 1$. This process is known as the right sweep.

5. Starting from site $k = L$, construct the superblock Hamiltonian, reshape it and then diagonalize.

6. Using SVD, right-normalize the tensor M^{n_k} that was obtained from the diagonalization. Multiply the S and V matrices to the tensor on the left, which is $M^{n_{k-1}}$.

7. Repeat steps 5 and 6 until $k = 2$. This process is known as the left sweep.

8. Repeat steps 2-7 until convergence is reached.

As mentioned before, the number of configurations in the ground state MPS obtained with this method is $O(2m^2L)$, which is linear in L instead of exponential if one were to solve the many-body Hamiltonian using exact diagonalization. This computational advantage is what allows large low entropy many-body systems to be solved.

In practice, even with this reduction in complexity, the Hilbert space is usually reduced even further by imposing the conservation of quantum numbers. In this discussion so far, the physical indices only contained fermion occupation number n_k, but in principle other quantum numbers can be physical indices, say local z-component of spin σ_k^z. For this discussion, we will restrict ourselves to the conservation of total electron number $N = \sum_k n_k$, but the following method for imposing quantum number conservation works for any quantum number provided the quantum number arises from $U(1)$ symmetry. Conserving quantum numbers that arise from $SU(2)$ symmetry such as S^2 is more complicated since the non-commutativity of the generators representing the $SU(2)$ group has to be taken into account.

Conserving total electron number is done by treating the physical and bond indices as a type of "charge". Incoming and outgoing indices can be defined where the outgoing indices equals the sum of the incoming indices. Tensor elements with indices that satisfy this conservation of charge are the only non-zero elements. In Fig. 2.8, the incoming indices are indicated by an arrow going into a node and outgoing indices are indicated by arrows leaving a node. The dotted arrow lines indicate dummy bonds, labelled m and $m + N$.

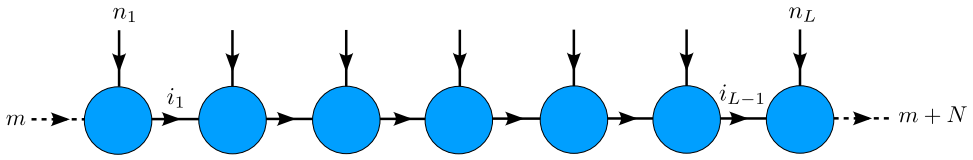

Figure 2.8: MPS with incoming and outgoing indices.

Imposing quantum number conservation is much like conservation of charge in circuit diagrams [36]. Consider a 3-pronged "T" junction where incoming current is

flowing through two prongs and outgoing current is flowing through one, the outgoing current must equal the sum of the incoming currents. Similarly, the outgoing index for a node k in Fig. 2.8 must equal the sum of the incoming indices, i.e. $i_k = n_k + i_{k-1}$. The global condition that must be satisfied for $m + N$ to be conserved, where $m + N$ in this case is total particle number, is $\sum_{k=1}^{L} n_k + \sum_{k=1}^{L-1} i_k = m + N$ where $m + N$ can be set arbitrarily [36].

Thus far, I have shown how the DMRG algorithm can be used to solve the ground state of a many-body system by using SVD to reduce the Hilbert space to $O(2m^2L)$ configurations. To determine electronic and magnetic properties of the system, often it is useful to obtain a few excited states. The DMRG algorithm can also be used to obtain low lying excited states. There are several different methods to do this. One method is to impose a quantum number conservation, such as total S^z, to the trial MPS so that the ground state in this symmetry sector of the Hamiltonian is the first excited state of the system. Another method is to compute the ground state first, and then apply an energy penalty to the ground state so that the DMRG algorithm will minimize the energy to the excited state instead. Also, adding a term such as a Zeeman term can cause the triplet to be the ground state in a system where, for example, the singlet state would be the ground state. In the next section, these three methods for obtaining excited states will be discussed.

2.2.8 Excited States

There are three methods for obtaining excited states using DMRG that will be discussed in this section. The first method that will be discussed is the use of quantum number conservation. If the structure of the low energy spectrum is known, for example, if the ground state is a singlet and the first excited state is a triplet, one can set the total $S^z = 1$ for the trial MPS. The DMRG algorithm will then look for the lowest energy state in this symmetry sector, which in this case will be the triplet. Another method is to add a term to the Hamiltonian that penalizes the ground state energetically. Finally, a term can be added to the Hamiltonian that acts as a sort

of chemical potential. Examples include an actual chemical potential term, or a μS^2 term. One can set μ that would minimize the energy of certain configurations.

To find the excited state using the conservation of a quantum number, consider the example of conserving total S^z. In this example, the physical bond indices n_k of the MPS defined in Eq. 2.24 will no longer just refer to occupation number, but will include a spin degree of freedom. This new definition of n_k for this example is $n_k \in \{|0\rangle, |\uparrow\rangle, |\downarrow\rangle, |\uparrow\downarrow\rangle\}$. To a state of $S^z = 2$, the outgoing index in Fig. 2.8 is set $m + S^z$. Using the same condition that $\sum_k i_k + \sum_k S^z_k = S^z$, then only the tensor elements $M^{n_k}_{i_{k-1},i_k}$ that satisfy this condition will be nonzero. Even if the true ground state of the system is a singlet, the DMRG algorithm will look for the lowest energy state that contains $S^z = 2$. The advantage of this method is that the excited state is treated exactly as if it were a ground state, thus there is no added complexity to this process. However, the states that can be accessed using this method are limited by the quantum numbers that are encoded in the physical indices. For example, in the case of a spin-1 Heisenberg chain with an even number of spins, it would be impossible to find a triplet state with $S^z = 0$ using this method since the lowest energy state with this S^z value would be a singlet.

The next method for obtaining excited states would be to penalize the ground state. First, DMRG is used to obtain the ground state $|GS\rangle$ of the many-body Hamiltonian H. Once the ground state has been found, the Hamiltonian is modified to $H' = H + \omega|GS\rangle\langle GS|$ where ω is the energy penalty for the ground state. If ω is large enough, then the ground state of H becomes the highest energy eigenstate of H', leaving the ground state of H' to be the first excited state of H. This process can be repeated to find higher energy states. The advantage of this method in principle is that one can find states that cannot be found using the previous method. In the example of a Heisenberg spin-1 chain with an even number of spins, if the first excited state happens to be a triplet with $S^z = 0$ and given that if the ground state is a singlet, this method would allow one to find such an excited state. Unfortunately, computing ground states using DMRG are computationally expensive, thus

the amount of resources needed to compute the n^{th} eigenstate scales as $O(n^2)$ [44].

An alternative to the previously mentioned methods is to add a term that acts as a chemical potential or magnetic field. If for example one wants to compute a state with total $S^2 = 0$, a term μS^2 can be added which will penalize any nonzero S^2 state if μ is large and positive. Another example would be to add a Zeeman term $-BS^z$ where $B \geq 0$. Varying B can cause different states of S^z to be the ground state. The advantage of this method is that a state with a specific property can be isolated. However, adding a term like this increases the bond dimension of the MPO which in turn increases the number of tensor elements with a scaling of N_{terms}^2.

These are several approaches to obtain excited states using DMRG. There has been work done on other methods such as imposing $SU(2)$ symmetry which is outside the scope of this work [45]. The methods that were used to compute excited states in this work were the first and third methods, which are imposing $U(1)$ symmetry and adding Zeeman-like terms.

Chapter 3

Systematic Study of the Emission Spectra of Nanowire Quantum Dots

My Contribution

This work was done in collaboration with the National Research Council of Canada. As the lead University of Ottawa-based graduate student under the supervision of Pawel Hawrylak, I designed and simulated the InAsP quantum dot nanowires with both uniform As distributions and gradient distributions. Using the parameterized tight-binding model, I computed the emission spectra of the quantum dots. Furthermore, I wrote the entire theory portion of the paper and constructed Figures 3.1(d) and 3.5. The National Research Council research group fabricated the nanowire quantum dots and performed photoluminescence and correlation measurements.

Authors

Patrick Laferrière, Edith Yeung, Marek Korkusinski, Philip J. Poole, Robin L. Williams, Dan Dalacu, Jacob Manalo, Moritz Cygorek, Abdulmenaf Altintas, Pawel Hawrylak

Abstract

A systematic study of the emission spectra of single InAsP nanowire quantum dots in position-controlled InP photonic nanowire waveguides is presented. Using excitation power-dependent photoluminescence and correlation measurements, we distinguish between the different excitonic complexes responsible for s-shell emission. From measurements of over 40 nominally identical devices, we obtain standard deviations of $\sim 5\,\mathrm{meV}$ in the emission energy of exciton, biexciton and charged exciton photons. Mean biexciton binding energies were 1.9 meV with a standard deviation of $\sim 0.8\,\mathrm{meV}$. The experimental spectra are understood using atomistic multi-million atom theory of neutral and charged multi-exciton complexes implemented in the design tool QNANO.

In semiconductor quantum dots the photon emission spectrum depends on the number of photo-excited carriers [46]. Hence a single photon can be spectrally identified as a recombination from a single exciton. Similarly, entangled photons can be generated by multi-exciton cascades [13, 14, 47, 48]. The difficulty in generating entangled photons by the bi-exciton (XX)-exciton (X) cascade is due to the exciton fine structure [49–53]. This difficulty is overcome by using symmetric quantum dot systems in which fine structure splittings are negligible [54–56]. Alternatively, entangled photon generation can be facilitated using quantum dots where the XX photon emission energy is degenerate with that of the X photon. The biexciton-exciton cascade in such a system is predicted to be less susceptible to deterioration of the degree of entanglement of the emitted photon due to electron-phonon interactions [57]. A vanishing biexciton binding energy can be achieved, for example, by gating [58–60] but may also occur naturally for specific structural parameters [33, 61].

Nanowires have shown promise as efficient sources of non-classical light [62–65]. To investigate the possibility of creating a system having the desired excitonic energy configuration for high fidelity entanglement generation, we study InAsP quantum dots incorporated in bottom-up InP nanowire structures. This system is ideally suited for engineering single and entangled photon sources as their diameter, height and composition is well controlled. In particular, we combine selective-area (SA) epitaxy and vapour-liquid-solid (VLS) epitaxy [66] to grow position-controlled devices consisting of a single quantum dot with a precisely defined geometry optimally located within a photonic nanowire waveguide [67].

Producing high optical quality quantum dots using VLS epitaxy necessitates avoiding some of the typical epitaxial techniques employed when growing heterostructures. For example, (*i*) the crystal structure of VLS nanowires depends on the growth rate [68] and (*ii*) the steady-state alloy composition of the metal catalyst is dependent on the group V element resulting in growth rate transients when switching precursors [69]. These two effects necessitate avoiding growth interrupts (i.e. pumping out the Group III species for a short period of time) in order to grow pure single phase heterostructures (i.e. with no stacking faults that can lead to significant spectral fluctuations [66]). Without the use of growth interrupts, which are typically required to obtain abrupt interfaces separating sections having well-defined compositions [70], ternary InAsP quantum dots are produced containing a significant fraction of phosphorus atoms carried over from the growth of the InP barrier.

The dilute nature of the quantum dot composition produces dots with different optical properties even if they are nominally the same size and have the same total composition; a consequence of strong local fluctuations in confining potentials and strain fields [54]. In order to gain a better understanding of the role of the distribution of the As and P atoms within the quantum dot we have performed a systematic experimental and theoretical study of the emission spectra observed in nominally identical dots. The different excitonic complexes are identified using excitation power-dependent measurements and comparison with results of atomistic

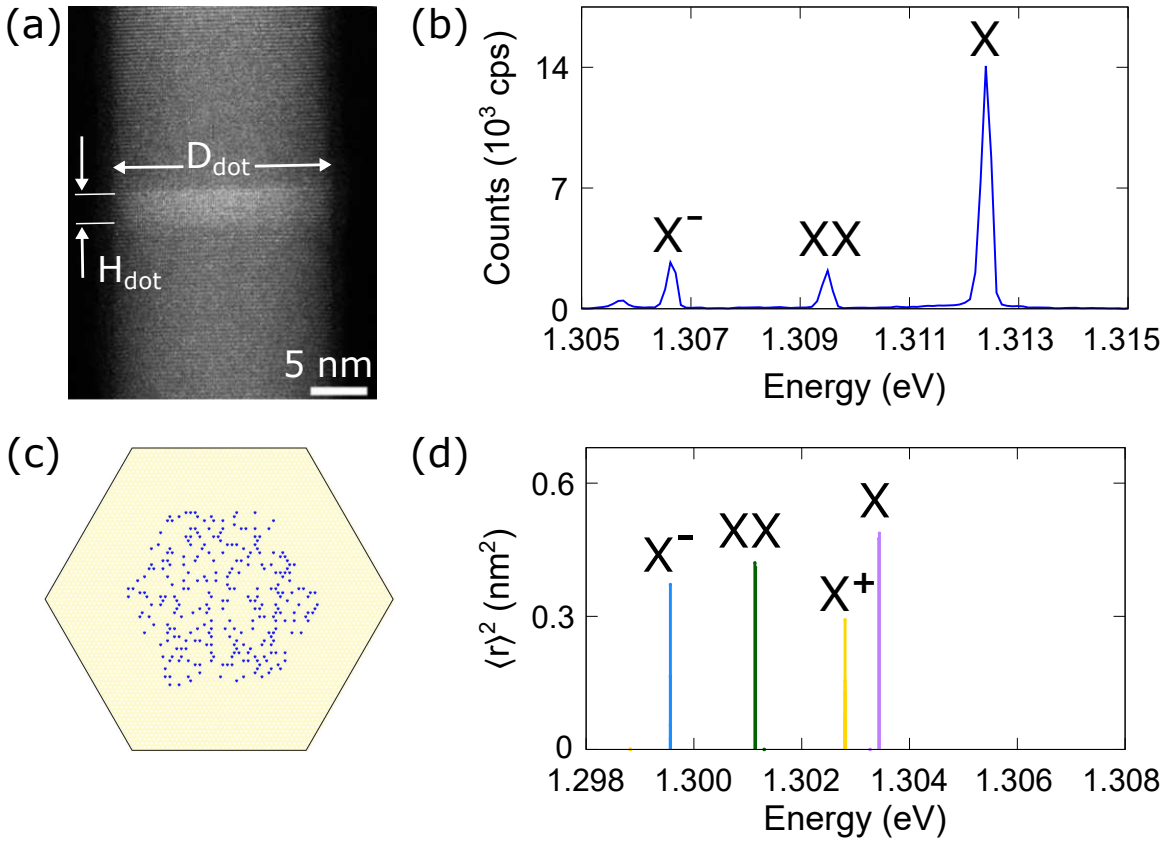

Figure 3.1: (a) Transmission electron microscopy image of an InAsP nanowire quantum dot. (b) Characteristic s-shell emission spectrum of a dot. (c) Cross-section of the InAsP dot used in the calculated emission spectrum shown in (d). with the blue dots indicating the position of As atoms

many-body calculations.

The nanowire quantum dots studied were grown in the InAs/InP material system using chemical beam epitaxy and the SA-VLS growth technique described in Ref. 66. This technique allows for the growth of $InAs_xP_{1-x}$ quantum dots embedded in position-controlled InP photonic nanowires having a wurtzite crystal phase free of stacking faults [64]. The quantum dots are incorporated in an InP nanowire core, $\sim 1\,\mu$m above the base, and have diameters $D_{\rm dot} \sim 20\,$nm, heights $H_{\rm dot} \sim 4\,$nm and compositions $x \sim 20\%$. A cross-sectional transmission electron microscopy image of a dot in a wurtzite InP nanowire core is shown in Figure 3.1(a). The core is clad with an InP shell to produce a photonic nanowire having a geometry optimized for collection of dot emission around $\lambda = 950\,$nm with a base diameter of 250 nm tapered to 20 nm over a length of $\sim 10\,\mu$m.

Optical measurements were carried out at 4 K in a closed-cycle helium cryostat.

Individual nanowires were excited above-band using continuous-wave excitation at $\lambda = 780\,\text{nm}$ (for photoluminescence measurements) or $\lambda = 633\,\text{nm}$ (for correlation measurements) focused to a few microns by a 100X objective with a numerical aperture of 0.81. Photoluminescence from the dot was collected through the same objective and spectrally-resolved using a grating spectrometer with a Si CCD array detector. For autocorrelation measurements, individual lines were selected using a fibre-based tunable filter with a 0.075 nm bandpass and the filtered emission was sent to two fibre-coupled avalanche photodiodes (APDs) via a 50:50 fibre beam-splitter. For cross-correlation measurements, two filters were used, one placed on each output arm of the splitter. The selected lines from each filter were sent to either the 'start' or the 'stop' APD.

Figure 3.1 (b) shows a characteristic emission spectrum of a nanowire quantum dot at low excitation power. At the lowest excitation power, we observe an emission line at high energy identified as the neutral exciton X and one at low energy identified as the charged exciton X^-. The fine structure splitting of the neutral exciton is typically a few μeV [71] and is not resolved in the spectrum. With increasing pump power the biexciton XX appears in between these two lines. The assignment of emission lines is based on the excitation power dependent-photoluminescence and correlation experiments discussed below.

In Figure 3.1 (d) we show the results of atomistic calculations of the emission from multi-exciton complexes in a quantum dot with specifications similar to the dot shown in Figure 3.1 (a): arsenic composition $x = 20\%$, diameter $D_{\text{dot}} = 18.2\,\text{nm}$ and a height $H_{\text{dot}} = 4.1\,\text{nm}$. The calculations are performed for the specific distribution of As atoms in the hexagonal InP nanowire shown in Figure 3.1 (c). The computed transition energies reproduce the ordering of levels observed experimentally, shifted by 9 meV. They also predict similar values for the binding energies of the biexciton (difference in X and XX photon energies, $E_{\text{B}} = E_{\text{X}} - E_{\text{XX}}$) and charged exciton (difference in X and X^- photon energies, $E_{\text{C}} = E_{\text{X}} - E_{\text{X}^-}$). The calculations confirm that the lowest energy peak corresponds to the negatively charged exciton whilst the

emission from the positively charged exciton (not observed experimentally) appears between XX and X. We note the calculated energy splitting of the intermediate exciton state due to fine structure is too small to be observed on this energy scale.

Although we obtained good agreement between theory and experiment for this particular dot, previous measurements on the same quantum dot system have demonstrated a wide range of biexciton binding energies, including both positive and negative values [33]. This variation was attributed, at least in part, to the random distribution of arsenic atoms in the dilute quantum dot [54]. To better quantify the statistical distribution of emission energies in the nanowire quantum dot system, we performed a systematic study of 42 nominally identical nanowire quantum dots having similar emission spectra. The different emission lines were identified using power-dependent photoluminescence and correlation measurements as described below.

In Figure 3.2 we show power-dependent emission spectra from three representative dots in terms of the power at which the X emission peak saturates, P_{sat}. At the lowest excitation power shown, the spectrum from each dot consists of two dominant emission lines around 1.3 eV separated by ~ 6 meV. A third weaker emission line is also evident, spectrally located in between the two dominant peaks, which becomes proportionately brighter as the excitation power is increased. At the highest power shown we observe additional peaks appearing around 1.3 eV as well as a new set of peaks around 1.35 eV. We associate the peaks around 1.3 eV with radiative recombination of electron-hole pairs from the s-shell of the quantum dot whilst those around 1.35 eV with p-shell recombination. As mentioned above, the typical s-shell emission in this quantum dot system for above-band excitation [72] consists of photons from radiative recombination of excitons (X) biexcitons (XX) and negatively charged excitons (X^-). One can readily distinguish between photons originating from excitonic complexes with only one possible decay pathway (e.g. X, X^-) and those with two possible pathways (e.g. XX) from the power dependence of the count rate. In Figure 3.2 (d)-(f) we plot the count rate as a function of pump power for the three dominant peaks for each of the three representative quantum dots. In each case, XX can be distinguished from X and

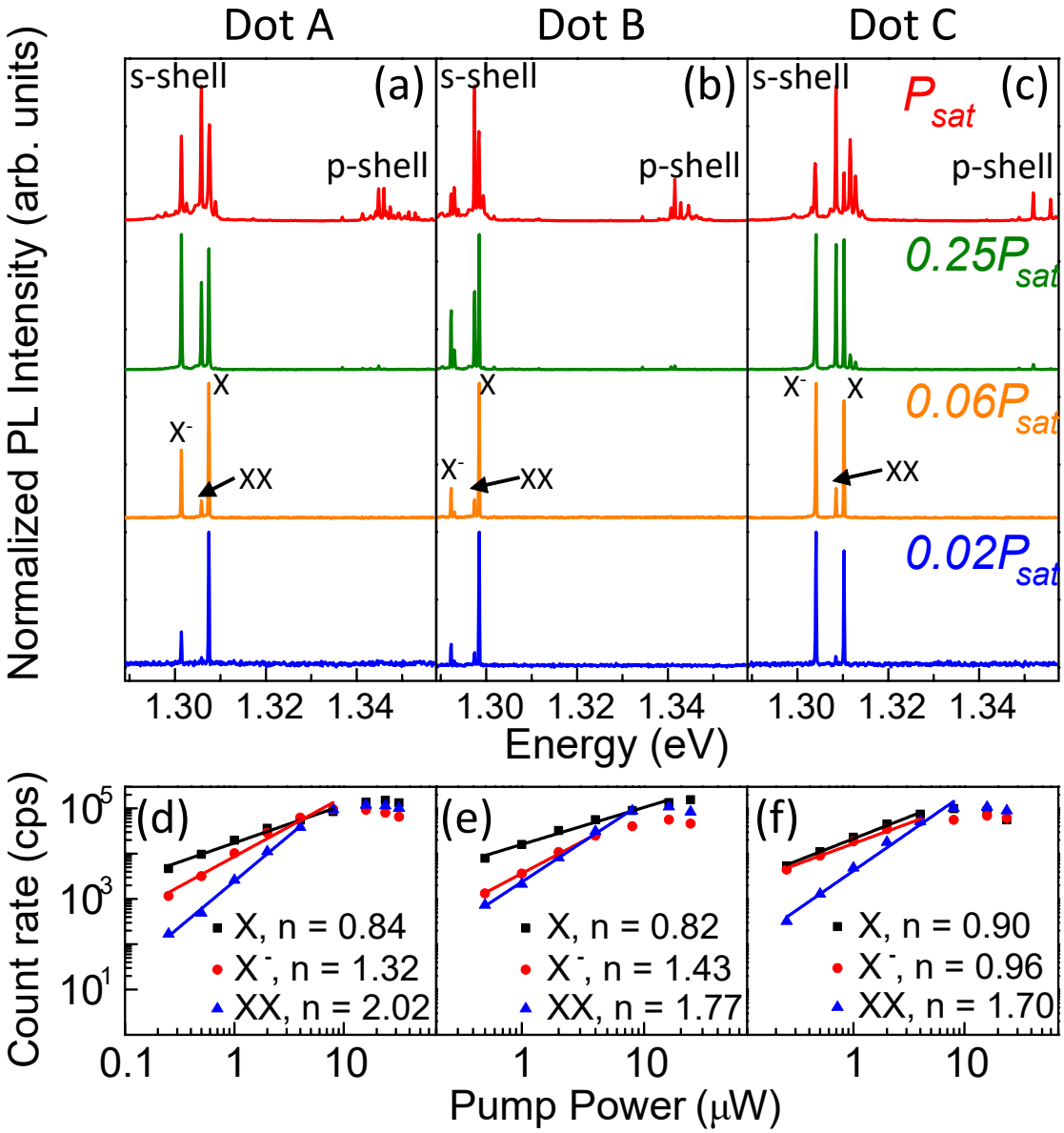

Figure 3.2: (a)-(c) Representative excitation power-dependent photoluminescence (PL) measurements of three nanowire quantum dots. (d)-(f) PL intensity as a function of power for the main three excitonic complexes X, XX and X^-.

X^- by the stronger dependence of the count rate on pump power (exponent $n \sim 2$) as well as the later onset of emission with pump power.

Using the count rate power dependence to distinguish between X and X^- is not completely reliable and may lead to incorrect peak identification. For example, two of the peaks in Dot C in Figure 3.2 show a very similar power dependence. One can instead use the presence of the anisotropic exchange interaction induced fine structure splitting of the neutral exciton X that is absent in the charged exciton X^-. However, the high symmetry of the wurtzite nanowire quantum dot system [54, 55] results in extremely small splittings [65] which are difficult to resolve with a typical grating spectrometer.

Alternatively, correlation measurements can provide additional information on the nature of the excitonic complex from which the photons are produced. In Figure 3.3 we show the second-order autocorrelation measurements, $g^{(2)}(\tau)$, of the three peaks observed in a characteristic dot. Biexciton photons are readily identified from the bunching observed at short time delays when pumping weakly [73], shown in Figure 3.3(a). Right after the detection of a biexciton photon, the dot is populated with one electron-hole pair which may then decay to the ground state or capture a second pair to form a new biexciton. As the excitation power is decreased, reducing the capture rate of electron-hole pairs, it becomes comparatively more likely to form a new biexciton at short delays when the dot already contains one electron-hole pair relative to long delays when the dot will typically be empty and requires the capture of two electron-hole pairs. Hence the decay of the bunching corresponds to the X lifetime.

Distinguishing between X and X^- using autocorrelations measurements is less trivial. In Figures 3.3 (b) and (c) we show the autocorrelation for the high and low energy peaks, respectively, at excitation powers of $\sim P_{sat}/5$ and $\sim P_{sat}/2$. In (b) the curve shows the behaviour expected from a two-level system consisting of the vacuum and the excitonic state, for which $g^{(2)}(\tau) = 1 - \mathrm{e}^{-(R+\Gamma)|\tau|}$ where R is the pump rate and Γ is the excitonic radiative lifetime. In both cases, the spectra display a strong

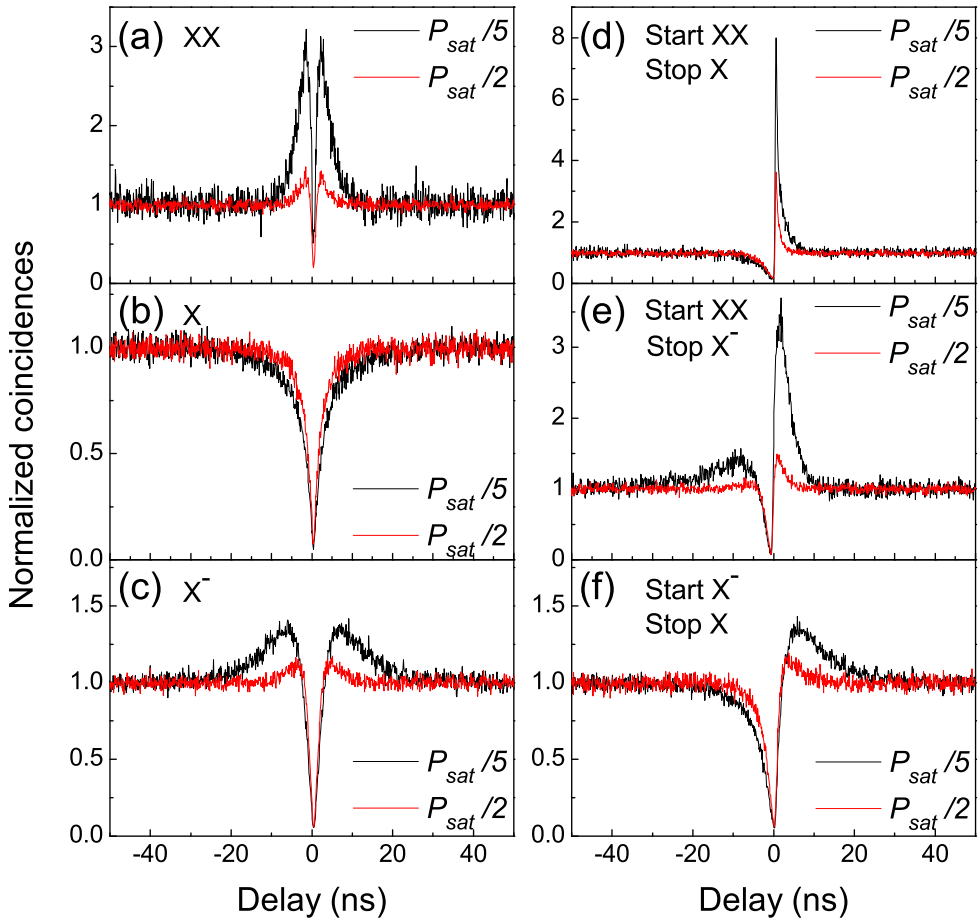

Figure 3.3: Power-dependent second-order autocorrelation measurements of (a) exciton, (b) biexciton and (c) charged exciton photons of a characteristic dot. Power-dependent cross-correlation between (d) XX-X, (e) XX-X^- and (f) X^--X of a characteristic dot.

antibunching dip down to $g^{(2)}(\tau = 0) \sim 0.05$ with a width that reflects the exciton lifetime when $R << \Gamma$ whilst for $R >> \Gamma$, the width is limited by the excitation rate. In the case shown in Figure 3.3(c), we also observe bunching at short delays that decays to average coincidence counts over an excitation power-dependent time scale that is longer than that expected from radiative recombination. The degree of bunching and the associated time scales vary from dot to dot and we associate this behaviour with changes in the charge configuration of the dot (e.g. blinking) that has been previously observed in different quantum dot systems [74–76].

To distinguish between X and X^- we measured the cross-correlations [73, 75–78] between the three dominant peaks. In Figure 3.3(d) we show the cross-correlation between the central peak (XX) and the high energy peak measured for excitation powers of $P_{sat}/2$ and $P_{sat}/5$. We send XX to the start APD and the high energy emission peak to the stop APD. The observed asymmetric bunching behaviour indicates a cascaded emission process typical of a $XX - X$ cascade (i.e. XX photons are emitted first followed by X photons). We thus identify the high energy peak for this dot as originating from X recombination.

Figure 3.3(e) shows the cross-correlation between the low energy peak, identified as X^-, and XX for a characteristic dot. The correlation spectra show strong antibunching at $\tau = 0$ and bunching at both positive and negative delays with a higher degree of bunching at positive delays and at lower excitation. In the limit of low excitation, the average number of carriers in the dot tends to zero. At short positive delays, having just detected an XX photon, the dot is necessarily occupied with two carriers (one electron and one hole). To put the dot in the X^- state then requires the capture of just a single electron. The probability of capturing a single carrier is more likely than capturing three carriers (two electrons and a hole) which is required at longer delays when the dot is typically empty (for low excitation rates). This produces the observed bunching at short positive delays. Similarly, at short negative delays, having just detected an X^- photon, the dot is left occupied with a single electron. To put the dot in the XX state requires capturing three additional carriers (one electron and two holes) which is more likely than the four carrier required (two electrons and two holes) if the dot were empty. This produces the observed bunching at short negative delays.

Finally we look at the cross-correlation between X^- and X (Figure 3.3(f)) which shows an antibunching dip at $\tau = 0$ and short delay bunching, but only for $\tau > 0$. As above, at short positive delays, having just detected an X^- photon, the dot is left occupied with a single electron. To create the neutral exciton, a single hole is required which is more likely than the requirement of capturing of two carriers (one

Table 3.1: Emission energies and spacings and their standard deviations from fits to the data in Figure 3.4.

	Emission Energy (meV)	σ **(meV)**	**Energy Spacing (meV)**	σ **(meV)**
X	1301	5.0	—	—
X^-	1296	5.6	5.92	0.32
XX	1300	4.3	1.90	0.77

electron and one hole) into an empty dot and thus bunching is observed at positive delays. No bunching is observed at negative delays as the dot is empty, having just detecting an X photon.

The results of applying the above optical characterization methodology to 42 quantum dots to extract emission energies E_{X}, E_{XX} and $E_{\mathrm{X^-}}$ as well as energy spacings E_{B} and E_{C} are summarized in Figure 3.4 and Table 3.1. In the table we have included the standard deviations from gaussian fits to the histograms in Figure 3.4.

In order to gain a microscopic understanding and evaluate the ability to engineer the emission spectra of nanowire quantum dots we use the atomistic million-atom many-body theory of multi-exciton complexes implemented in the code QNANO [54, 79, 80]. The simulations are targeted to provide insight into the observed distribution of biexcitonic binding energies, with the specific aim of identifying the structural parameter required to achieve coincidences between X and XX emission lines.

The starting point of QNANO are the atomic positions of In and P in a hexagonal nanowire. Next, we replace 20% of the P atoms with As in the volume of a hexagonal quantum dot as shown in Figure 3.1(c). Because InAs and InP lattice constants differ, such a replacement causes strain and displacement of the As atoms from the P positions. In the case of the InAsP quantum dot, this mismatch is about 3% and is accounted for in the model [54]. We hence find the actual atomic positions of all the atoms by minimizing the total elastic energy.

With the atomic positions of all the atoms defined, we obtain the single particle

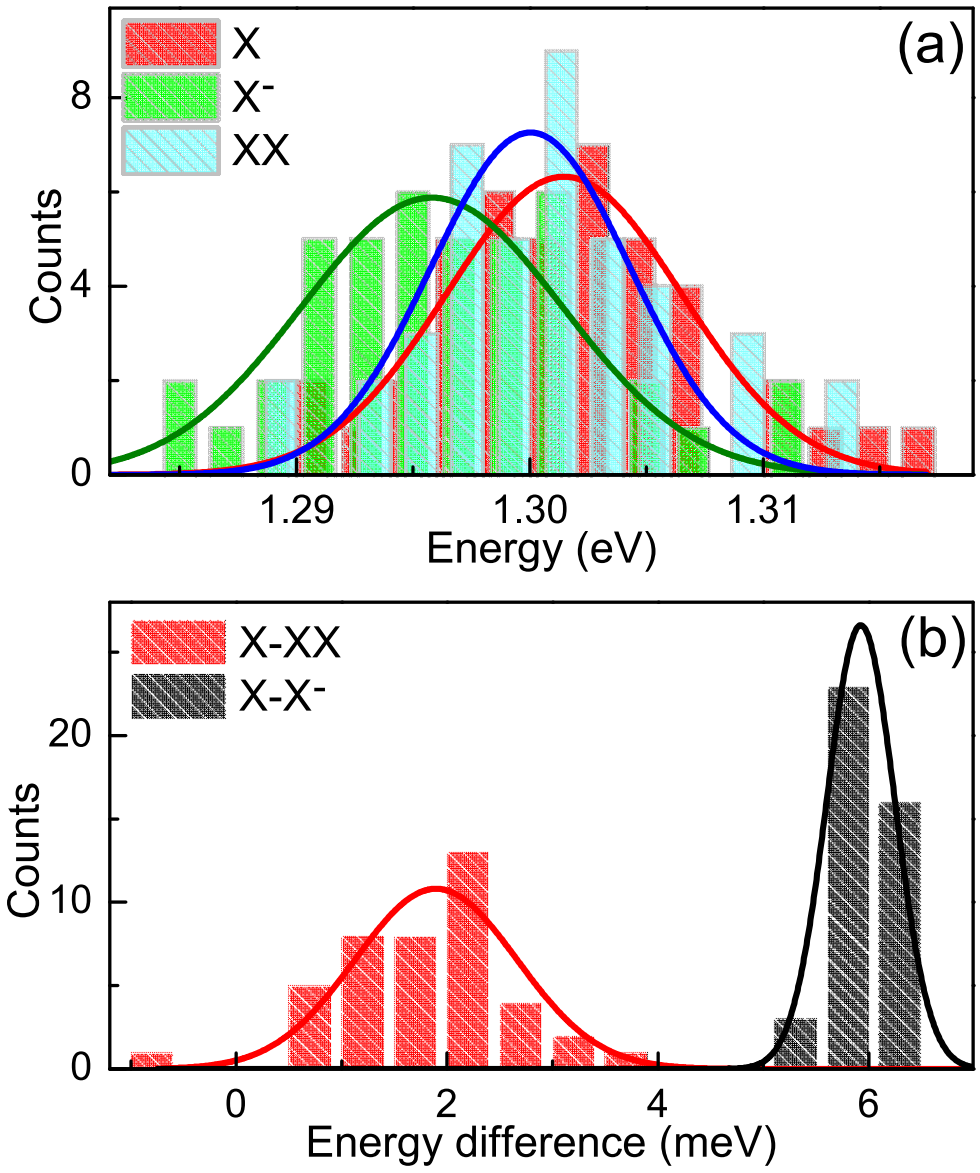

Figure 3.4: (a) Energy distribution of the different complexes extracted from the measurements on 42 nanowire quantum dots. (b) Histograms of the energy difference between the X-XX emission lines, E_B (red) and the X-X^- emission lines, E_C (black).

states from the strain parameterized tight-binding Hamiltonian:

$$H_{TB} = \sum_{i=1}^{N_a} \sum_{\alpha=1}^{N_{\text{orb}}} \varepsilon_{i\alpha} c_{i\alpha}^{\dagger} c_{i\alpha} + \sum_{i=1}^{N_a} \sum_{\alpha,\beta=1}^{N_{\text{orb}}} \lambda_{i\alpha\beta} c_{i\alpha}^{\dagger} c_{i\beta} + \sum_{i=1}^{N_a} \sum_{j=1}^{nn(i)} \sum_{\alpha,\beta=1}^{N_{\text{orb}}} t_{i\alpha j\beta} c_{i\alpha}^{\dagger} c_{j\beta} \tag{3.1}$$

where the Roman indices denote atomic positions and the Greek indices denote atomic orbitals. The parameters ε, t and λ representing the on-site energy, tunneling matrix elements and spin-orbit coupling, respectively, are obtained by fitting (3.1) to a density functional theory (DFT) bandstructure of the (strained) bulk materials, discussed in detail in Ref. [54]. In this model, each atom is described by 20 $spds^*$ orbitals. Using exact diagonalization, the conduction and valence band quantum dot states for structures with up to millions of atoms are obtained.

In the next step we describe excited electrons and valence holes strongly interacting with each other. The multi-exciton complexes are described by the many-body Hamiltonian:

$$H_{MB} = \sum_{i} E_i^{\text{CB}} c_i^{\dagger} c_i + \frac{1}{2} \sum_{ijkl} \langle ij|V|kl\rangle c_i^{\dagger} c_j^{\dagger} c_k c_l + \sum_{p} E_p^{\text{VB}} h_p^{\dagger} h_p + \frac{1}{2} \sum_{pqrs} \langle pq|V|rs\rangle h_p^{\dagger} h_q^{\dagger} h_r h_s + \sum_{iqrl} \left(\langle iq|V|rl\rangle - \langle iq|V|lr\rangle \right) c_i^{\dagger} h_q^{\dagger} h_r c_l \tag{3.2}$$

where $E_i^{\text{C (V) B}}$ and $c_i(h_i)$ are the conduction (valence) band energies and electron (hole) annihilation operators respectively. We then construct electron-hole configurations for a given excitonic complex, construct the Hamiltonian matrix in the space of electron-hole configurations and diagonalize it to obtain the multi-excitonic energy levels and wavefunctions. Simultaneously, we compute dipole matrix elements and emission spectra.

One of the difficulties in calculating the many-body states lies in the Coulomb

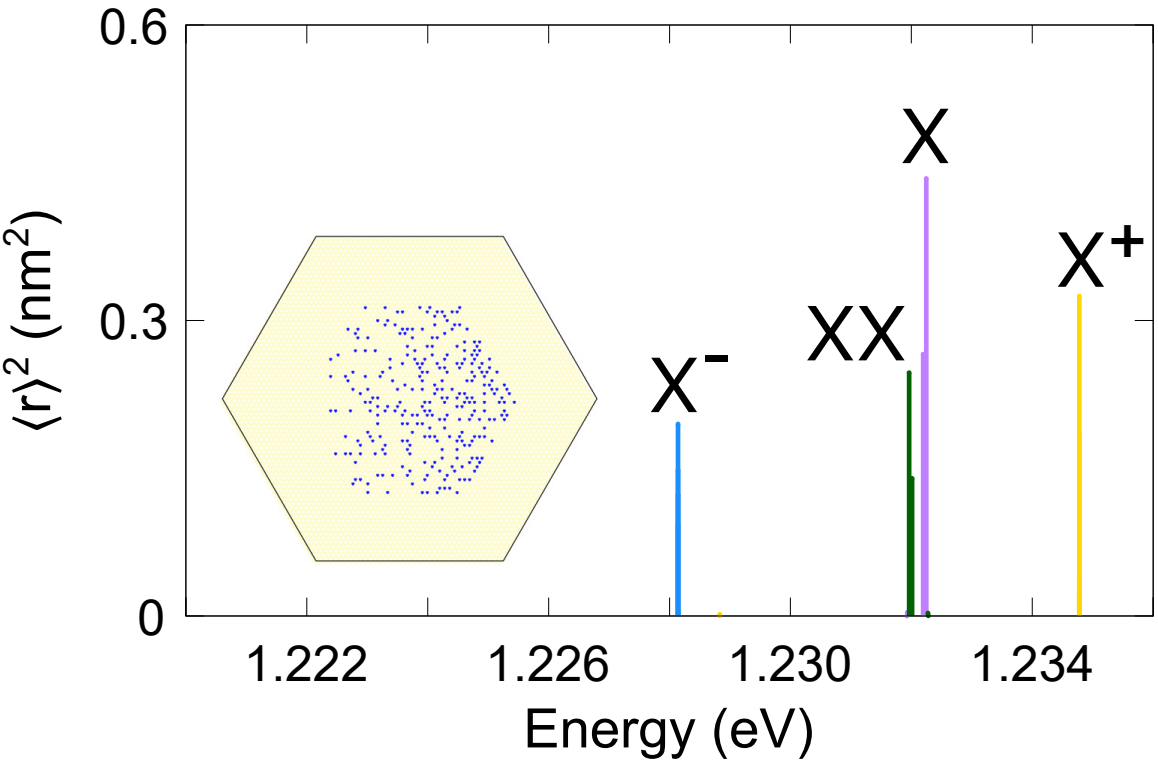

Figure 3.5: Emission spectrum of the quantum dot with a gradient distribution of As atoms. The inset is a cross-section of the quantum dot used in the simulation, the blue dots corresponding to the position of As atoms.

matrix elements. Since the nanostructure we are dealing with contains hundreds of thousands of atoms, each with 20 orbitals, necessary approximations are made in order to maintain computational feasibility. These approximations include only computing two-centre integrals i.e. integrals that only involve the scattering of electrons on one or two atoms, distinguishing between on-site and long-range terms, simplifying the latter by neglecting the overlap of wave functions on distant atoms.

Calculated emission spectra are shown in Figures 3.1 and 3.5. Figure 3.1(c) shows a cross-section of the simulated InAsP quantum dot having parameters similar to the grown structures: arsenic composition $x = 20\%$, diameter $D_{\text{dot}} = 18.2\,\text{nm}$ and a height $H_{\text{dot}} = 4.1\,\text{nm}$. Since the distribution of As atoms is random, the calculated emission spectrum differs from experimental spectra (e.g. Figure 3.1(b)) but emission lines do follow the same order as seen from Figure 3.1(d), with X^- being the lowest energy line, followed by XX, X^+ and X lines.

We note that the distribution of XX binding energies shown in Figure 3.4 includes

samples where the XX and X emission lines coincide. If we repeat our simulations using randomly generated As atom distributions, we observe a distribution of XX binding energies with a mean value of 2.4 meV [54], which overestimates the experimental value of 1.9 meV. We also obtain a standard deviation of only 0.72 meV, suggesting an additional contribution is required in order to reproduce the experimentally observed negative XX binding energies.

The systematically higher theoretical value of the biexciton binding energy compared to the measurements can be explained by the assumption of a homogeneous distribution of the As atoms within the dot. We have previously demonstrated [58] that a lateral displacement between the centres of electron and hole wave functions results in a decreasing biexciton binding energy. While this was achieved in Ref. [58] using a lateral electric field, in the case of InAsP nanowire quantum dots, an inhomogeneous distribution of As atom can play a similar role. Because of the larger deformation potential constant as well as the larger effective mass of holes compared to electrons, the hole wave function tends to be strongly localised in regions with high As content, while electron wave functions have a more delocalised character spanning the dot volume more smoothly [54]. As an example, Figure 3.5 depicts the situation of inhomogeneous As distribution implemented as a linear lateral gradient. We find a significant reduction of the biexciton binding energy to a value of $\sim 200\,\mu$eV, corroborating the trend towards a reduction of biexciton binding energies with introducing inhomogeneities in the As distribution.

While both, electron and hole wave functions depicted in Figure 3.5 are shifted towards the right-hand side of the quantum dot, where the As density is large, the effect is stronger for the hole wave function. The net effect is a difference of the centres of the respective wave function. A similar effect can be expected from clustering of As atoms that can occur naturally during the growth, driven by a local lattice distortion of already incorporated As atoms, which may provide an energetic advantage for the incorporation of further As atoms nearby. Thus, while the overall theoretical description leads to good estimates of quantities like the biexciton binding energies,

more detailed investigations of the As incorporation dynamics and the resulting As distributions would be beneficial for modelling the many-body properties in InAsP nanowire quantum dots.

Excitation power-dependent photoluminescence and autocorrelation measurements were used to identify the different excitonic complexes in nanowire quantum dots. The emission spectra were compared with predictions of the atomistic multi-million atom design tool QNANO. The observed variation of emission energies are associated with different distributions of arsenic atoms in the dilute quantum dot system which has an otherwise well-defined geometry. Our findings summarise the characterization and atomistic theory of quantum dots in nanowires and are a step toward the full understanding of the dot dynamics within nanowire waveguides.

This work was supported by the Natural Sciences and Engineering Research Council of Canada and the Canadian Space Agency. J.M., A.A., M.C., P.L., E.Y. and P.H. acknowledge funding by NSERC Discovery, QSC2 SPG, QC2DM SPG and UOttawa URC grants. M.C. acknowledges funding from Humboldt Foundation and UOttawa.

Chapter 4

Electronic and magnetic properties of many-electron complexes in charged InAsP quantum dots in InP nanowires

My Contribution

As the lead author of this paper, I simulated the single and double nanowire quantum dots using the parameterized tight-binding model. This involved computing the single particle and manybody spectra of both systems. Furthermore, I derived an effective multi-orbital Hubbard model. Using a genetic algorithm, I obtained multi-orbital Hubbard model parameters from the tight-binding spectra. For the publication itself, I wrote the manuscript as well as created all of the figures.

Authors

Jacob Manalo, Moritz Cygorek, Abdulmenaf Altintas, Pawel Hawrylak

Abstract

We present here a microscopic theory of electronic complexes in charged $InAs_xP_{1-x}$ quantum dots in InP nanowires with a hexagonal cross section and determine the potential use of an array of such quantum dots as a synthetic spin chain for the possible construction of a topological qubit. The single particle energies and wavefunctions are obtained by diagonalizing a microscopic atomistic tight-binding Hamiltonian of multiple quantum dots in the basis of $sp^3d^5s^*$ local atomic orbitals for a given random distribution of arsenic (As) vs phosphorus (P) atoms. The conduction band electronic states are found grouped into s, p and d quantum dot shells. For a double dot, the electronic shells can be understood in terms of interdot tunneling despite the random distribution of As atoms in each quantum dot. The single and double dot structures were charged with finite number of electrons. The many-body Hamiltonian including Coulomb electron-electron interactions was constructed using single atomistic particle states and then diagonalized in the space of many-electron configurations. For a single dot filled with N_e = 1-7 electrons, ground state of half filled p-shell configuration with $N_e = 4$ was found with total electronic spin $S = 1$. The low energy spectrum obtained using exact diagonalization of a Hamiltonian of a charged double dot filled with $N_e = 8$ electrons, i.e. half-filled p-shells in each dot, was successfully fitted to the Hubbard-Kanamori and antiferromagnetic Heisenberg spin one Hamiltonians. The atomistic simulation confirmed the potential of InAsP/InP quantum dots in a nanowire for the design of synthetic spin chains.

4.1 Introduction

There is currently interest in designing quantum systems for quantum technologies, including quantum computation and quantum communication. This includes semiconductor quantum dots containing single and multi-electron complexes, with quantum information embedded in electron spin or encoded in multi-electron configurations [2, 10, 15, 16, 81–91]. The single and double quantum dots have also been

explored for the generation of single and entangled photon states [12–14], photon cluster states [48], lasers [92–94] and quantum dot photodetectors [95, 96, 96].

Here we focus on designing synthetic spin one chains using many-electron complexes in arrays of quantum dots embedded in semiconductor nanowires [15, 97, 98]. Many electron complexes in self-assembled [98–102] and etched quantum dots [103, 104] have already been extensively investigated. Here we discuss InAsP quantum dots in InP nanowires [4, 12, 71, 97, 98]. The electronic properties of these quantum dots can be designed by controlling the position, size, height, and arsenic concentration. The dots have a hexagonal disk geometry and are grown without a wetting layer using vapour-liquid-solid epitaxy, with a relatively low concentration of arsenic atoms replacing the phosphorus atoms [3]. As is the case with self-assembled dots, these dots suffer from intrinsic atomistic disorder. Despite the disorder, the conduction band states form electronic shells [4] that strongly resemble harmonic oscillator states observed in self-assembled quantum dots [46, 105, 106]. The effect of disorder results in the effective quantum dot lateral anisotropy and plays a role in the removal of degeneracies of electronic shells. When engineering the total spin of the many electron complexes, the degeneracies play an important role which leads to maximal spin at half-filled shells. Here we show that the spin-1 ground state survives atomistic disorder and that the different realizations of disorder on two vertically coupled quantum dots can be still understood in terms of interdot tunneling and the formation of bonding and antibonding electronic states. The many-electron complexes corresponding to half-filled p-shells can be understood in terms of Hubbard-Kanamori and anti-ferromagnetic Heisenberg Hamiltonians for coupled spin-1 particles.

The problem of many-electron complexes in vertically coupled quantum dots has already been investigated using the effective mass model where atomic disorder was neglected and the Coulomb interactions were derived microscopically [15, 103, 107–109]. The atomistic description of an InAsP quantum dot in InP nanowire and the many-exciton complexes were previously analyzed by Zielinski [50] and by some of us [4, 27, 110, 111].

Here, we use a realistic tight-binding model consisting of millions of atoms with twenty ($spds^*$) orbitals each to compute the single particle states, with strain, and the configuration interaction method to compute the many-body states of $N_e = 1 - 8$ electrons in single and double, vertically coupled $InAs_xP_{1-x}$ quantum dots in an InP nanowire in the wurtzite phase.

We demonstrate that a single quantum dot containing $N_e = 4$ electrons in a half-filled p-shell configuration corresponds to a spin-1 ground state. Consequently, a chain of two vertically coupled quantum dots, each with a half-filled p-shell, was found to have a low energy electronic spectrum that resembles two antiferromagnetically coupled spin-1 particles. The atomistic disorder in the dots leads to a variation of tunneling matrix elements and spin-spin exchange coupling constants. The microscopic theory was later used to obtain parameters of a simplified Hubbard-Kanamori and Heisenberg Hamiltonians. The Hubbard-Kanamori parameters obtained from atomistic calculations enable the description of larger chains and thus the investigation of a synthetic spin-1 Haldane material.

The paper is organised as follows. First, we briefly discuss the tight-binding and configuration interaction methods that are used to simulate the electronic properties of the quantum dots. We then describe the electronic properties of electronic complexes in a single InAs quantum dot in an InP nanowire, where we discuss the single particle and many-body electronic states, and determine the spin of the ground state of the half-filled p-shell to be $S = 1$. Next, we provide an analysis of the electronic properties of electrons in two vertically coupled quantum dots. Similar to the analysis of a single quantum dot, here we determine whether two quantum dots with half-filled p-shells behave as two coupled spin-1 particles. This is followed by a description of the effective Hubbard-Kanamori model. Here, we compare the results of the Hubbard-Kanamori model with the Heisenberg chain and the atomistic tight-binding plus configuration interaction microscopic models. Finally, we discuss the results of both the Hubbard-Kanamori and microscopic models in the context of a synthetic Heisenberg chain.

4.2 Microscopic theory of charged $InAs_xP_{1-x}$ quantum dots in InP nanowires

The Microscopic theory of charged InAsP quantum dots in InP nanowires begins with a definition of atomistic structure followed by the computation of strain, construction of an atomistic tight-binding Hamiltonian from ab-initio methods, and obtaining the single particle states and energy spectrum. This is followed by the computation of Coulomb matrix elements constructed with the tight-binding atomistic single particle states. We next introduce N_e additional electrons, construct many-body configurations and their interaction Hamiltonian to obtain a many-body spectrum by exact diagonalization [4,27,110]. Analysis of the spectrum and electron configurations then leads to our understanding of the electronic and magnetic properties of these nanostructures.

The single particle states of a single and double $InAs_xP_{1-x}$ quantum dots embedded in an InP nanowire are expanded in terms of local atomic orbitals as

$$\langle \mathbf{r}|i\rangle = \sum_k \sum_\alpha C_{ik\alpha}\phi_\alpha(\mathbf{r}-\mathbf{R}_k) \tag{4.1}$$

where $\phi_\alpha(\mathbf{r}-\mathbf{R}_k)$, the orbital α of atom k at location $\mathbf{R}_k$, is assumed to have the form

$$\phi_\alpha(\mathbf{r}) = Ar^a e^{-br} Y_l^m(\theta,\varphi)\chi_\sigma. \tag{4.2}$$

Each atomic orbital has a radial component which is approximated as a Slater orbital with material dependent parameters a and b, a Spherical Harmonic Y angular component, spinor component χ_σ and normalization constant A.

Next the tight-binding Hamiltonian in the basis of $N_{\text{orb}} = 20$ $sp^3d^5s^*$ local atomic

orbitals is constructed as

$$H_{TB} = \sum_{i=1}^{N_a}\sum_{\alpha=1}^{N_{\rm orb}} \varepsilon_{i\alpha} c_{i\alpha}^{\dagger} c_{i\alpha} + \sum_{i=1}^{N_a}\sum_{\alpha,\beta=1}^{N_{\rm orb}} \lambda_{i\alpha\beta} c_{i\alpha}^{\dagger} c_{i\beta} + \sum_{i=1}^{N_a}\sum_{j=1}^{nn(i)}\sum_{\alpha,\beta=1}^{N_{\rm orb}} t_{i\alpha j\beta} c_{i\alpha}^{\dagger} c_{j\beta} \quad . \tag{4.3}$$

Here $\varepsilon_{i\alpha}$ is the onsite energy, the spin-orbit interaction is $\lambda_{i\alpha\beta}$ and the tunneling matrix element is $t_{i\alpha j\beta}$, whereby the Roman indices denote atom and Greek indices denote atomic orbital. The values of these tight-binding parameters for the InAsP qauntum dot nanowires are taken directly from Ref. [4]. Determination of these parameters involves fitting (4.3) to an ab-initio DFT based band structure as discussed in detail in Refs. [4, 27, 111]. We next introduce N_e electrons into our quantum dot.

The behaviour of multi-electron complexes is described by the many-body Hamiltonian

$$H_{MB} = \sum_i E_i c_i^{\dagger} c_i + \frac{1}{2}\sum_{ijkl} \langle ij|V|kl\rangle c_i^{\dagger} c_j^{\dagger} c_k c_l \tag{4.4}$$

where the indices i refer to single particle states and $\langle ij|V|kl\rangle$ are the Coulomb matrix elements.

Since the nanostructures under investigation contain several millions of atoms, necessary approximations to the Coulomb matrix elements are made in order to maintain computational feasibility. First, only two centre integrals are computed, i.e. integrals that only involve scattering of electrons on one or two atoms and second, only on-site and long-range terms are included, where $\langle ij|V|kl\rangle = \langle ij|V^{\rm OS}|kl\rangle + \langle ij|V^{\rm LR}|kl\rangle$. The on-site terms, given by

$$\langle ij|V^{\rm OS}|kl\rangle = \frac{e^2}{4\pi\epsilon_0\epsilon_{\rm OS}} \sum_{a\in N_{\rm a}} \sum_{\alpha,\beta,\gamma,\delta} C_{ia\alpha}^{*} C_{ja\beta}^{*} C_{ka\gamma} C_{la\delta} \times \int \frac{\phi_\alpha^{*}(\mathbf{r}_1)\phi_\beta^{*}(\mathbf{r}_2)\phi_\gamma(\mathbf{r}_2)\phi_\delta(\mathbf{r}_1)}{|\mathbf{r}_1 - \mathbf{r}_2|} d^3r_1 d^3r_2, \tag{4.5}$$

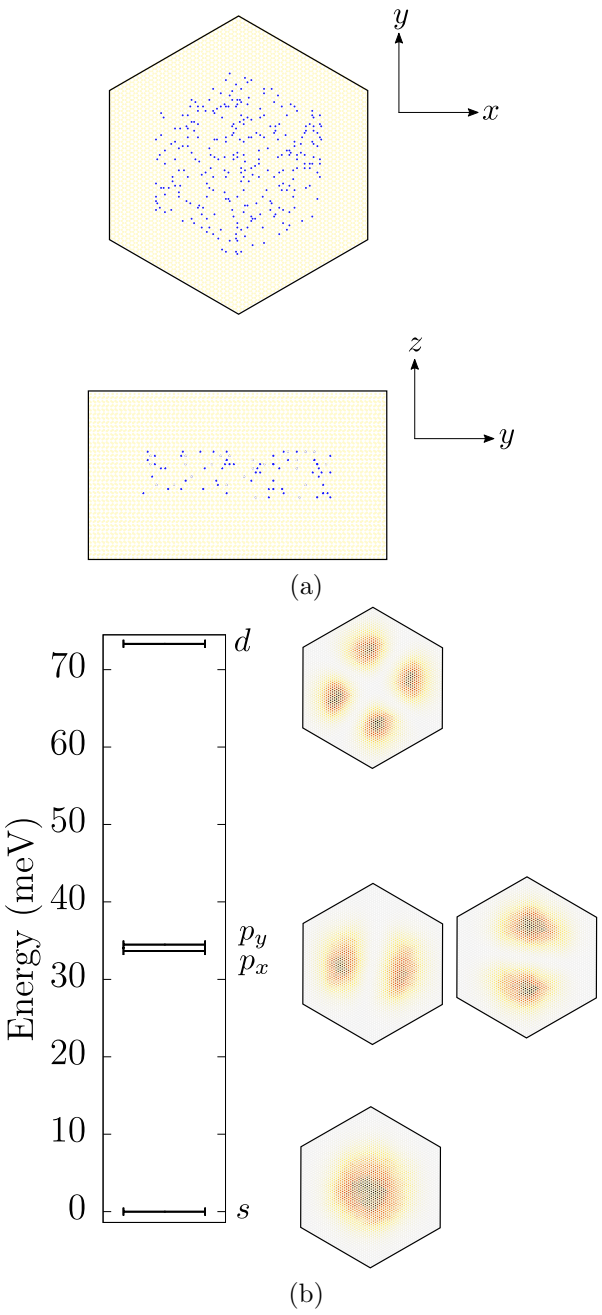

Figure 4.1: (a) Top and side cross section of the quantum dot nanowire containing about 380000 atoms. The diameter of the quantum dot is 18.2 nm and the thickness is 4.1 nm. The diameter of the nanowire is 28.2 nm and the height is 13.5 nm. (b) Single particle spectrum (left) and charge densities (right). The p_y charge density is located slightly higher than the p_x charge density to illustrate that the energy of the p_y state is slightly higher than the p_x energy.

only contain integrals corresponding to scattering of orbitals on a single atom a. Due to the dependence of the dielectric constant on distance [112, 113], the on-site dielectric constant $\epsilon_{\rm OS}$ is taken to be 1.

The other significant contributions to the total Coulomb matrix element are the long-range terms, given by

$$\begin{aligned}\langle ij|V^{\rm LR}|kl\rangle =& \frac{e^2}{4\pi\epsilon_0\epsilon_{\rm LR}}\sum_a\sum_{b\neq a}\sum_{\alpha\beta} C^*_{ia\alpha}C^*_{jb\beta}C_{kb\beta}C_{la\alpha} \\ &\times \frac{1}{|\mathbf{R}_a-\mathbf{R}_b|}\end{aligned} \tag{4.6}$$

where the electron-electron Coulomb interactions are screened by bulk dielectric constant $\epsilon_{\rm LR}$. Since the electrons located at atoms a and b are far apart, they can be treated as point charges which eliminates the need to compute the integrals explicitly. Furthermore, the only terms that survive the orthogonality relation between local atomic orbitals are terms where the atomic orbital angular momentum is conserved.

With the Coulomb matrix elements in place, the many-body states $|\nu\rangle$ of N_e electrons can be expanded in electronic configurations k as $|\nu\rangle = \sum_k A^\nu_k|k\rangle$. The many-body configurations, $|k\rangle = \prod_i c_i^\dagger|0\rangle$, are written as Slater determinants constructed from the finite number of single particle orbitals i. Next, the matrix elements $\langle q|H|k\rangle$ of the many-body Hamiltonian are constructed in the space of configurations. The ground and excited states of the electronic complex are computed by diagonalization of the many-body Hamiltonian (4.4).

4.3 Electronic states of a single $InAs_xP_{1-x}$ quantum dot in InP nanowire

4.3.1 Single particle levels of a single $InAs_xP_{1-x}$ quantum dot in InP nanowire

Here we discuss the single particle spectrum of a single quantum dot in a nanowire. We start with InP nanowire and define a quantum dot volume. Within this volume we randomly replace P atoms with As atoms on the InP lattice, resulting in average concentration of As of 10%. The resulting strain is obtained by moving As atoms to minimize the total elastic energy. With the equilibrium position of atoms obtained, we construct a tight-binding Hamiltonian. Diagonalization of the tight-binding Hamiltonian (4.3) gives the single particle spectrum of an $InAs_{0.1}P_{0.9}InP$ quantum dot in an InP nanowire. Fig. 4.1(a) shows the random distribution of the As atoms in the quantum dot. Despite this random distribution, the single particle states, shown in Fig. 4.1(b), are grouped into s, p and d quantum dot electronic shells, which are not to be confused with the individual atomic orbitals as the quantum dot shells are localized throughout the whole quantum dot. However, due to the lateral asymmetry of the dot caused by random distribution of As atoms, the two states of the p shell, denoted as p_x and p_y, are not degenerate, but are split by an energy difference of $\Delta \approx 0.84$ meV. The splitting of the p shell is much smaller than the energy separation of different electronic shells, e.g. s-p and p-d shells with splitting of the order of 30 meV. Hence the p-shell is approximately two-fold degenerate as is the case with previously investigated effective mass models [16].

4.3.2 Many-electron complexes in a single $InAs_xP_{1-x}$ quantum dot in InP nanowire

We now turn to many-electron complexes in an $InAs_xP_{1-x}$ quantum dot in an InP nanowire. The many-body spectrum of an electronic complex is obtained through

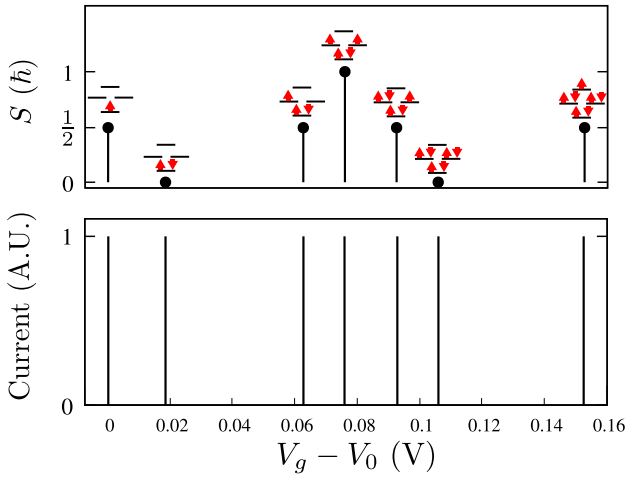

Figure 4.2: (Top) Total spin S for corresponding electronic complexes. (Bottom) Coulomb blockade spectrum of many-body groundstates as a function of relative backgate voltage where $V_0 = 1.483$ meV is the voltage corresponding to single electron occupancy in the quantum dot, with chemical potential set at the top of the valence band.

the diagonalization of the many-body Hamiltonian (4.4) in a basis consisting of all possible configurations built with a set of single particle states. In this work, we retain 40 conduction band states. This basis already assured converged results for multi-exciton states in a similar quantum dot [4]. For example, for $N_e = 4$ electrons with total spin $S = 0$, the Hilbert space consists of $85,048$ configurations while for $S = 1$ we find $85,325$ configurations. The overlap of the triplet configuration shown in Fig. 4.2 with the numerically obtained ground state is found to be high, with a value of 0.97. In Fig. 4.2 we show schematically configurations with significant overlap with the correlated ground state of the electron complexes consisting of $N_e = 1 - 8$ electrons.

4.3.3 Coulomb Blockade Spectroscopy

The many-body effects manifest themselves in the Coulomb Blockade Spectroscopy [82,86,97,114,115]. To determine the number of electrons N_e in the quantum dot and the effects of their interactions, source and drain leads can be attached and current can be measured as a function of back gate voltage V_g controlling the number of electrons in the quantum dot.

The current flows when the chemical potential of the quantum dot μ equals the chemical potential of the leads resulting in a Coulomb Blockade spectrum [82, 86]. Hence the Coulomb Blockade spectrum as a function of back gate voltage directly measures the many-body N_e and $N_e - 1$ electron ground states, as

$$eV_g = E(N_e) - E(N_e - 1). \tag{4.7}$$

We have computed the chemical potential of the quantum dot, Coulomb Blockade spectrum, for different electron numbers N_e. As shown in the Coulomb Blockade spectrum of the single dot in Fig. 4.2, there are large gaps in between the second and third peaks and between the sixth and seventh peaks [97, 99, 104, 115]. The first gap is due to the *s*-*p* shell energy splitting and the second large gap is due to the *p*-*d* shell energy splitting. The remaining variations in Coulomb Blockade peaks reflect electronic interactions, both exchange and correlations, in degenerate shells [99].

Also shown in Fig. 4.2 is the total electronic spin S of the groundstate as a function of V_g. The oscillatory behaviour between $S = 0$ and $S = 1$ is indicative of Hund's rule being satisfied. It is shown in the Coulomb Blockade spectrum (Fig. 4.2) that a $N_e = 4$ quantum dot with half-filled *p*-shells generates a spin-1 ground state. Further analysis of the $N_e = 4$ half-filled *p*-shell spectrum is necessary in order to understand the electronic and magnetic properties of the InAsP quantum dot nanowire.

4.4 Electronic and magnetic properties of a half-filled p-shell

The evolution of the energy spectrum of the $N_e = 4$ complex in a single dot as a function of increasing number of different electronic configurations is shown in Fig. 4.3. We start with two almost degenerate p_x, p_y orbitals. We place two electrons, one with spin up and one with spin down onto the *p*-shell as shown in Fig. 4.3 (a). Next, we form a spin triplet configuration with $S_z = 0$, schematically shown here with

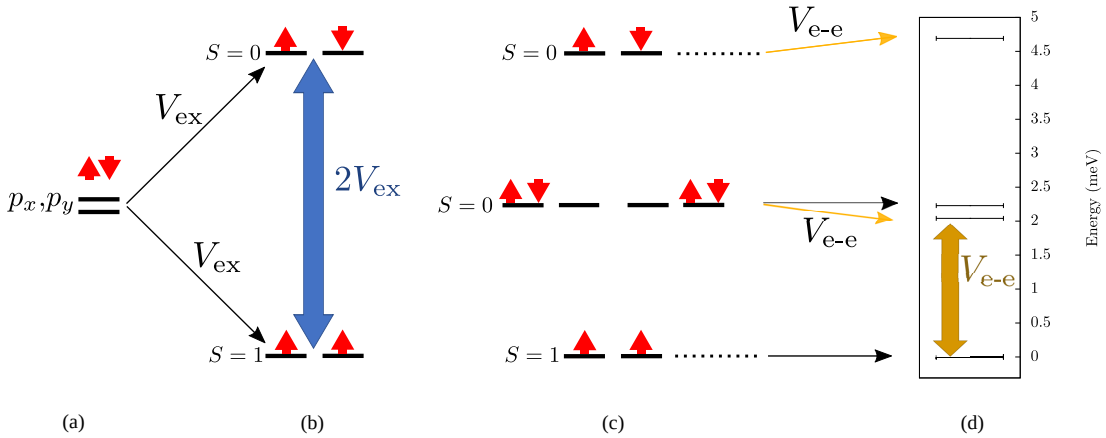

Figure 4.3: (a) Schematic of configurations on the half-filled p-shell. Two electrons occupy the p_x and p_y orbitals. (b) Schematic of the low energy spectrum containing only singly occupied configurations. The ground state is a triplet and the excited state is a singlet. The splitting is twice the exchange energy V_x. (c) The low energy spectrum including doubly occupied configurations. (d) The low energy many-body spectrum from the atomistic simulation. The splitting between the ground state and first excited state is the Coulomb interaction energy V_{ee}.

both spins up, and a spin singlet configuration. The exchange interaction V_{ex} is then turned on. This lowers the energy of spin triplet configuration compared to singlet configuration by $2V_{ex}$, as shown in Fig. 4.3 (b). Finally, we add two doubly occupied configurations, where two electrons, spin up and down, occupy either p_x or p_y orbital as shown in Fig. 4.3 (c).

We next turn on interaction among all singlet singly and doubly occupied configurations. The anti-symmetric combination of doubly occupied configurations remains decoupled from other singlet configurations but a symmetric combination of doubly occupied configurations couples with singly occupied one. This lowers the energy of mostly doubly occupied configurations and increases the energy of mostly singly occupied configurations as shown in Fig. 4.3 (d). For the doubly occupied singlet configuration, the doubly occupied configurations contribute 89% to the total wavefunction and the singly occupied configurations contribute about 6%. The remaining 5% comes from other contributions, such as ones where the d state is occupied. For the singly occupied singlet, contributions are interchanged, where 6% of the wavefunction comes from doubly occupied configurations and 89% comes from singly occupied configurations. So retaining only the singly and doubly occupied configurations on a

p-shell is a reasonable approximation. Finally, the gap Δ separating the triplet and singlet configurations is reduced from $\Delta = 2V_x$ to $\Delta = V_x - \delta$ where δ represents correlation contribution. The important conclusion is that the triplet configuration remains the ground state of the $N_e = 4$ electron complex in accordance with Hund's rules. Since the ground state of a single quantum dot is shown to behave as a spin-1, the next step is to determine whether two quantum dots act as two coupled spin-1s.

4.5 Microscopic theory of two coupled charged $InAs_xP_{1-x}$ quantum dots in InP nanowire

We now turn to two coupled charged InAs quantum dots in InP nanowire. The double dot system consists of two quantum dots with the same dimensions and concentrations as the single quantum dot, with diameter of 18.2 nm and the thickness of 4.1 nm. Cross sections of the two dots in a nanowire with an interdot distance of 5.4 nm are shown in Fig. 4.4 (a). The lower panel shows the probability densty of the s and two p-orbitals. The $z-y$ cross section (bottom panel) shows that the p-orbitals on the two dots form molecular π bonds. This is due to the tunneling between the two dots which gives rise to eigenstates that are a linear combination of the local quantum dot orbitals [116]. This is seen more clearly if the dots are approximated as sites containing a local harmonic orbital (LHO) each, with $|B\rangle$ being the bottom dot orbital and $|T\rangle$ being the top dot orbital. If we assume the on-site energy is the same for both sites, then the Hamiltonian in the B T basis of p_x (p_y) orbitals is given by

$$H_{2-\text{site}} = \begin{bmatrix} 0 & -t \\ -t & 0 \end{bmatrix} \tag{4.8}$$

where t is the tunneling matrix element mixing the two sites. The eigenstates are then symmetrical $|S\rangle = \frac{1}{\sqrt{2}}(|T\rangle + |B\rangle)$, and antisymmetric $|AS\rangle = \frac{1}{\sqrt{2}}(|T\rangle - |B\rangle)$ linear combinations of T and B orbitals, with energies $-t$ and t, respectively. The symmetric-antisymmetric splitting is thus $2t$.

For the atomistic double quantum dot in a nanowire, the single particle states come in symmetric-antisymmetric pairs as well, where each energy level is labelled with the corresponding orbital [107,117]. As is the case with the single dot nanowire, the charge probability densities for the double dot exhibit s, p and d symmetry as seen in Fig. 4.4 (b). The tunneling strength for given orbitals on the two dots, which is half of the symmetric-antisymmetric energy splitting, decreases exponentially with respect to interdot distance. The tunneling matrix element for p-shell orbitals as a function of interdot distance is defined as $|t| = E_{A,p_x} - E_{S,p_x}$. Using the least squares method, the tunneling matrix element dependence on interdot distance was obtained from atomistic energy splittings with an error of about $\chi^2 = 0.06$ meV^2. The exponential dependence of the tunneling strength on interdot distance allows for tuning of the tunneling matrix element. In addition to interdot tunneling, electron-electron interactions between the dots must be taken into account in order to understand the properties of the half-filled p-shell configuration of the double dot.

4.6 Electronic and magnetic properties of two coupled $InAs_xP_{1-x}$ quantum dots with half-filled p-shell each

We now turn to the analysis of properties of two coupled quantum dots, each with the half-filled p-shell configuration. To do this we must diagonalize the many-body Hamiltonian (4.4) for $N_e = 8$ electrons where index i denotes single particle eigenstates of the double dot tight-binding Hamiltonian (4.3). We construct $76,904,685$ possible $N_e = 8$ electron configurations on $N_c = 40$ single particle states and diagonalize the many-body Hamiltonian. The numerically obtained low energy many-body spectrum $E(n)$ for $N_e = 8$ electrons in a double quantum dot nanowire is shown in Fig. 4.5

We see that the lowest energy, $n = 0$, state with energy E_0 is non-degenerate and is the singlet state. The next in energy are the three states E_1-E_3 of almost degenerate

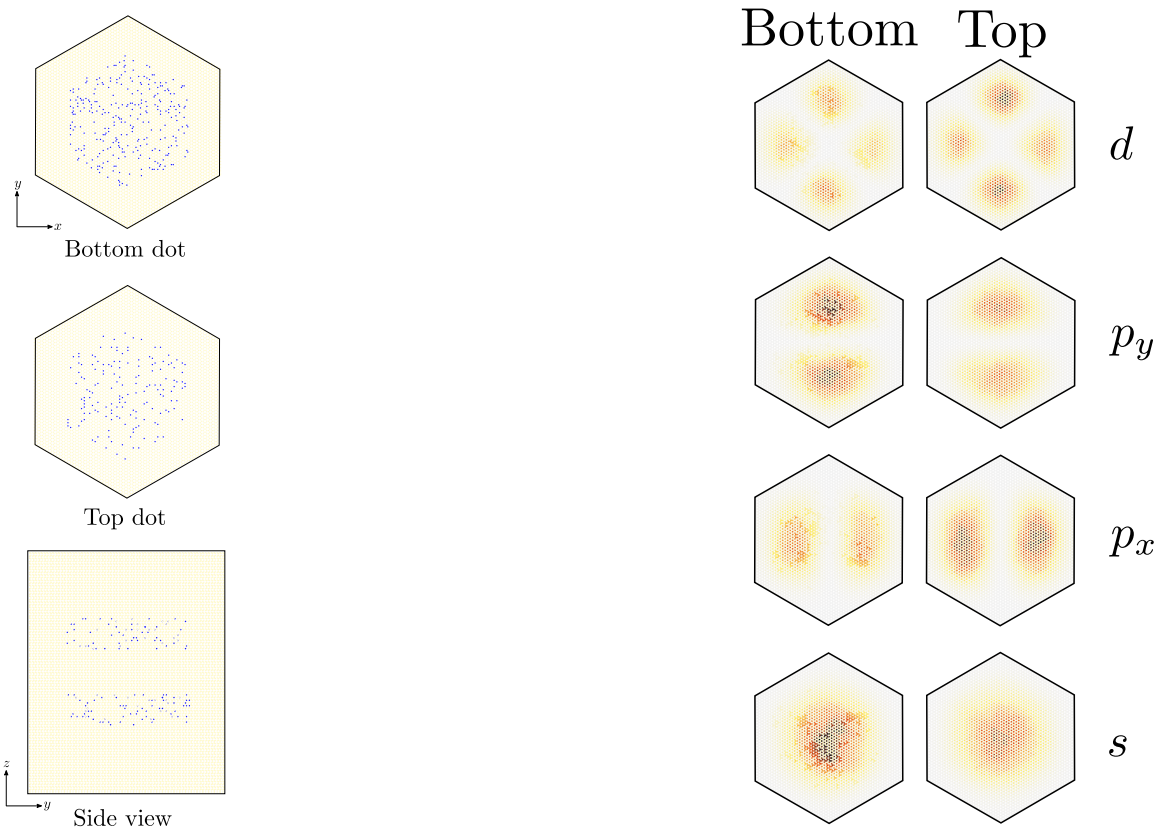

Figure 4.4: (a)Cross sections of the double dot nanowire structure containing about 435000 atoms. The As atoms are blue and both the In and P atoms are yellow. (b) Charge densities of the single particle states.

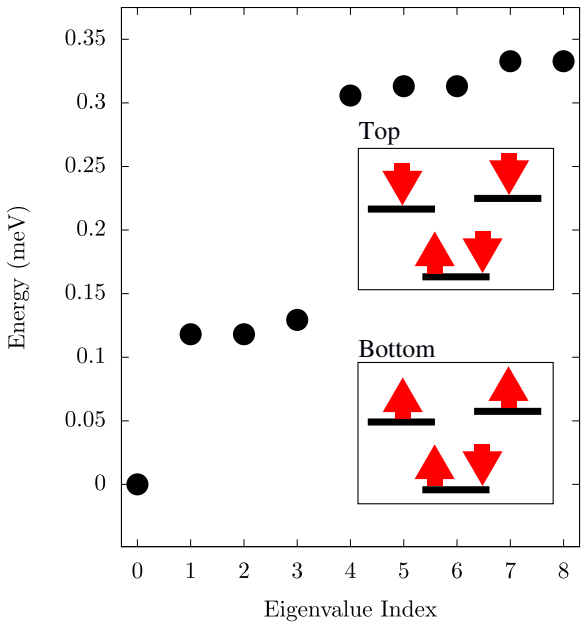

Figure 4.5: Many-body spectrum of the 8 electron complex for a double quantum dot nanowire of 14.9 nm interdot distance. The inset shows schematic half-filled p-shell configurations on top and bottom quantum dots.

triplet followed by a quintuplet E_4-E_8 of almost degenerate states. This low energy spectrum is identical to the spectrum of two spin 1s, S_1 and S_2, coupled by exchange interaction and described by the Heisenberg Hamiltonian $H = J_{AF}\vec{S_1} \cdot \vec{S_2}$, where J_{AF} is the interdot Anti-Ferromagnetic exchange constant, which is discussed in further detail in the following section. The differences between the microscopic spectrum and that of a Heisenberg chain are due to small contributions from higher energy configurations, such as doubly occupied configurations and configurations that contain d shell orbitals and higher. Such contributions are the largest for the quintuplet state. We now use the numerical spectrum of the $N_e = 8$ complex to obtain parameters for a simplified microscopic model, the Hubbard-Kanamori model.

4.7 Effective Hubbard-Kanamori Model

Though the many-body Hamiltonian, Eq. (4.4), provides an accurate description of the electronic complexes in up to 2 quantum dots in a nanowire it cannot be extended to a larger number of quantum dots with 4 electrons per dot. Hence we discuss the simplified Hubbard-Kanamori model capturing the essential features that might give rise to the behaviour of a Heisenberg spin-1 chain. In this model, the s-shell electrons are frozen and we retain only two orbitals, p_+ and p_-, and two electrons on each quantum dot.

4.7.1 The Hubbard-Kanamori Hamiltonian

To derive the Hubbard-Kanamori Hamiltonian, we start with the many-body Hamiltonian written in the basis of p_+ and p_- degenerate orbitals localized on each idealized, disorder free quantum dot. The many-body Hamiltonian in this basis is given by

$$H_{MB} = \sum_{i,\alpha,\sigma} E_{i\alpha\sigma} c^{\dagger}_{i\alpha\sigma} c_{i\alpha\sigma} + \sum_{\sigma} \sum_{ij} \sum_{\alpha\beta} t_{i\alpha,j\beta} c^{\dagger}_{i\alpha\sigma} c_{j\beta\sigma}$$
$$+ \frac{1}{2} \sum_{\sigma\sigma'} \sum_{ijkl} \sum_{\alpha\beta\gamma\delta} \langle i\alpha, j\beta | V | k\delta, l\gamma \rangle c^{\dagger}_{i\alpha\sigma} c^{\dagger}_{j\beta\sigma'} c_{k\delta\sigma'} c_{l\gamma\sigma} \tag{4.9}$$

where the Roman indices i, j, k and l denote quantum dot number, indices α, β, δ and γ denote quantum dot orbitals p_+ or p_-, and σ denotes the electron spin. Here, the first term describes energies of degenerate p-shell orbitals, the second term describes interdot tunneling and intradot disorder and the third term describes intra and inter dot electron-electron interactions. With the first term describing energies of two degenerate p orbitals, $t_{i\alpha,i\beta}$ describes mixing of p_+, p_- orbitals on the same dot i by the atomistic disorder, leading to an energy splitting Δ while $t_{i\alpha,i+1\alpha}$ describes tunneling of electron between p_+ (p_-) orbitals on neighboring dots. For two dots, this tunneling translates to the symmetric (antisymmetric) orbitals and energy splitting.

To simplify (4.9) further, all interdot and intradot tunneling matrix elements are written as

$$t_{i\alpha\sigma,i\beta\sigma} \equiv \frac{\Delta}{2} \tag{4.10}$$

$$t_{i\alpha\sigma,j\alpha\sigma} \equiv t \tag{4.11}$$

for all i, α, β and σ. Moreover, all of the other tunneling matrix elements are zero since all tunneling, intradot or interdot, conserves spin and interdot tunneling conserves orbital angular momentum.

In the spirit of the Hubbard-Kanamori model, similar approximations are made for the electron-electron interaction matrix elements, where the only nonzero matrix

elements between nearest neighboring dots 1 and 2 are

$$\langle 1\alpha, 1\beta|V|1\beta, 1\alpha\rangle = \langle 1\alpha, 1\alpha|V|1\alpha, 1\alpha\rangle \equiv U \tag{4.12}$$

$$\langle 1\alpha, 1\beta|V|1\alpha, 1\beta\rangle \equiv \frac{J}{2} \tag{4.13}$$

$$\langle 1\alpha, 2\alpha|V|2\alpha, 1\alpha\rangle \equiv V \tag{4.14}$$

$$\langle 1+, 2-|V|2+, 1-\rangle \equiv W \tag{4.15}$$

Note the last Coulomb matrix element W conserves the total angular momentum of the electron pair but corresponds to scattering of electron pair from dot 1 to dot 2 with exchange of electrons. With all of these reductions, the many-body Hamiltonian (4.9) reduces to the Hubbard-Kanamori Hamiltonian for two dots given by

$$\begin{aligned} H =& H_0(1) + H_0(2) \\ &+ \sum_{\alpha\sigma}(t_{12}c^\dagger_{1\alpha\sigma}c_{2\alpha\sigma} + t_{12}c^\dagger_{2\alpha\sigma}c_{1\alpha\sigma}) \\ &+ V(n_{1,+} + n_{1,-})(n_{2,+} + n_{2,-}) \\ &+ WL^+_1L^-_2 + W^*L^-_1L^+_2 \end{aligned} \tag{4.16}$$

where $H_0(1)$ is the Hubbard-Kanamori Hamiltonian for a single quantum dot

$$\begin{aligned} H_0 =& \sum_{\alpha,\sigma} E_{\alpha,\sigma}n_{\alpha,\sigma} + \frac{\Delta}{2}\sum_{\sigma}\sum_{\alpha\neq\beta} c^\dagger_{\alpha\sigma}c_{\beta\sigma} \\ &+ Un_{-\uparrow}n_{-\downarrow} + Un_{+\uparrow}n_{+\downarrow} \\ &+ (U - \frac{J}{4})(n_{-\uparrow} + n_{-\downarrow})(n_{+\uparrow} + n_{+\downarrow}) + \\ &- J\mathbf{S}_- \cdot \mathbf{S}_+ \end{aligned} \tag{4.17}$$

where $\alpha \in \{+, -\}$ labels the two degenerate orbitals p_-, p_+, $E_{\alpha,\sigma} = E$ are the energies of the two degenerate orbitals and Δ describes mixing of p-shell orbitals by microscopic disorder and lattice effects, ferromagnetic exchange coupling J aligns the spins of two

p-shell electrons, $n_i = n_{i,\uparrow} + n_{i,\downarrow}$ is the number of electrons on state with quantum number i, $S^+_{i\alpha} = c^\dagger_{i\alpha\uparrow} c_{i\alpha\downarrow}$, $S^-_{i\alpha} = (S^+_{i\alpha})^\dagger$, $S^z_{i\alpha} = \frac{1}{2}\left(c^\dagger_{i\alpha\uparrow} c_{i\alpha\uparrow} - c^\dagger_{i\alpha\downarrow} c_{i\alpha\downarrow}\right)$, $L^+_i = \sum_\sigma c^\dagger_{i+\sigma} c_{i-\sigma}$ and $L^-_i = (L^+_i)^\dagger$.

We note that while the tunneling of a single electron from one dot to another conserves the angular momentum, i.e., tunneling takes place between p_+ orbital on one dot to p_+ orbital on neighboring dot, the last term is a bit unusual, it involves tunneling of two electrons, one electron from $p+$ orbital on one dot to p_- orbital on the second dot simultaneous with second electron tunneling from p_- orbital to p_+ orbital on a second dot. Hence the total angular momentum of electron pair is conserved but electrons change orbitals in a scattering event. We also note the presence of ferromagnetic Heisenberg coupling J, which is the exchange interaction between two electrons on the p-shell in the same quantum dot. The coupling of the two spins on dots 1 and 2 is described by the interdot tunneling and interactions. All the parameters entering the Hubbard-Kanamori Hamiltonian will be extracted from a microscopic model below.

4.7.2 Analysis of Hubbard-Kanamori model for a single quantum dot

The Hubbard-Kanamori spectrum of two electrons in a single dot is obtained by diagonalizing the Hamiltonian, (4.17), in the basis of L_z, S^2 and S^z simultaneous eigenstates constructed out of singly and doubly occupied two electron configurations, with the spectrum identical to the one computed microscopically and shown in Fig. 4.3 (d). The eigenvalues of the single dot Hubbard-Kanamori Hamiltonian are $E_T = 2E$ for a three fold degenerate triplet and three singlet states $E_{S1} = 2E + \frac{1}{4}(3J - \sqrt{J^2 + (4\Delta)^2})$, $E_{S2} = 2E + \frac{J}{2}$, $E_{S3} = 2E + \frac{1}{4}(3J + \sqrt{J^2 + (4\Delta)^2})$

When the p-shell splitting is zero, the splitting between the triplets and the doubly occupied singlets is equal to the intrashell exchange J while the splitting J between 3 triplets and the singly occupied singlet is twice the exchange matrix element. When p-shell splitting Δ is nonzero, the degeneracy of the doubly occupied configurations is

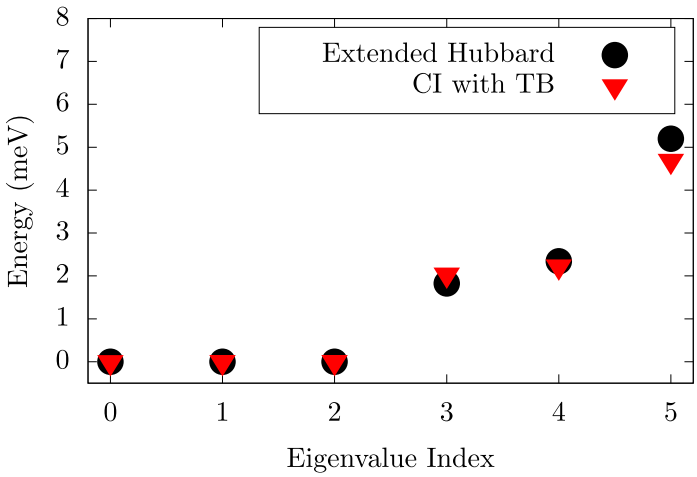

Figure 4.6: Comparison between Hubbard-Kanamori and atomistic spectra

lifted and the singly occupied singlet increases in energy. This is due to the fact that the p-shell mixing couples one of the doubly occupied configurations to the singly occupied singlet. The triplet states remain uncoupled because p-shell mixing must conserve S and S^z. With the full energy spectrum expressed in terms of the Hubbard-Kanamori parameters, fitting the Hubbard-Kanamori spectrum to the atomistic spectrum shown in Fig. 4.3 (d) enables the extraction of Hubbard-Kanamori parameters. We find for the typical $InAs_xP_{1-x}$ quantum dots studied here $U = 16$ meV, $J = 5$ meV and $\Delta = 0.8$ meV. For these parameters we show in Fig. 4.6 both the Hubbard-Kanamori spectrum and the full microscopic spectrum of 4 electrons on a single dot.

The Hubbard-Kanamori and atomistic spectra are in close agreement. The largest difference of 0.5 meV is in the energy of singly occupied singlet. Just as in the atomistic spectrum, the ground state is the three fold degenerate triplet, followed by two doubly occupied singlet states and a singly occupied singlet. As discussed before, the spin-polarized ground state can be understood in terms of the exchange coupling between the p-shell electrons as shown in Eq.(4.16). Having shown the correspondence between the Hubbard-Kanamori and atomistic models for a single quantum dot, we can now use these single quantum dot parameters in the double quantum dot Hubbard-Kanamori Hamiltonian to determine the double quantum dot spectrum for 4 electrons on two p-shells.

4.7.3 Analysis of Hubbard-Kanamori model for a double quantum dot

Unlike in the single quantum dot, analytically determining the many-body spectrum for a double quantum dot consisting of 4 p-shell states and 4 active electrons would be difficult as the Hilbert space of the Hubbard-Kanamori model consists of 70 configurations. We hence fit the Hubbard-Kanamori spectrum, Eq.(4.16), to the atomistic spectra numerically. To better understand the effect of interdot tunneling and interactions on the double dot spectrum we start with a double dot without tunneling and interactions. Assuming the two quantum dots are identical, we form eigenstates with 2 electrons on each p-shell by forming products of many-body eigenstates between the two single quantum dots provided S and L are conserved. Examples of these eigenstates formed in this manner are the ground states of maximal S^z given by

$$\begin{aligned}
|S_{\mathrm{T}}=0,S^z=0\rangle =&\alpha_{\mathrm{s}}(|\downarrow\downarrow;\uparrow\uparrow\rangle+|\uparrow\uparrow;\downarrow\downarrow\rangle)\\
&+\beta_{\mathrm{s}}(|\downarrow\uparrow;\uparrow\downarrow\rangle+|\downarrow\uparrow;\downarrow\uparrow\rangle\\
&+|\uparrow\downarrow;\downarrow\uparrow\rangle+|\uparrow\downarrow;\uparrow\downarrow\rangle)\\
|S_{\mathrm{T}}=1,S^z=1\rangle =&\alpha_{\mathrm{t}}(|\uparrow\uparrow;\uparrow\downarrow\rangle+|\uparrow\uparrow;\downarrow\uparrow\rangle\\
&-|\uparrow\downarrow;\uparrow\uparrow\rangle-|\downarrow\uparrow;\uparrow\uparrow\rangle)\\
|S_{\mathrm{T}}=2,S^z=2\rangle =&\alpha_{\mathrm{q}}|\uparrow\uparrow;\uparrow\uparrow\rangle
\end{aligned} \tag{4.18}$$

Here we neglect eigenstates with triple and quadruple occupancy in a quantum dot. The energies of these configurations would be higher in energy by U. A schematic for the noninteracting Hubbard-Kanamori spectrum without tunneling and electron-electron interactions is shown in Fig. 4.7. The left hand side shows the Hubbard-Kanamori spectrum of two noninteracting quantum dots with 2 electrons each. The spectrum is the same as an Hubbard-Kanamori spectrum of a single dot but degenerate. Hence the lowest energy band consists of 3 triplet states on each dot, with a total of 9 states.

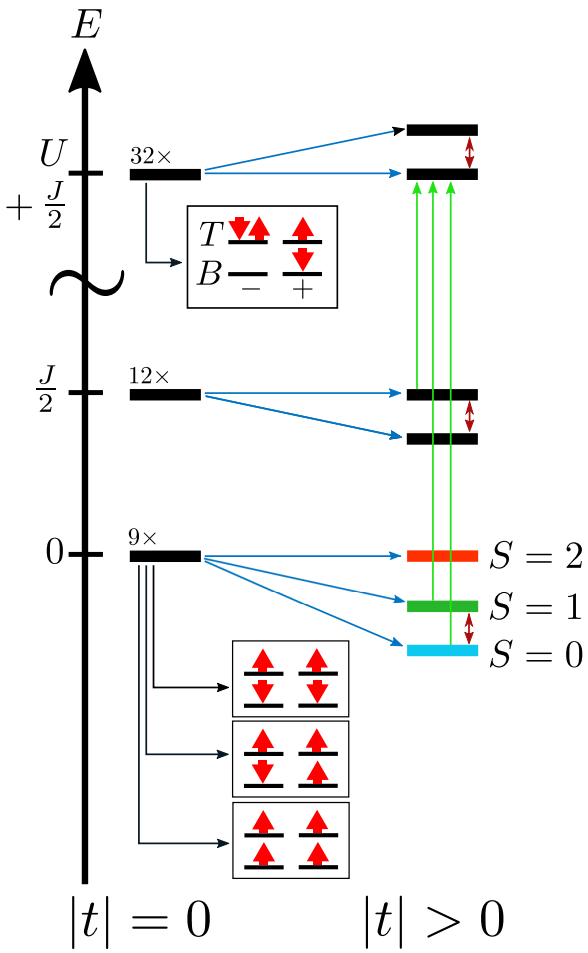

Figure 4.7: Schematic energy spectrum of a double quantum dot. On the left is the double dot spectrum when $t = 0$ and on the right is the spectrum when $|t| > 0$. The bottom insets show the configurations of one of terms of the $S^z = 0$ triplet as well as the $S^z = -1$ and $+1$ triplet states configurations. The top inset shows one of the configurations that contain three electrons in one dot. Blue arrows indicate splittings of levels due to tunneling. On the right, the green arrows indicate coupling between states due to tunneling. The red, green and cyan states correspond to the singlet, triplet and quintuplet states. The double headed red arrows indicate a splitting of $\frac{2t^2}{U+J/2}$

The right hand panel shows the energy spectrum of a double dot as interdot tunneling is turned on. We see that the singlet, triplet and quintuplet states are no longer degenerate. This is due to the singlets and triplets coupling to the triply occupied configurations as shown in Fig. 4.7. The quintuplet states however remain uncoupled since tunneling conserves S. Most importantly, the singlet, triplet and quintuplet degeneracies are lifted in a manner that resembles the spectrum of a Heisenberg chain of spin-1 particles with coupling $J_H = \frac{2t^2}{U+J/2-V}$. The reduction of the Hubbard-Kanamori Hamiltonian (4.16) to the Heisenberg spin-1 chain Hamiltonian is discussed in further detail in Ref. [118] where interdot tunneling is treated perturbatively. In essence, the behaviour of coupled spin-1 spins arises when the ferromagnetic intradot coupling J between electrons on two different p-shell orbitals is much stronger than the interdot coupling between composite spin-1 particles (i.e. $J \gg J_H$). If J_H is large, then the tunneling is no longer a perturbation and the intradot coupling J is no longer strong enough to hold two electron spins parallel in a single quantum dot.

The Hubbard-Kanamori parameters for the double quantum dot are obtained in a similar manner as for the single quantum dot system. First initial guesses are made by relating the parameters to the atomistic single particle spectrum and Coulomb matrix elements. However, in the case of the double quantum dot, a genetic algorithm is used to make adjustments to the parameters to obtain accurate fit to the microscopic many-body spectrum. The algorithm is as follows. First random parameters are generated within a small vicinity around the initial guesses in parameter space and used to compute the low energy many-body spectra. Out of those guesses, another set of random points is generated, but in a smaller vicinity around the previous set of parameters that yielded a spectrum closest to the atomistic low energy spectrum. This process is repeated until the difference between the Hubbard-Kanamori and atomistic spectra is below a threshold value and the result is a set of fitted Hubbard-Kanamori parameters. To obtain the fitted parameters, only t, V and W were varied while the rest of the parameters were held stationary in the genetic algorithm. The set of parameters for this system are given in Table 4.1.

Table 4.1: Fitted Hubbard-Kanamori Parameters for the double quantum dot nanowire

Fitted HK Parameter	Numerical Value (meV)
U	15.971
$\frac{J}{2}$	2.500
Δ	0.844
t	0.748
V	7.734
W	0.000

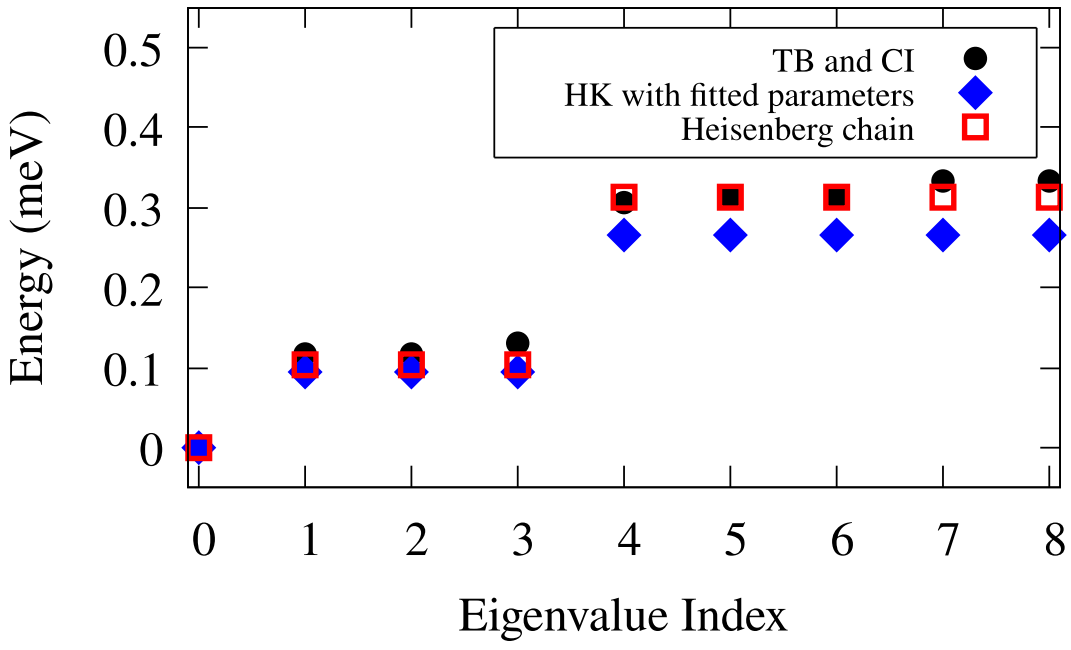

Figure 4.8: Comparison between atomistic, Hubbard-Kanamori and Heisenberg chain spectra.

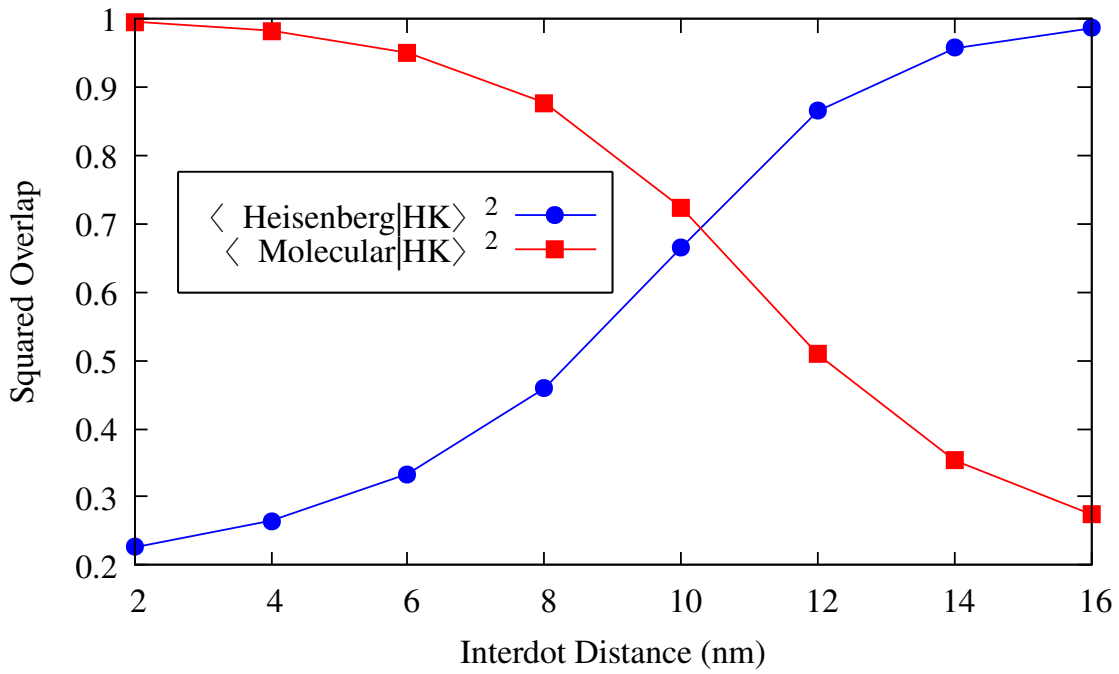

Figure 4.9: Comparison between the overlaps of the Hubbard-Kanamori groundstate with the Heisenberg $S = 1$ groundstate and the molecular groundstate.

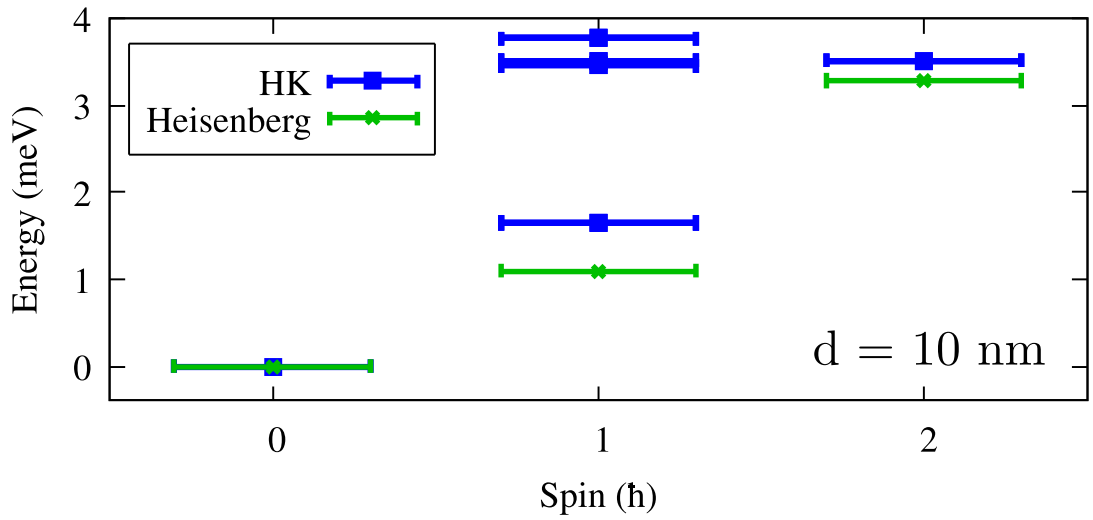

Figure 4.10: Hubbard-Kanamori and Heisenberg low energy spectrum as a function of total spin S

We then compare atomistic, Hubbard-Kanamori and Heisenberg chain spectra in Fig. 4.8. Here, the Heisenberg coupling is chosen to be $J_H = \frac{2t^2}{U+\frac{J}{2}-V} = 0.104$ meV. The agreement between all three spectra indicate that not only is the parametrized Hubbard-Kanamori model a valid approximation of the atomistic Hamiltonian, but that the Hubbard-Kanamori model does in fact exhibit properties of the Heisenberg chain. Though the Heisenberg coupling increases as a function of interdot distance, there is a limit to the magnitude of J_H. This is shown in Fig. 4.9 with the comparison between overlaps of the Hubbard-Kanamori groundstate with the groundstates of the Heisenberg Hamiltonian and the molecular Hamiltonian given by

$$H_{\text{Mol.}} = t \sum_{\alpha\sigma} c^{\dagger}_{1\alpha\sigma} c_{2\alpha\sigma} + (\text{c.c.}) \tag{4.19}$$

In the molecular Hamiltonian, the energy spectrum is dominated by interdot tunneling, with two spin up and down electrons occupying a molecular symmetric p_+ and p_- orbitals instead of forming spin one states on each dot. The Heisenberg triplet groundstate increasingly becomes a more accurate description of the Hubbard-Kanamori groundstate as the interdot distance increases. Conversely, molecular groundstate is a better description for smaller interdot distances when interdot tunneling dominates. At an interdot distance of 10 nm, the Heisenberg groundstate accounts for $\sim$70% of the composition of the Hubbard-Kanamori groundstate. Furthermore, at this interdot distance, the system is adequately described in terms of coupled spin-1 particles while simultaneously keeping J_H rather large. It is worth noting that the squared overlaps for a given interdot distance do not sum to unity due to the fact that the Heisenberg and molecular groundstates are not orthogonal to each other.

As shown in Fig 4.10, the Hubbard-Kanamori and Heisenberg spectra are in agreement with a χ^2 error of $\sim$0.35 meV. This interdot distance yields an effective maximum for the magnitude of the Heisenberg coupling, which in this case is $J_H = 1.096$ meV.

4.8 Conclusion

We described here electronic properties of multi-electron complexes in InAsP quantum dots in InP nanowires using a combination of a microscopic many-body Hamiltonian based on atomistic tight-binding single particle states and Configuration Interaction approach to electron-electron interactions. We determined the evolution of total spin of ground state of electronic complexes with electron number and found the synthetic spin one state for $N_e = 4$ electrons in a dot. We related the evolution of total spin to generalised Hunds rule and discussed detection using Coulomb Blockade Spectroscopy. We extended the microscopic model to two tunnel coupled quantum dots in a nanowire. We determined the electronic spectra as a function of interdot coupling. We computed the $N_e = 8$ electron complex, with 4 electrons per quantum dot. The low energy spectra of Hubbard-Kanamori and Heisenberg Hamiltonians were fitted to the low energy spectra of a microscopic Hamiltonian and understood in terms of antiferromagneticaly coupled two spin one complexes on each dot. The Hubbard Kanamori parameters and interdot exchange coupling were determined from microscopic calculations. This analysis has shown that a chain of $InAs_{1-x}InP_x$ quantum dots in InP nanowire can be used to construct a synthetic Heisenberg spin one chain described by the Hubbard-Kanamori model. Because of the reduction of the Hilbert Space, the Hubbard-Kanamori model will allow for microscopic understanding of macroscopic chains which could be used to construct macroscopic quantum states and topologically protected qubits.

Acknowledgments

J.M., M.C., A.A. and P.H. would like to thank B. Jaworowski, M. Korkusinski, Y.Saleem, L. Szulakowska and A. Dusko for the fruitful discussions . J.M., M.C., A.A. and P.H. acknowledges support from NSERC Discovery and Strategic QC2DM Project Grants and Compute Canada for computing resources. M.C. acknowledges support from the Humboldt Foundation.

Chapter 5

Microscopic design of a topologically protected singlet-triplet qubit using an InAsP quantum dot array

My Contribution

As the lead author of this paper, I performed the computations for all manybody spectra of the various quantum dot systems. These computations included the spectrum of the chain of quantum dots as a function of system size, the spectrum as a function of magnetic field and the phase diagrams. As for the computational techniques, with the help of Post-Doctorate Fellow Daniel Miravet, I wrote the computational tool used in the DMRG calculations. Also with the help of Daniel Miravet, I compared the results with results obtained using exact diagonalization as well as results obtained using the well known DMRG tool iTensor. Furthermore, I wrote the manuscript as well as created all of the figures.

Authors

Jacob Manalo, Daniel Miravet, Pawel Hawrylak

Abstract

We present here the steps enabling the microscopic design of a topologically protected singlet-triplet qubit in an InAsP quantum dot array embedded in an InP nanowire. The qubit is constructed with two Haldane spin-$\frac{1}{2}$ quasiparticles in a synthetic spin one chain. The qubit is described by a two-leg multi-orbital Hubbard Kanamori (HK) model with parameters obtained from the microscopic calculations of up to eight electrons in a single and double quantum dot. In this HK model describing long arrays of quantum dots, using both exact diagonalization and matrix product state (MPS) tools, we demonstrate a four-fold quasidegenerate ground state separated from excited states by a finite energy gap similar to a Heisenberg spin-1 chain in the Haldane phase. We demonstrate the existence of spin-$\frac{1}{2}$ quasiparticles at the edges of the chain by observing the magnetic field dependence of the low energy spectrum as a function of applied magnetic field. The applied magnetic field also isolates the singlet and $S^z = 0$ triplet states from the other triplet components allowing these states to serve as a qubit basis. Most importantly, the regions in parameter space where the low energy spectrum of the multi-orbital Hubbard chain yields a Heisenberg spin-1 chain spectrum are mapped out. Due to the finite energy gap, this qubit has the potential to be protected against perturbations.

5.1 Introduction

The development of solid state quantum information processing devices is currently a research area of great interest [3, 119–122]. At the moment, qubits developed for commercial use are superconducting [19–21], trapped ion [25, 26], electron spin [2, 84, 123, 124] and photonic qubits [22–24] due to their robustness and scalability [22, 23,

125–127]. However, these qubits suffer from decoherence and a quest for topologically protected qubits continues [16, 128, 129]. Recently, a qubit constructed with two Haldane spin-$\frac{1}{2}$ quasiparticles [17, 18, 130] in a synthetic spin one chain [15, 16] has been proposed [10, 15, 131]. A synthetic spin one chain could be realised using gated triple quantum dots [131], array of semiconductor quantum dots in a nanowire [5, 15] and a chain of triangular graphene quantum dots [132–134]. Here, we discuss the atomistic design of a synthetic spin-1 chain using a semiconductor quantum dot array in a nanowire to realize a topologically protected singlet-triplet qubit.

Previous effective mass and Heisenberg model based spin calculations suggested that such a qubit can be realized using a chain of InAsP semiconductor quantum dots with 4 electrons each in a InP nanowire [5, 15, 16]. Furthermore, it has been shown through microscopic calculations that the ground state of a single InAsP quantum dot in a nanowire is a spin triplet and that the low energy spectrum of an array of two InAsP quantum dots in an InP nanowire is similar to the spectrum of a Heisenberg chain of two spin-1 particles [5]. The parameters of this two site Heisenberg Hamiltonian were used to extend the Heisenber spin-1 chain.

Here, instead of effective Heisenberg Hamiltonian we derive and use an effective multi-orbital Hubbard model with parameters obtained from microscopic atomistic calculations. We determine a set of microscopic parameters for which a long macroscopic quantum dot chain with 4 electrons each has a four-fold quasi-degenerate ground state separated from the quintuplet state by a finite energy gap, similar to a Heisenberg spin-1 chain. We also show that the electrons in a quantum dot array behave the same way as two coupled spin-$\frac{1}{2}$ quasi-particles would in a magnetic field.

Furthermore, we show that the length of array controls the singlet-triplet splitting while the Zeeman splitting of the nonzero spin triplet states allows us to isolate the quasi-degenerate singlet and triplet states from the quintuplet allowing the isolated states to serve as a qubit basis. We then demonstrate that the multi-orbital Hubbard parameters which result in a Heisenberg spin-1 chain model form distinct regions in parameter space and not sporadic regions. Determining these parameters allows for

the fine tuning of the spectral gap. The parameters are modified by controlling the size and As concentration of the InAsP quantum dot as well as interdot distance and material of the quantum dot array enabling construction of robust topologically protected singlet-triplet qubits.

The paper is organized as follows. First, we define the multi-orbital Hubbard model in terms of individual quantum dots and the interaction between them. We then describe the methodology of the calculations which include exact diagonalization and density matrix renormalization group (DMRG) in the formalism of matrix product states (MPS) [34,35,35,135]. Next, we analyze the low energy spectrum as a function of array size and show the behaviour of the chain in a magnetic field. Finally, we map out regions in parameter space where the multi-orbital Hubbard model gives a low energy spectrum that resembles that of the Heisenberg spin-1 chain.

5.2 InAsP Quantum Dot Array in an InP nanowire

We aim to realize a synthetic spin-1 chain with an array of InAsP quantum dots embedded in an InP nanowire. The quantum dot array is constructed with a single InAsP quantum dot shown in Fig. 5.1(a) as a building block. It has been shown that a synthetic spin-1 object is formed when 4 electrons are injected into the InAsP quantum dot [5]. With each InAsP quantum dot acting as a spin-1 object, we construct a synthetic spin-1 chain with an array of these InAsP quantum dots as shown in Fig. 5.2.

The microscopic calculations for one and two InAsP quantum dots embedded in an InP nanowire serve as the foundation for the effective multi-orbital Hubbard model that describes the InAsP quantum dot array. Essentially, the microscopic calculations begin with a tight-binding model [4, 5, 27, 110] where the quantum dot nanowire is created by first building an InP matrix and defining a hexagonal nanowire inside as shown in Fig. 5.1(a) where random P atoms are replaced with As atoms at a concentration of 10%. Fig. 5.1(b) shows the probability densities of the single particle states obtained from the tight-binding model. Despite the random distribution of As

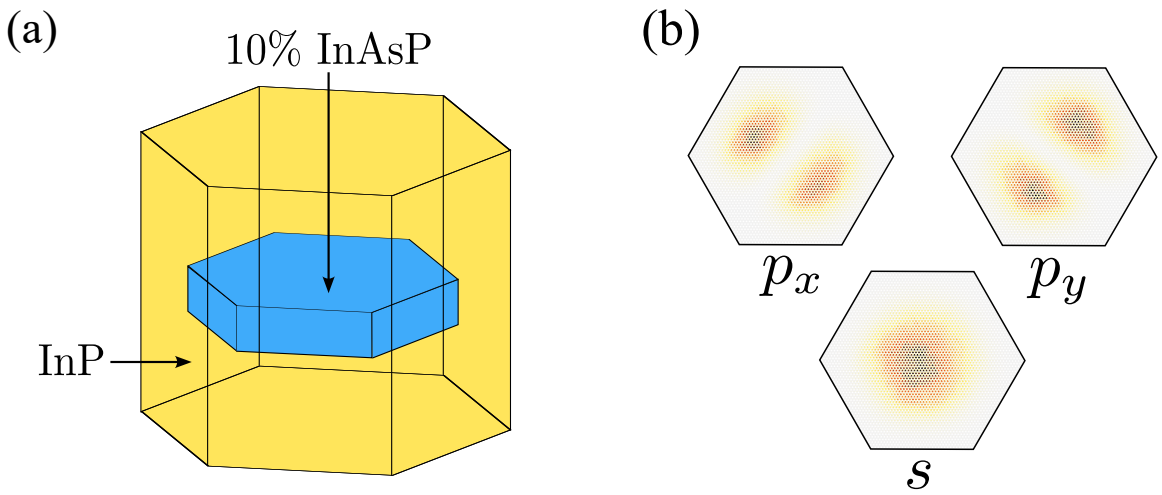

Figure 5.1: (a) Hexagonal InAsP quantum dot (blue) in an InP nanowire (yellow). (b) Charge densities of single particle states.

atoms, the spectrum consists of an s-shell followed by two states of a p-shell.

Furthermore, it was shown that when four electrons were inserted into the quantum dot, two of the electrons filled the s-shell, leaving the other two electrons to form a triplet state on the p-shell. The many-body calculations of the N electron complex were done using the configuration interaction method for the Hamiltonian given by

$$H_{MB} = \sum_i E_i c_i^\dagger c_i + \frac{1}{2} \sum_{ijkl} \langle ij|V|kl\rangle c_i^\dagger c_j^\dagger c_k c_l \tag{5.1}$$

where E_i is the energy of single particle state i, $c_i^\dagger$ (c_i) is the creation (annihilation) operator for an electron on state i and $\langle ij|V|kl\rangle$ is the Coulomb matrix element where two electrons, one in state i and another in state j scatter to states k and l. Likewise, the many-body spectrum of two quantum dots, each with four electrons, resembled the spectrum of two coupled spin-1 particles. The limitation of these microscopic calculations extended to a long chain of quantum dots is that they are computationally expensive. Computing such arrays where each quantum dot contains millions of atoms, with each atom containing 20 spin-up and spin-down orbitals, and 4 electrons per quantum dot is not possible. Since the singlet-triplet qubit requires a chain of many synthetic spin-1 quasiparticles, it is necessary to use a simplified model that still captures the physics of a spin-1 chain.

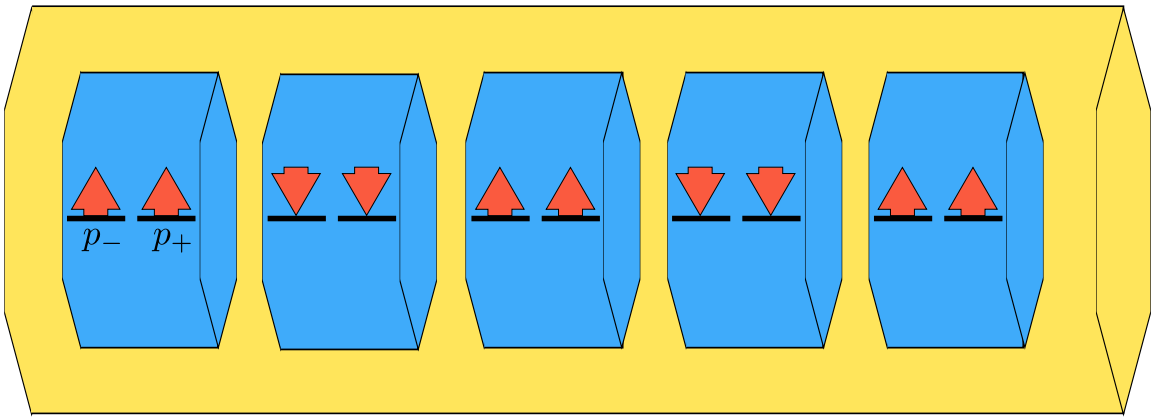

Figure 5.2: A chain of InAsP quantum dots (blue) embedded in an InP nanowire (yellow). Red arrows indicate electrons with corresponding spin.

5.3 The Multi-Orbital Hubbard Model

We now turn to the effective multi-orbital Hubbard model to describe the quantum dot array shown in Fig. 5.2. In this model, each quantum dot is described as a site with two p orbitals, p_- and p_+. Here, s-shell electrons are ignored because the probability of s electrons scattering to the p-shell is negligible due to the large s-p splitting in the microscopic single-particle spectrum. Exchange interaction of additional two electrons half-filling the p-shell can ferromagnetically couple their spins to form a synthetic spin-1 state as shown schematically in Fig. 5.2.

To retain essential microscopic description of the quantum dot we reduce the microscopic Hamiltonian in (5.1) to the effective multi-orbital Hubbard Hamiltonian for a single quantum dot given below

$$\begin{aligned} H_0(i) = U_1 \sum_{\alpha} n_{i\alpha\uparrow} n_{i\alpha\downarrow} + (U_2 - \frac{J_{1/2}}{4}) n_{i-} n_{i+} \\ - J_{1/2} \mathbf{S}_{i-} \cdot \mathbf{S}_{i+} + \frac{\Delta}{2} \sum_{\sigma} \sum_{\alpha \neq \beta} c^{\dagger}_{i\alpha\sigma} c_{i\beta\sigma} \end{aligned} \tag{5.2}$$

where $\alpha, \beta \in \{-, +\}$ denote the orbital indices, $\sigma \in \{\uparrow, \downarrow\}$ denotes spin and $n_{i\alpha} \equiv \sum_{\sigma} n_{i\alpha\sigma}$ is the number of electrons in orbital α in quantum dot i. This Hamiltonian as well as the Hamiltonian for a chain of quantum dots is derived from the microscopic

Hamiltonian by employing certain approximations to the Coulomb matrix elements as described in Ref. [5].

The first term is the Hubbard term, which describes the energy U_1 required for a spin-up and spin-down electron to occupy a single orbital. The second term describes the coupling between electrons on the p_- and p_+ shells with energy $(U_2 - J_{1/2}/4)$. Here, U_2 is the direct Coulomb interaction between an electron on p_- and an electron on p_+ and $J_{1/2}$ is the exchange between them. In general, U_1 and U_2 differ in value, but for the systems we are interested in, $U_1 = U_2 \equiv U$. The following $J_{1/2}$ term describes the Heisenberg ferromagnetic coupling between p_- and p_+ electrons, which is not to be confused with the effective Heisenberg spin-1 coupling between quantum dots, hence the subscript 1/2 in the coupling constant $J_{1/2}$. This spin-$\frac{1}{2}$ coupling arises from the exchange interaction between electrons on different orbitals. Finally, the last term describes the p-shell splitting due to the broken lateral symmetry of the quantum dot from the random distribution of As atoms, where the energy splitting Δ is the splitting between the p_x and p_y orbitals which are both linear combinations of p_- and p_+.

To compute the spectrum of a chain of quantum dots, we must include the interaction between the quantum dots. The total multi-orbital Hubbard Hamiltonian is given by

$$H = \sum_i \left(H_0(i) + t \sum_{\alpha\sigma} (c^\dagger_{i\alpha\sigma} c_{i+1\alpha\sigma} + \text{h.c.}) \right) + V \sum_i n_i n_{i+1} \tag{5.3}$$

which is the sum of all single quantum dot Hamiltonians in the array and the interactions between nearest neighboring dots. The first term that describes the interdot interactions is the tunneling term $tc^\dagger_{i\alpha\sigma} c_{i+1\alpha\sigma}$ which describes the process of an electron hopping from quantum dot i to the nearest neighbor quantum dot $i+1$ with a hopping energy t. The second term of the interdot interaction portion of the Hamiltonian describes the electrostatic interaction between electrons on neighboring

quantum dots. Here, $n_i \in [0,4]$ is the electron occupation of dot i and V is the Coulomb matrix element which is direct with respect to dot index and is defined to be $V \equiv \langle i\alpha, j\beta|V|j\beta, i\alpha\rangle$ where $\alpha, \beta \in \{p_+, p_-\}$.

The two most important terms in determining the behaviour of the system as a spin-1 chain are the intradot exchange term $-J_{1/2}\sum_i \mathbf{S}_{i-} \cdot \mathbf{S}_{i+}$, which describes the spin-spin coupling between a p_- electron and a p_+ electron, and the tunneling term $t\sum_i \sum_{\alpha\sigma} c^\dagger_{i\alpha\sigma} c_{i+1\alpha\sigma}$. The intradot exchange term, which controls the electronic behaviour of the quantum dot as a spin-1 object is compromised by the tunneling term, which breaks the spin-1 apart. Without the interdot tunneling term however, the singlet, triplet and quintuplet states of the quantum dot array will all be degenerate which means that there is no finite gap in the spectrum.

The single dot parameters U_1, U_2, $J_{1/2}$, Δ and multidot parameters t and V were obtained by fitting the spectrum of (5.3) to the microscopic tight-binding spectrum of a two dot array using a genetic algorithm. This effective multi-orbital Hubbard model with parameters obtained from microscopic calculations allows us to simulate an array with many dots so that we can construct the topologically protected singlet-triplet qubit.

5.4 Methodology

In this work, we compute the many-body spectrum of a large chain of quantum dots using the multi-orbital Hubbard model and Configuration Interaction and DMRG tools to demonstrate the similarity to the spectrum of a spin-1 chain with two Haldane spin-$\frac{1}{2}$ quasiparticles. Next, we apply a magnetic field to the quantum dot chain to determine the behaviour of the Haldane spin-$\frac{1}{2}$ quasiparticles at the edges as well as to find the magnetic field at which the qubit can operate. Finally, regions in parameter space, i.e. the parameters in (5.2) and (5.3), where the Hubbard chain produces a Heisenberg spin-1 chain spectrum are mapped out.

All calculations of spectra of arrays with two quantum dots are done with exact diagonalization while calculations of spectra of larger arrays are done with the DMRG

Table 5.1: Multi-orbital Hubbard parameters for the quantum dot chain

Parameter	Value (meV)
U	15.971
$J_{1/2}$	5.000
Δ	0.844
t	2.389
V	8.05

algorithm [34,35,35,135]. In this work, we used iTensor and a tool that we developed called Python MPS (PyMPS) to perform the DMRG calculations [136, 137].

Table 5.1 shows the multi-orbital Hubbard model parameters that were obtained from microscopic calculations [5]. An important feature of the multi-orbital Hubbard chain is the similarity of its low energy spectrum and the spectrum of a spin-1 chain. However, the similarity to the spin-1 chain spectrum is dependent on the choice of multi-orbital Hubbard parameters. This is evident with the example of a chain of two quantum dots. The spectrum of the two quantum dot array is shown in Fig. 5.3(a) where the parameters except for $J_{1/2}$ and t are taken from Table 5.1. While the Heisenberg spin-1 chain spectrum is reproduced with the parameters shown in Fig. 5.3(a), it is not reproduced when those parameters are changed as shown in Fig. 5.3(b). The dependence of the spectrum on parameters allows us to define a criterion for Heisenberg spin-1 chain behaviour. The criterion is such that when the multi-orbital Hubbard spectrum replicates the spin-1 chain spectrum as shown in Fig. 5.3(a), the criterion is satisfied, otherwise, as illustrated in Fig. 5.3(b) when the spectrum of the spin-1 chain is not replicated, the criterion is not satisfied. This principle applies to long arrays of quantum dots. For $L = 50$ quantum dots the $S^z = 0$ Hilbert space of the HK model at half-filling is $\binom{100}{50}^2 \approx 10^{58}$. For such a large Hilbert space we apply MPS-DMRG tools to obtain the low energy spectrum. Fig. 5.4(a) shows an example where a chain of 50 quantum dots satisfies the spin-1 chain criterion. This criterion applies to any size of quantum dot array and will be imperative to mapping out regions in parameter space where the system behaves as a chain of spin-1s.

The low energy spectrum of the long chain shown in Fig. 5.4(a) illustrates the

behaviour of two uncoupled spin-$\frac{1}{2}$ quasiparticles. While Fig. 5.3(a) shows that the two dot array resembles two spin-1s, Fig. 5.4(a) shows that the chain of many quantum dots resembles a chain of many spin-1 particles, which is understood in terms of two Haldane spin-$\frac{1}{2}$ quasiparticles at the edges. To illustrate the spectral gap, the spectrum of the multi-orbital Hubbard Hamiltonian as a function of system size shown in Fig. 5.4(b) was computed and compared with that of the Heisenberg spin-1 chain.

The spectrum of the Heisenberg spin-1 chain was computed using the Heisenberg Hamiltonian given by

$$H = J_1 \sum_i \mathbf{S}_i \cdot \mathbf{S}_{i+1} \tag{5.4}$$

where $J_1 = 2t^2 / \left(U + \frac{J_{1/2}}{2} - V\right)$ is the effective Heisenberg spin-1 coupling which is analytically obtained by treating the tunneling term in (5.3) as a perturbation [138].

We then added the term $g\mu B S^z_{\text{Total}}$ to (5.3) to study the behaviour of the quantum dot array as a function of applied magnetic field. Using a chain of 20 and 50 quantum dots, we determined the array size required for the singlet-triplet splitting in Figs. 5.5(a) and (b) to be small enough to avoid unwanted level crossings.

Finally, to determine the set of multi-orbital Hubbard parameters where the array gives a Heisenberg spin-1 chain like spectrum, we set the following criterion; if the spectrum consists of a singlet ground state, followed by a triplet first excited state, then followed by a quintuplet second excited state with no other states in between, then the criterion is satisfied.

Fig. 5.3 shows an example of a spectrum that satisfies the Heisenberg spin-1 criterion and another example that does not. In Fig. 5.3 (a), $t = \frac{1}{6}U$, which is still in the perturbative regime, while in Fig. 5.3 (b), $t \sim U$ thus the spin-1 description is no longer valid. Unlike the Heisenberg spin-1 chain spectrum, there are intermediate singlet and triplet states that appear below the quintuplet energy due to the coupling

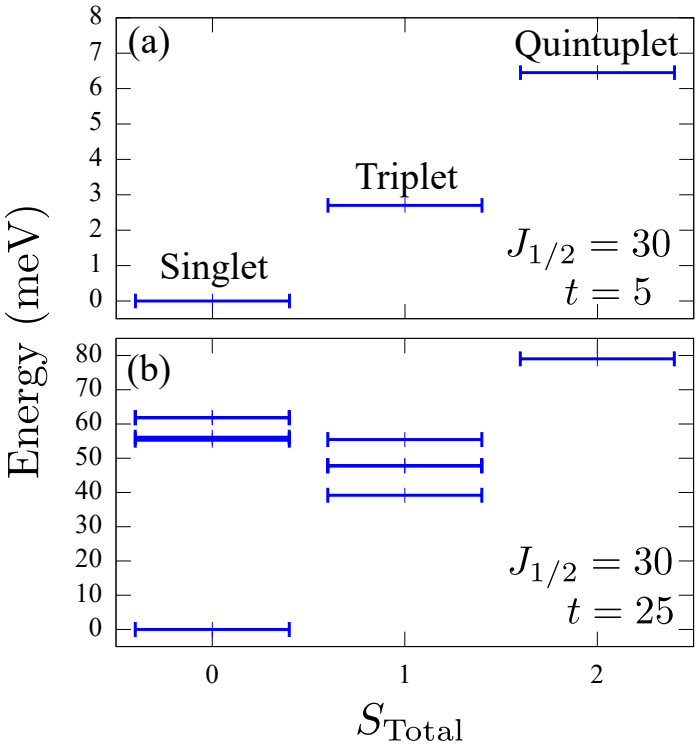

Figure 5.3: Low energy spectra of two quantum dots with two different sets of parameters. The spectrum (a) shows the spin-1 spectrum criterion satisfied, while (b) is an example where the criterion is not satisfied. All parameters are in meV.

of the ground state singlet and triplet to the higher energy configurations that contain triple electron occupation in a dot [5]. We then map out the regime in parameter space where this criterion is satisfied for a 16 quantum dot system.

5.5 Results

One of the ways to determine the spin-1 chain characteristics of the quantum dot array is to observe a quasidegenerate singlet-triplet ground state with a gap that separates the ground state from the quintuplet state in the low energy spectrum. Similar to the multi-orbital Hubbard spectrum for two quantum dots in Fig. 5.3(a), the spectrum of a chain of many dots in Fig. 5.4(a) also consists of a ground state singlet followed by triplet states and quintuplet states. The difference is that unlike the spectrum of two quantum dots, the singlet and triplet states in the spectrum of the large chain are almost degenerate with a splitting of 0.05 meV and are separated by a spectral gap from the quintuplet state. The almost degenerate singlet-triplet

states along with the spectral gap are indications of the existence of Haldane spin-$\frac{1}{2}$ quasiparticles at the edges. To demonstrate this point further, we show the energy of singlet and triplet states as a function of system size in 5.4(b). We see that singlet and triplet become almost degenerate while the singlet-quintuplet energy gap approaches a value of about 0.29 meV.

The same behaviour is observed in the spectrum of the Heisenberg spin-1 chain in Fig. 5.4(b) where the spectral gap is 0.45 meV. This spectral gap is known as the Haldane gap. Though the spectral gap for the multi-orbital Hubbard model is only about 65% of the spectral gap in the Heisenberg spin-1 chain spectrum, this level of agreement is to be expected considering the fact that the ground state of a two dot multi-orbital Hubbard model given these parameters is in about 70% agreement with the ground state of a two site Heisenberg spin-1 chain as seen in the overlap integral which was calculated in Ref. [5].

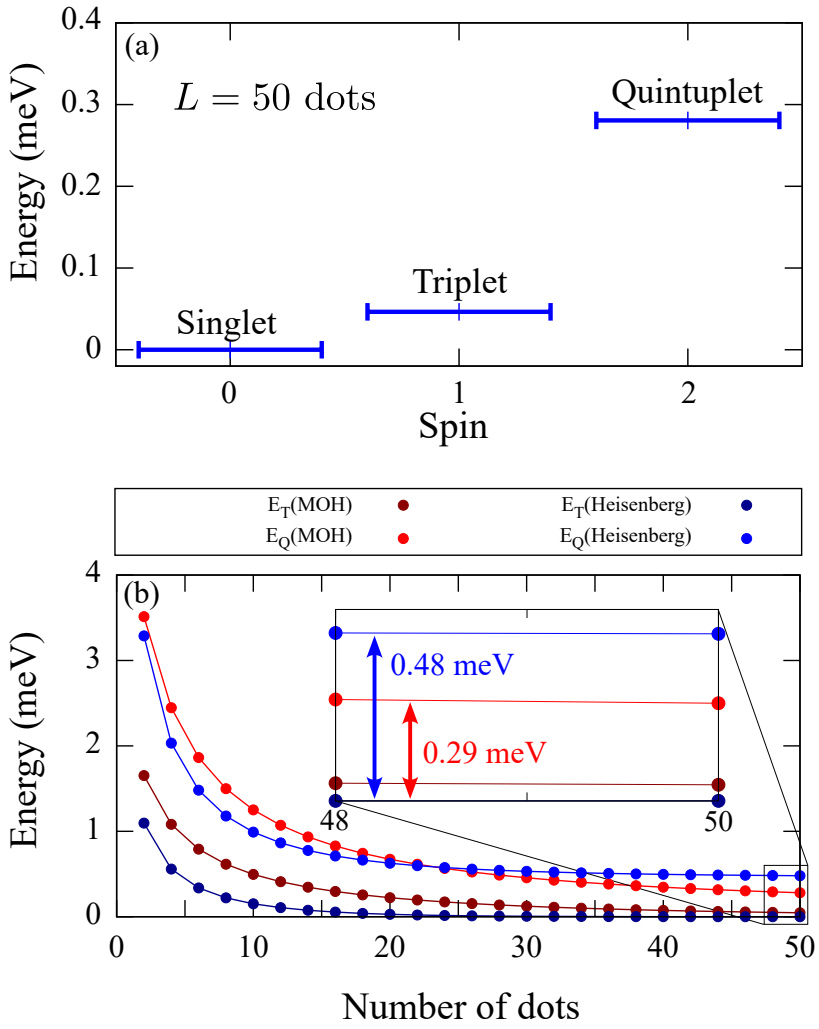

Figure 5.4: Parameters used are in Table 5.1. (a) Low energy spectrum of a chain of 50 quantum dots using the multi-orbital Hubbard model (MOH). (b) Low energy spectrum of a quantum dot array as a function of array size using various models. E_T and E_Q denote triplet and quintuplet energy respectively. All energies are shifted so that the singlet energy, which is not shown, is zero. The inset shows an enlarged section of the plot from $L = 48$ to 50 dots.

Next, we apply a magnetic field by adding Zeeman energy to demonstrate that the quantum dot array behaves the same way as two Haldane spin-$\frac{1}{2}$ quasiparticles would in a magnetic field and to also show that the $S^z = 0$ triplet and singlet can be isolated for use as a qubit basis. The spectra for 20 and 50 quantum dot arrays as a function of applied magnetic field are shown in Fig. 5.5.

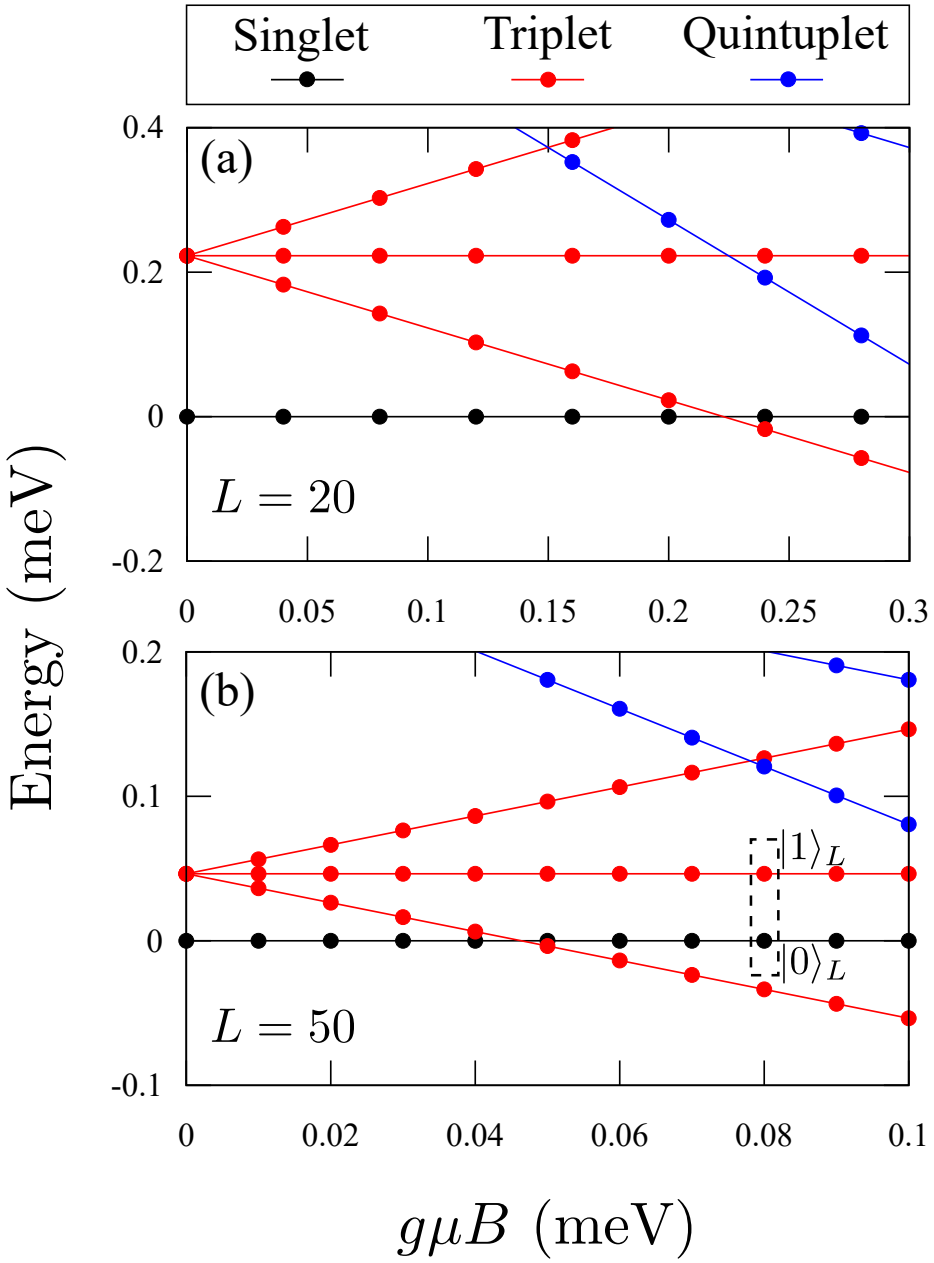

Figure 5.5: Multi-orbital Hubbard spectra as a function of magnetic field $g\mu B$ for $L = 20$ (a) and $L = 50$ (b) quantum dot arrays. The logical qubit states are highlighted in the dashed square.

In both the $L = 20$ and $L = 50$ cases, the Zeeman splitting between the triplet components increases as a function of magnetic field while the singlet remains unaffected, which is also the case for two coupled spin-$\frac{1}{2}$ particles. With the inclusion of the Zeeman splitting of the quintuplet components, this system behaves as a Hesienberg spin-1 chain would under a magnetic field.

For qubit operation, it is necessary for the $S^z = \pm 1$ triplet components to split

away far enough to isolate the $S^z = 0$ triplet and singlet before the $S^z = -2$ quinutplet crosses the $S^z = 0$ triplet. This does not happen with the $L = 20$ chain as seen in Fig. 5.5 (a) where at about $g\mu B = 0.24$ meV, the $S^z = -1$ triplet begins to cross below the singlet, but by then the lowest energy quintuplet already crossed below the $S^z = 0$ triplet. For the $L = 50$ chain, the singlet-triplet splitting at zero field is small enough such that isolation of the zero singlet and triplet occurs before any quintuplet crossing occurs. At about $g\mu B = 0.07$ meV as seen in Fig. 5.5 (b), the nonzero triplets isolate the qubit basis before the lowest energy quintuplet crosses even the $S^z = +1$ triplet. Since it is useful to have a larger spacing between the qubit basis and the nonzero triplets, we can use a magnetic field of 0.08 meV for qubit operation where the high energy triplet and the low energy quintuplet begin to cross.

It is also useful to construct a synthetic spin-1 chain with other parameters. These multi-orbital Hubbard parameters depend on the material, quantum dot As concentration, interdot distance and quantum dot size. Varying these parameters would vary the spectral gap since $J_1 \propto \frac{t^2}{U+\frac{J_{1/2}}{2}-V}$ [138], hence it is important to find which parameters would yield a synthetic spin-1 chain.

We map out regions in parameter space for 2 dot and 16 dot arrays where the Hamiltonian (5.3) produces a spin-1 chain spectrum, that is, regions where the spectrum consists of a singlet ground state, a triplet first excited state and a quintuplet second excited state. In both Figs. 5.6 and 5.7, there are clear regions in parameter space where a spin-1 spectrum is produced as opposed to random points sporadically dispersed. We decided to omit the parameter V from the diagrams because the term containing this factor only contributes a constant shift to the low energy spectrum due to all of the orbitals in these states having single occupation.

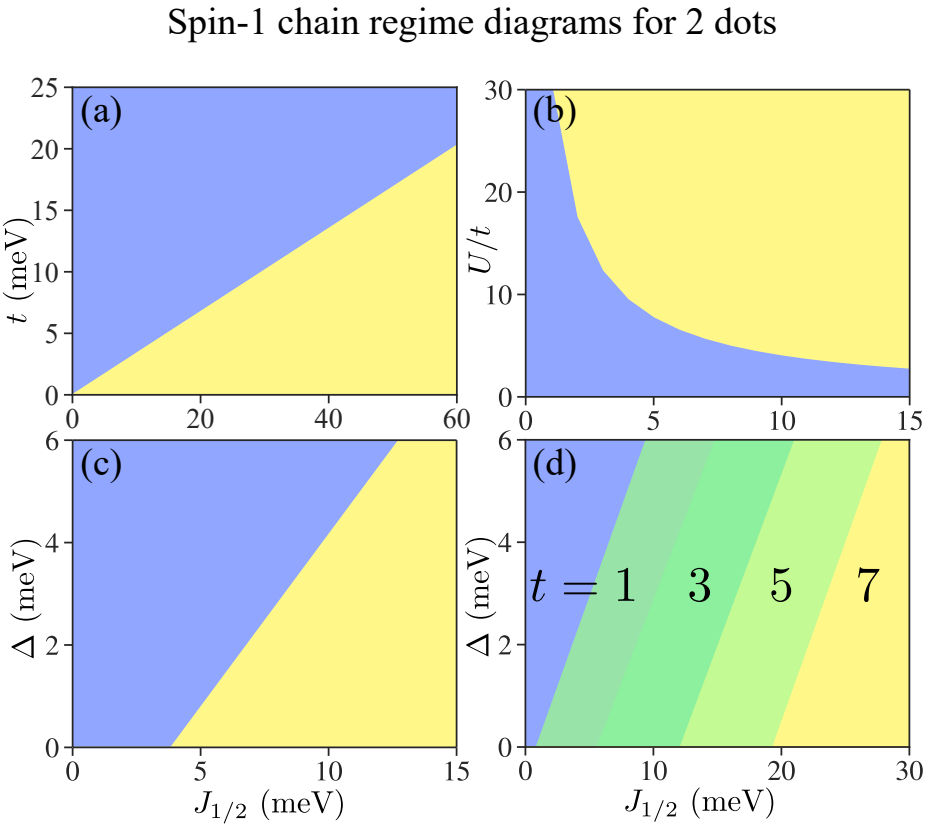

Figure 5.6: Spin-1 chain spectrum criterion as a function of various multi-orbital Hubbard parameters for an array of two quantum dots. Yellow (or green) region is where the criterion is satisfied and blue is otherwise. (a) is a diagram of t and $J_{1/2}$, (b) is a diagram of U/t and $J_{1/2}$, (c) shows Δ versus $J_{1/2}$ and (d) shows Δ versus $J_{1/2}$ at different values of t, where the all values of t are in units of meV.

In Fig. 5.6(a) we see a t varying linearly with $J_{1/2}$ at the boundary. Moreover, Fig. 5.6(b) shows a $\frac{1}{J_{1/2}}$ dependence of U at the boundary, which is expected because of the linear dependence of t on $J_{1/2}$ at the boundary in Fig. 5.6(a). In Fig. 5.6(c), we see a linear dependence between Δ and J at the boundary. Furthermore, varying t at different cross sections of the Δ-$J_{1/2}$ plane as shown in Fig. 5.6(d), does not vary the slope of the boundary. However, the $J_{1/2}$-intercept increases with t.

Since the singlet-triplet qubit requires large chains, we also map out regions in parameter space where a spin-1 chain spectrum is produced for a 16 dot system in Fig. 5.7. Similar trends to the 2 dot diagrams are seen in the 16 dot diagrams. For instance, linear dependence of t on $J_{1/2}$ at the boundary where the spin-1 chain criterion is satisfied is shown in Fig. 5.7(a). The $\frac{1}{J_{1/2}}$ dependence in Fig. 5.7(b) is also seen as well as the linear dependence of Δ on $J_{1/2}$ in Fig. 5.7(c).

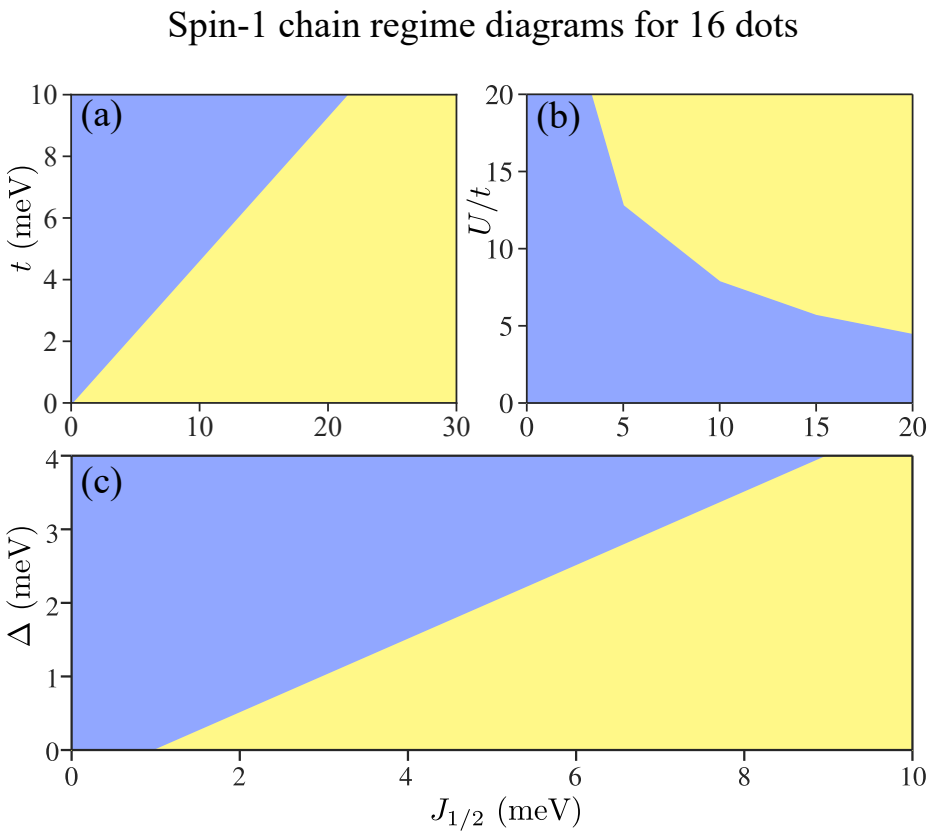

Figure 5.7: Spin-1 spectrum criterion as a function of various multi-orbital Hubbard parameters for an array of 16 quantum dots. Yellow region is where the criterion is satisfied and blue is otherwise. All parameters are the same as the ones used in Figs. 5.4 and 5.5 except for those that are varied.

The two lowest energy eigenstates for a single quantum dot with two electrons in the p-shell are a triplet ground state and a singlet first excited state separated by an energy $E_{s1} = \frac{3J_{1/2} - \sqrt{J_{1/2}^2 + (4\Delta)^2}}{4}$ [5]. If another quantum dot is placed beside the first one, the orbitals in different dots are coupled by the hopping term $tc_{i\alpha}^{\dagger} c_{i+1\alpha}$. We see the effect of hopping in the spectrum of 4 electrons on two quantum dots in the splitting of the singlet and triplet double quantum dot states, where in this case, the singlet is the ground state and the first excited state is a triplet. In the regime where the hopping term in (5.3) is weak, the singlet triplet splitting is proportional to the effective Heisenberg spin-1 coupling $J_1 = 2t^2/\left(U + J_{1/2}/2 - V\right)$. This introduces the condition $J_1 < E_{s1}$ which can be interpreted as the values of t which conserve the spin-1 character of each quantum dot in the array. This condition can shed light on Figs. 5.6 and 5.7.

Increasing $J_{1/2}$ increases the singlet-triplet splitting for a single quantum dot,

protecting the spin-1 character of each dot against perturbations according to the analytic expression of E_{s1}. This behavior is observed in Figs. 5.6 and 5.7, where the Haldane phase is favored whenever $J_{1/2}$ is increased. On the other hand, an increase in the hopping energy t mixes the single quantum dot ground and excited states, destabilizing Haldane phase , which is also observed in Figs. 5.6(a) and 5.7(a). Similarly, increasing the p-shell splitting Δ decreases the singlet-triplet gap in a single quantum dot, eventually producing a ground state that is a singlet instead of a triplet in the case when $E_{s1} < 0$, losing the spin-1 behavior of each quantum dot.

In Figs. 5.6(c) and 5.7(d) the competition between $J_{1/2}$ and Δ terms can be seen directly. Particularly, in Fig. 5.6(d) the combined effect of varying Δ with the hopping term t and $J_{1/2}$ is shown. When the hopping energy t is increased, $J_{1/2}$ must also increase even for negligible Δ in order to stabilize the Haldane phase. This is the reason behind the increasing of the $J_{1/2}$-intercept as t increases.

5.6 Conclusion

We presented here the steps enabling the microscopic design of a topologically protected singlet-triplet qubit in an InAsP quantum dot array embedded in an InP nanowire. The multi-orbital Hubbard model derived from microscopic calculations is used to describe the singlet-triplet qubit. A degenerate singlet-triplet ground state followed by a spectral gap separating the ground state from the quintuplet state is observed in the low energy spectrum of the multi-orbital Hubbard chain. This same behaviour which is also observed in the spectrum of a Heisenberg spin-1 chain indicates the existence of spin-$\frac{1}{2}$ quasiparticles at the edges of the chain. Further indication of the existence of spin-$\frac{1}{2}$ quasiparticles is the behaviour of the low energy spectrum as a function of applied magnetic field. Despite the system being a chain of synthetic spin-1s constructed using an InAsP quantum dot array, the magnetic field dependence of the spectrum is the same as that of two spin-$\frac{1}{2}$ quasiparticles. The external magnetic field also allows the $S^z = 0$ triplet and singlet states to serve as the qubit basis by isolating those states from the other $S^z = \pm 1$ components of the

triplet and the quintuplet states. For the design of the qubit, the regions in parameter space where the low energy spectrum of the Heisenberg spin-1 chain is reproduced with the multi-orbital Hubbard model are mapped. The finite spectral gap gives the qubit potential to be robust against perturbations.

Acknowledgements

J.M., D.M. and P.H. acknowledges support from NSERC Discovery and Strategic QC2DM Project Grants and Compute Canada for computing resources.

Chapter 6

Conclusions

Using microscopic computational techniques such as TB and CI, the electronic and excitonic spectrum of an InAsP nanowire quantum dot embedded in an InP nanowire was computed. The ordering of the emission lines was found to be consistent with the measured spectra of actual InAsP quantum dot nanowires. Furthermore, by introducing inhomogeneity to the As distribution in the quantum dots, we were able to generate emission spectra of vastly different orderings of excitonic peaks from those of quantum dots with a uniform random distribution of As, demonstrating the ability to control the emission spectra by the As composition in the quantum dots. This control enables the design of single and entangled photon sources since single photons are generated from exciton recombination and entangled photons are generated from biexciton-exciton cascade from quantum dots where the exciton and biexciton peaks are degenerate.

The same computational techniques were then applied to study the electronic and magnetic properties of one and two InAsP quantum dots embedded in an InP nanowire to demonstrate the possibility of constructing a synthetic spin-1 chain using an array of such quantum dots in a nanowire. Through the analysis of the Coulomb blockade spectrum, it was determined that one quantum dot with a half-filled p-shell has a spin-1 ground state and that two quantum dots with a half-filled p-shell exhibit the same low energy spectrum as two coupled spin-1 particles. The magnetic properties of one and two spin-1 particles that were observed in the single and double

quantum dot systems respectively allow for the possibility to construct a synthetic spin-1 chain with an array of these quantum dots and therefore to construct a topologically protected singlet-triplet qubit.

Long arrays of InAsP quantum dots were then simulated using the more abstract microscopic multi-orbital Hubbard model with parameters obtained from microscopic calculations. To address the long chain of the multi-orbital Hubbard model, the MPS DMRG tool was developed. For a long chain, it was shown that the ground state was separated from a finite energy gap from the excited states, which is indication that the ground state is topologically protected from the excited states as is the case with a long chain of spin-1 particles. Furthermore, the behaviour of the quantum dot chain as a function of an external magnetic field was shown to be the same as two spin-1/2 particles at the edges of the chain, which is further indication that the system is in a topological phase. The applied magnetic field also isolates the $S^z = 0$ singlet and triplet states from the rest of the spectrum, allowing for qubit operation. Finally, the regions in the multi-orbital Hubbard parameter space where such spectra are reproduced were mapped, allowing for the design and engineering of a topologically protected singlet-triplet qubit.

Since unexpected clustering of As atoms occurs naturally in the growth process of these quantum dots, the incorporation of lattice dynamics would provide a better theoretical understanding of the many-body properties of the quantum dot and hence more accurate calculations of the excitonic spectra. The effect of lattice vibrations on the stability of the spin-1 behaviour of the quantum dot is still to be determined.

Another issue with these InAsP quantum dots is that when two of the dots are close to each other, i.e. for a two dot array, the effective Heisenberg spin-1 coupling constant is much lower than room temperature at about 1 meV. Improving the coupling constant involves finding a way to increase t with respect to U. Some of the more obvious ways of attempting this would be to increase the physical parameters such as the size of each quantum dot and the interdot distance. Another possibility is to use a different material all together such as an array of Moiré quantum dots from

twisted layers of transition metal dichalcogenides (TMD) [139].

Though not necessary for the construction of a singlet-triplet qubit, more rigorous methods to classify the topological Haldane phase of the quantum dot array would be beneficial. One such method could be to observe a quantity known as the spin-string correlation $\langle S_0^z \prod_i^{n-1} \exp[i\pi S_i^z] S_n^z \rangle$ [140] which unlike the familiar spin correlation $\langle S_0^z S_n^z \rangle$, does not necessarily decay with distance n. In fact, the conjecture proposed by Girvin and Arovas is that if the spin-string correlation does not decay, but the spin correlation does, then the system has a finite spectral gap which, for the synthetic spin-1 chain, would imply that the ground state is in the topological Haldane phase [140].

Bibliography

[1] M. Ciorga, A.S. Sachrajda, P. Hawrylak, C. Gould, P. Zawadzki, Y. Feng, and Z. Wasilewski. Readout of a single electron spin based quantum bit by current detection. *Physica E: Low-dimensional Systems and Nanostructures*, 11(1):35–40, 2001.

[2] Daniel Loss and David P. DiVincenzo. Quantum computation with quantum dots. *Phys. Rev. A*, 57:120–126, Jan 1998.

[3] Patrick Laferrière, Edith Yeung, Marek Korkusinski, Philip J. Poole, Robin L. Williams, Dan Dalacu, Jacob Manalo, Moritz Cygorek, Abdulmenaf Altintas, and Pawel Hawrylak. Systematic study of the emission spectra of nanowire quantum dots. *Applied Physics Letters*, 118(16):161107, 2021.

[4] Moritz Cygorek, Marek Korkusinski, and Pawel Hawrylak. Atomistic theory of electronic and optical properties of inasp/inp nanowire quantum dots. *Phys. Rev. B*, 101:075307, Feb 2020.

[5] Jacob Manalo, Moritz Cygorek, Abdulmenaf Altintas, and Pawel Hawrylak. Electronic and magnetic properties of many-electron complexes in charged InA_xP_{1-x} quantum dots in inp nanowires. *Phys. Rev. B*, 104:125402, Sep 2021.

[6] Sofiane Haffouz, Katharina D. Zeuner, Dan Dalacu, Philip J. Poole, Jean Lapointe, Daniel Poitras, Khaled Mnaymneh, Xiaohua Wu, Martin Couillard, Marek Korkusinski, Eva Schöll, Klaus D. Jöns, Valery Zwiller, and Robin L. Williams. Bright single inasp quantum dots at telecom wavelengths in position-

controlled inp nanowires: The role of the photonic waveguide. *Nano Letters*, 18(5):3047–3052, May 2018.

[7] Andrew J. Shields. Semiconductor quantum light sources. *Nature Photonics*, 1(4):215–223, Apr 2007.

[8] D. Dalacu, S. Frédérick, D. Kim, M. E. Reimer, J. Lapointe, P. J. Poole, G. C. Aers, R. L. Williams, W. R. McKinnon, M. Korkusi'nski, and P. Hawrylak. Directed self-assembly of single quantum dots for telecommunication wavelength optical devices. *Laser & Photon. Rev.*, 4(2):283–299, 2010.

[9] M Korkusinski, P Hawrylak, A Babinski, M Potemski, S Raymond, and Z Wasilewski. Optical readout of charge and spin in a self-assembled quantum dot in a strong magnetic field. *Europhysics Letters (EPL)*, 79(4):47005, jul 2007.

[10] Chang-Yu Hsieh, Yun-Pil Shim, Marek Korkusinski, and Pawel Hawrylak. Physics of lateral triple quantum-dot molecules with controlled electron numbers. *Reports on Progress in Physics*, 75(11):114501, oct 2012.

[11] Dan Dalacu, Khaled Mnaymneh, Xiaohua Wu, Jean Lapointe, Geof C. Aers, Philip J. Poole, and Robin L. Williams. Selective-area vapor-liquid-solid growth of tunable inasp quantum dots in nanowires. *Applied Physics Letters*, 98(25):251101, 2011.

[12] Dan Dalacu, Khaled Mnaymneh, Jean Lapointe, Xiaohua Wu, Philip J. Poole, Gabriele Bulgarini, Val Zwiller, and Michael E. Reimer. Ultraclean emission from inasp quantum dots in defect-free wurtzite inp nanowires. *Nano Letters*, 12(11):5919–5923, 2012. PMID: 23066839.

[13] O. Benson, C. Santori, M. Pelton, and Y. Yamamoto. Regulated and entangled photons from a single quantum dot. *Phys. Rev. Lett.*, 84:2513–2516, 2000.

[14] N. Akopian, N. H. Lindner, E. Poem, Y. Berlatzky, J. Avron, D. Gershoni, B. D. Gerardot, and P. M. Petroff. Entangled photon pairs from semiconductor quantum dots. *Phys. Rev. Lett.*, 96:130501, 2006.

[15] Blazej Jaworowski, Nick Rogers, Marek Grabowski, and Pawel Hawrylak. Macroscopic singlet-triplet qubit in synthetic spin-one chain in semiconductor nanowires. *Scientific Reports*, 7(1):5529, Jul 2017.

[16] Błażej Jaworowski and Paweł Hawrylak. Quantum bits with macroscopic topologically protected states in semiconductor devices. *Applied Sciences*, 9(3), 2019.

[17] F. Duncan M. Haldane. Nobel lecture: Topological quantum matter. *Rev. Mod. Phys.*, 89:040502, Oct 2017.

[18] Ian Affleck, Tom Kennedy, Elliott H. Lieb, and Hal Tasaki. Rigorous results on valence-bond ground states in antiferromagnets. *Phys. Rev. Lett.*, 59:799–802, Aug 1987.

[19] M. W. Johnson, M. H. S. Amin, S. Gildert, T. Lanting, F. Hamze, N. Dickson, R. Harris, A. J. Berkley, J. Johansson, P. Bunyk, E. M. Chapple, C. Enderud, J. P. Hilton, K. Karimi, E. Ladizinsky, N. Ladizinsky, T. Oh, I. Perminov, C. Rich, M. C. Thom, E. Tolkacheva, C. J. S. Truncik, S. Uchaikin, J. Wang, B. Wilson, and G. Rose. Quantum annealing with manufactured spins. *Nature*, 473(7346):194–198, May 2011.

[20] Jay M. Gambetta, Jerry M. Chow, and Matthias Steffen. Building logical qubits in a superconducting quantum computing system. *npj Quantum Information*, 3(1):2, Jan 2017.

[21] Frank Arute, Kunal Arya, Ryan Babbush, Dave Bacon, Joseph C. Bardin, Rami Barends, Rupak Biswas, Sergio Boixo, Fernando G. S. L. Brandao, David A. Buell, Brian Burkett, Yu Chen, Zijun Chen, Ben Chiaro, Roberto Collins,

John M. Martinis, et al. Quantum supremacy using a programmable superconducting processor. *Nature*, 574(7779):505–510, Oct 2019.

[22] E. Knill, R. Laflamme, and G. J. Milburn. A scheme for efficient quantum computation with linear optics. *Nature*, 409(6816):46–52, Jan 2001.

[23] Lars S. Madsen, Fabian Laudenbach, Mohsen Falamarzi. Askarani, Fabien Rortais, Trevor Vincent, Jacob F. F. Bulmer, Filippo M. Miatto, Leonhard Neuhaus, Lukas G. Helt, Matthew J. Collins, Adriana E. Lita, Thomas Gerrits, Sae Woo Nam, Varun D. Vaidya, Matteo Menotti, Ish Dhand, Zachary Vernon, Nicolás Quesada, and Jonathan Lavoie. Quantum computational advantage with a programmable photonic processor. *Nature*, 606(7912):75–81, Jun 2022.

[24] Pieter Kok, W. J. Munro, Kae Nemoto, T. C. Ralph, Jonathan P. Dowling, and G. J. Milburn. Linear optical quantum computing with photonic qubits. *Rev. Mod. Phys.*, 79:135–174, Jan 2007.

[25] K. Wright, K. M. Beck, S. Debnath, J. M. Amini, Y. Nam, N. Grzesiak, J.-S. Chen, N. C. Pisenti, M. Chmielewski, C. Collins, K. M. Hudek, J. Mizrahi, J. D. Wong-Campos, S. Allen, J. Kim, et al. Benchmarking an 11-qubit quantum computer. *Nature Communications*, 10(1):5464, Nov 2019.

[26] I. Pogorelov, T. Feldker, Ch. D. Marciniak, L. Postler, G. Jacob, O. Krieglsteiner, V. Podlesnic, M. Meth, V. Negnevitsky, M. Stadler, B. Höfer, C. Wächter, K. Lakhmanskiy, R. Blatt, P. Schindler, and T. Monz. Compact ion-trap quantum computing demonstrator. *PRX Quantum*, 2:020343, Jun 2021.

[27] M. Zieliński, M. Korkusiński, and P. Hawrylak. Atomistic tight-binding theory of multiexciton complexes in a self-assembled inas quantum dot. *Phys. Rev. B*, 81:085301, Feb 2010.

[28] Marek Korkusinski. *Atomistic Simulations of Electronic and Optical Properties of Semiconductor Nanostructures*, pages 149–216. Springer International Publishing, Cham, 2015.

[29] Marek Korkusinski, Oleksandr Voznyy, and Pawel Hawrylak. Fine structure and size dependence of exciton and biexciton optical spectra in cdse nanocrystals. *Phys. Rev. B*, 82:245304, Dec 2010.

[30] P. N. Keating. Effect of invariance requirements on the elastic strain energy of crystals with application to the diamond structure. *Phys. Rev.*, 145:637–645, May 1966.

[31] Jean-Marc Jancu, Reinhard Scholz, Fabio Beltram, and Franco Bassani. Empirical spds* tight-binding calculation for cubic semiconductors: General method and material parameters. *Phys. Rev. B*, 57:6493–6507, Mar 1998.

[32] Timothy B. Boykin, Gerhard Klimeck, R. Chris Bowen, and Fabiano Oyafuso. Diagonal parameter shifts due to nearest-neighbor displacements in empirical tight-binding theory. *Phys. Rev. B*, 66:125207, Sep 2002.

[33] Dan Dalacu, David B. Northeast, Philip J. Poole, Geof C. Aers, Robin L. Williams, Kim A. Owen, and Daniel Oblak. Pump power control of photon statistics in a nanowire quantum dot. *Phys. Rev. B*, 102:115401, Sep 2020.

[34] Steven R. White. Density matrix formulation for quantum renormalization groups. *Phys. Rev. Lett.*, 69:2863–2866, Nov 1992.

[35] U. Schollwöck. The density-matrix renormalization group. *Rev. Mod. Phys.*, 77:259–315, Apr 2005.

[36] Ulrich Schollwöck. The density-matrix renormalization group in the age of matrix product states. *Annals of Physics*, 326(1):96–192, 2011. January 2011 Special Issue.

[37] M B Hastings. An area law for one-dimensional quantum systems. *Journal of Statistical Mechanics: Theory and Experiment*, 2007(08):P08024–P08024, aug 2007.

[38] Matthew B. Hastings and Tohru Koma. Spectral gap and exponential decay of correlations. *Communications in Mathematical Physics*, 265(3):781–804, Aug 2006.

[39] J. Eisert, M. Cramer, and M. B. Plenio. Colloquium: Area laws for the entanglement entropy. *Rev. Mod. Phys.*, 82:277–306, Feb 2010.

[40] Johannes Hauschild and Frank Pollmann. Efficient numerical simulations with Tensor Networks: Tensor Network Python (TeNPy). *SciPost Phys. Lect. Notes*, page 5, 2018.

[41] G. W. Stewart. On the early history of the singular value decomposition. *SIAM Review*, 35(4):551–566, 1993.

[42] C. Hubig, I. P. McCulloch, and U. Schollwöck. Generic construction of efficient matrix product operators. *Phys. Rev. B*, 95:035129, Jan 2017.

[43] Garnet Kin-Lic Chan, Anna Keselman, Naoki Nakatani, Zhendong Li, and Steven R. White. Matrix product operators, matrix product states, and ab initio density matrix renormalization group algorithms. *The Journal of Chemical Physics*, 145(1):014102, 2016.

[44] E.M. Stoudenmire and Steven R. White. Studying two-dimensional systems with the density matrix renormalization group. *Annual Review of Condensed Matter Physics*, 3(1):111–128, 2012.

[45] Gonzalo Alvarez. Implementation of the su(2) hamiltonian symmetry for the dmrg algorithm. *Computer Physics Communications*, 183(10):2226–2232, 2012.

[46] M. Bayer, O. Stern, P. Hawrylak, S. Fafard, and A. Forchel. Hidden symmetries in the energy levels of excitonic artificial atoms. *Nature*, 405:923–926, 2000.

[47] David Fattal, Kyo Inoue, Jelena Vučković, Charles Santori, Glenn S. Solomon, and Yoshihisa Yamamoto. Entanglement formation and violation of Bell's inequality with a semiconductor single photon source. *Phys. Rev. Lett.*, 92:037903, 2004.

[48] I. Schwartz, D. Cogan, E. R. Schmidgall, Y. Don, L. Gantz, O. Kenneth, N. H. Lindner, and D. Gershoni. Deterministic generation of a cluster state of entangled photons. *Science*, 354:6311, 2016.

[49] M. Bayer, G. Ortner, O. Stern, A. Kuther, A. A. Gorbunov, A. Forchel, P. Hawrylak, S. Fafard, K. Hinzer, T. L. Reinecke, S. N. Walck, J. P. Reithmaier, F. Klopf, and F. Schäfer. Fine structure of neutral and charged excitons in self-assembled In(Ga)As/(Al)GaAs quantum dots. *Phys. Rev. B*, 65:195315, 2002.

[50] M. Zieliński. Fine structure of light-hole excitons in nanowire quantum dots. *Phys. Rev. B*, 88:115424, 2013.

[51] M. Korkusinski and P. Hawrylak. Atomistic theory of emission from dark excitons in self-assembled quantum dots. *Phys. Rev. B*, 87:115310, 2013.

[52] Eugene Kadantsev and Pawel Hawrylak. Theory of exciton fine structure in semiconductor quantum dots: Quantum dot anisotropy and lateral electric field. *Phys. Rev. B*, 81:045311, 2010.

[53] Anna H. Trojnar, Eugene S. Kadantsev, Marek Korkusiński, and Pawel Hawrylak. Theory of fine structure of correlated exciton states in self-assembled semiconductor quantum dots in a magnetic field. *Phys. Rev. B*, 84:245314, 2011.

[54] Moritz Cygorek, Marek Korkusinski, and Pawel Hawrylak. Atomistic theory of electronic and optical properties of InAsP/InP nanowire quantum dots. *Phys. Rev. B*, 101:075307, 2020.

[55] R. Singh and G. Bester. Nanowire quantum dots as an ideal source of entangled photon pairs. *Phys. Rev. Lett.*, 103:063601, 2009.

[56] Takashi Kuroda, Takaaki Mano, Neul Ha, Hideaki Nakajima, Hidekazu Kumano, Bernhard Urbaszek, Masafumi Jo, Marco Abbarchi, Yoshiki Sakuma, Kazuaki Sakoda, Ikuo Suemune, Xavier Marie, and Thierry Amand. Symmetric quantum dots as efficient sources of highly entangled photons: Violation of Bell's inequality without spectral and temporal filtering. *Phys. Rev. B*, 88:041306(R), 2013.

[57] T. Seidelmann, F. Ungar, M. Cygorek, A. Vagov, A. M. Barth, T. Kuhn, , and V. M. Axt. From strong to weak temperature dependence of the two-photon entanglement resulting from the biexciton cascade inside a cavity. *Phys. Rev. B*, 99:245301, 2019.

[58] Marek Korkusinski, Michael E. Reimer, Robin L. Williams, and Pawel Hawrylak. Engineering photon cascades from multiexciton complexes in a self-assembled quantum dot by a lateral electric field. *Phys. Rev. B*, 79:035309, 2009.

[59] M. E. Reimer, M. P. van Kouwen, A. W. Hidma, M. H. M. van Weert, E. P. A. M. Bakkers, L. P. Kouwenhoven, and V. Zwiller. Electric field induced removal of the biexciton binding energy in a single quantum dot. *Nano Lett.*, 11:645–650, 2010.

[60] Mohd Zeeshan, Nachiket Sherlekar, Arash Ahmadi, Robin L Williams, and Michael E Reimer. Proposed scheme to generate bright entangled photon pairs by application of a quadrupole field to a single quantum dot. *Phys. Rev. Lett.*, 122:227401, 2019.

[61] T. Heindel, A. Thoma, M. von Helversen, M. Schmidt, A. Schlehahn, M. Gschrey, P. Schnauber, J-H. Schulze, A. Strittmatter, J. Beyer, S. Rodt, A. Carmele, A. Knorr, and S. Reitzenstein. A bright triggered twin-photon source in the solid state. *Nat. Commun.*, 8:14870, 2017.

[62] J. Claudon, J. Bleuse, N. S. Malik, M. Bazin, P. Jaffrennou, N. Gregersen, C. Sauvan, P. Lalanne, and J.-M. Gérard. A highly efficient single-photon source based on a quantum dot in a photonic nanowire. *Nat. Photon.*, 4:174, 2010.

[63] M. E. Reimer, G. Bulgarini, N. Akopian, M. Hocevar, M. Bouwes Bavinck, M. A. Verheijen, E. P. A. M. Bakkers, L. P. Kouwenhoven, and V. Zwiller. Bright single-photon sources in bottom-up tailored nanowires. *Nat. Commun.*, 3:737, 2012.

[64] D. Dalacu, K. Mnaymneh, J. Lapointe, X. Wu, P. J. Poole, G. Bulgarini, V. Zwiller, and M. E. Reimer. Ultraclean emission from InAsP quantum dots in defect-free wurtzite InP nanowires. *Nano Lett.*, 12:5919–5923, 2012.

[65] M. A. M. Versteegh, M. E. Reimer, K. D. Jöns, D. Dalacu, P.J. Poole, A. Gulinatti, A. Giudice, and V. Zwiller. Observation of strongly entangled photon pairs from a nanowire quantum dot. *Nat. Commun.*, 5:6298, 2014.

[66] D. Dalacu, K. Mnaymneh, X. Wu, J. Lapointe, G. C. Aers, P. J. Poole, and R. L. Williams. Selective-area vapor-liquid-sold growth of tunable inasp quantum dots in nanowires. *Appl. Phys. Lett.*, 98:251101, 2011.

[67] Dan Dalacu, Philip J. Poole, and Robin L. Williams. Nanowire-based sources of non-classical light. *Nanotechnology*, 30:232001, 2019.

[68] K. A. Dick, J. Bolinsson, M. E. Messing, S. Lehmann, J. Johansson, and P. Caroff. Parameter space mapping of InAs nanowire cyrstal structure. *J. Vac. Sci. Technol. B*, 29:04D103, 2011.

[69] L. E. Fröberg, B. A. Wacaser, J. B. Wagner, S. Jeppesen, B. J. Ohlsson, K. Deppert, and L. Samuelson. Transients in the formation of nanowire heterostructures. *Nano Lett.*, 8:3815–3818, 2008.

[70] S. Haffouz, P. J. Poole, J. Jin, X. Wu, L. Giner, K. Mnaymneh, D. Dalacu, and R. L. Williams. Single quantum dot-in-a-rod embedded in a photonic nanowire waveguide for telecom band emission. *Applied Physics Letters*, 117:113102, 2020.

[71] M. E. Reimer, G. Bulgarini, A. Fognini, R. W. Heeres, B. J. Witek, M. A. M. Versteegh, A. Rubino, T. Braun, M. Kamp, S. Höfling, D. Dalacu, J. Lapointe, P. J. Poole, and V. Zwiller. Overcoming power broadening of the quantum dot emission in a pure wurtzite nanowire. *Phys. Rev. B*, 93:195316, 2016.

[72] A. Fognini, A. Ahmadi, M. Zeeshan, J. T. Fokkens, S. J. Gibson, N. Sherlekar, S. J. Daley, D. Dalacu, P. J. Poole, K. D. Jöns, V. Zwiller, , and M. E. Reimer. Dephasing free photon entanglement with a quantum dot. *ACS Photonics*, 6:1656, 2019.

[73] A. Kiraz, S. Fälth, C. Becher, B. Gayral, W. V. Schoenfeld, P. M. Petroff, Lidong Zhang, E. Hu, and A. Imamoglŭ. Photon correlation spectroscopy of a single quantum dot. *Phys. Rev. B*, 65:161303(R), 2002.

[74] Charles Santori, David Fattal, Jelena Vuckovic, Glenn S Solomon, Edo Waks, and Yoshihisa Yamamoto. Submicrosecond correlations in photoluminescence from InAs quantum dots. *Phys. Rev. B*, 69:205324, 2004.

[75] G. Sallen, A. Tribu, T. Aichele, R. André, L. Besombes, C. Bougerol, S. Tatarenko, K. Kheng, , and J. Ph. Poizat. Exciton dynamics of a single quantum dot embedded in a nanowire. *Phys. Rev. B*, 80:085310, 2009.

[76] G. Sallen, A. Tribu, T. Aichele, R. André, L. Besombes, C. Bougerol, S. Tatarenko, K. Kheng, , and J. Ph. Poizat. Photon correlation studies of charge variation in a single GaAlAs quantum dot. *Phys. Rev. B*, 87:035310, 2013.

[77] E. Moreau, I. Robert, L. Manin, V. Thierry-Mieg, J. M. Gérard, and I. Abram. Quantum cascade of photons in semiconductor quantum dots. *Phys. Rev. Lett.*, 87:183601, 2001.

[78] D. V. Regelman, U. Mizrahi, D. Gershoni, E. Ehrenfreund, W. V. Schoenfeld, and P. M. Petroff. Semiconductor quantum dot: A quantum light source of multicolor photons with tunable statistics. *Phys. Rev. Lett.*, 87:257401, 2001.

[79] W. Sheng and P. Hawrylak. Atomistic theory of electronic and optical properties of InAs/InP self-assembled quantum dots on patterned substrates. *Phys. Rev. B*, 75:035326, 2005.

[80] M. Zieliński, M. Korkusinski, and P. Hawrylak. Atomistic tight-binding theory of multiexciton complexes in a self-assembled InAs quantum dot. *Phys. Rev. B*, 81:085301, 2010.

[81] Garnett Bryant. Electronic structure of ultrasmall quantum-well boxes. *Phys. Rev. Lett.*, 59:1140, Sept 1987.

[82] Pawel Hawrylak. Single-electron capacitance spectroscopy of few-electron artificial atoms in a magnetic field: Theory and experiment. *Phys. Rev. Lett.*, 71:3347–3350, Nov 1993.

[83] Raymond Ashoori. Electrons in artificial atoms. *Nature*, 379:413–419, 1996.

[84] José A. Brum and Pawel Hawrylak. Coupled quantum dots as quantum exclusive-or gate. *Superlattices and Microstructures*, 22(3):431–436, 1997.

[85] S. Tarucha, D. G. Austing, T. Honda, R. J. van der Hage, and L. P. Kouwenhoven. Shell filling and spin effects in a few electron quantum dot. *Phys. Rev. Lett.*, 77:3613–3616, Oct 1996.

[86] M. Ciorga, A. S. Sachrajda, P. Hawrylak, C. Gould, P. Zawadzki, S. Jullian, Y. Feng, and Z. Wasilewski. Addition spectrum of a lateral dot from coulomb and spin-blockade spectroscopy. *Phys. Rev. B*, 61:R16315–R16318, Jun 2000.

[87] R. Hanson, L. P. Kouwenhoven, J. R. Petta, S. Tarucha, and L. M. K. Vandersypen. Spins in few-electron quantum dots. *Rev. Mod. Phys.*, 79:1217–1265, Oct 2007.

[88] Anderson West, Bas Hensen, Alexis Jouan, Tuomo Tanttu, Chih-Hwan Yang, Alessandro Rossi, M. Fernando Gonzalez-Zalba, Fay Hudson, Andrea Morello, David J. Reilly, and Andrew S. Dzurak. Gate-based single-shot readout of spins in silicon. *Nature Nanotechnology*, 14(5):437–441, May 2019.

[89] Florian Meier, Jeremy Levy, and Daniel Loss. Quantum computing with spin cluster qubits. *Phys. Rev. Lett.*, 90:047901, Jan 2003.

[90] E. Kawakami, P. Scarlino, D. R. Ward, F. R. Braakman, D. E. Savage, M. G. Lagally, Mark Friesen, S. N. Coppersmith, M. A. Eriksson, and L. M. K. Vandersypen. Electrical control of a long-lived spin qubit in a si/sige quantum dot. *Nature Nanotechnology*, 9(9):666–670, Sep 2014.

[91] Dan Cogan, Oded Kenneth, Netanel H. Lindner, Giora Peniakov, Caspar Hopfmann, Dan Dalacu, Philip J. Poole, Pawel Hawrylak, and David Gershoni. Depolarization of electronic spin qubits confined in semiconductor quantum dots. *Phys. Rev. X*, 8:041050, Dec 2018.

[92] Y. Arakawa and H. Sakaki. Multidimensional quantum well laser and temperature dependence of its threshold current. *Applied Physics Letters*, 40(11):939–941, 1982.

[93] S. Fafard, K. Hinzer, S. Raymond, M. Dion, J. McCaffrey, Y. Feng, and S. Charbonneau. Red-emitting semiconductor quantum dot lasers. *Science*, 274:1350, 1996.

[94] D. Bimberg, M. Grundmann, F. Heinrichsdorff, N.N. Ledentsov, V.M. Ustinov, A.E. Zhukov, A.R. Kovsh, M.V. Maximov, Y.M. Shernyakov, B.V. Volovik, A.F. Tsatsul'nikov, P.S. Kop'ev, and Zh.I. Alferov. Quantum dot lasers: breakthrough in optoelectronics. *Thin Solid Films*, 367(1):235–249, 2000.

[95] M. P. van Kouwen, M. H. M. van Weert, M. E. Reimer, N. Akopian, U. Perinetti, R. E. Algra, E. P. A. M. Bakkers, L. P. Kouwenhoven, and V. Zwiller. Single quantum dot nanowire photodetectors. *Appl. Phys. Lett.*, 97:113108, 2010.

[96] B. Aslan, H. C. Liu, M. Korkusinski, S.-J. Cheng, and P. Hawrylak. Response spectra from mid- to far-infrared, polarization behaviors, and effects of electron numbers in quantum-dot photodetectors. *Applied Physics Letters*, 82(4):630–632, 2003.

[97] Mikael T. Björk, Claes Thelander, Adam E. Hansen, Linus E. Jensen, Magnus W. Larsson, L. Reine Wallenberg, and Lars Samuelson. Few-electron quantum dots in nanowires. *Nano Letters*, 4(9):1621–1625, 2004.

[98] Maarten P. van Kouwen, Michael E. Reimer, Anne W. Hidma, Maarten H. M. van Weert, Rienk E. Algra, Erik P. A. M. Bakkers, Leo P. Kouwenhoven, and Val Zwiller. Single electron charging in optically active nanowire quantum dots. *Nano Letters*, 10(5):1817–1822, 2010.

[99] Arkadiusz Wojs and Pawel Hawrylak. Charging and infrared spectroscopy of self-assembled quantum dots in a magnetic field. *Phys. Rev. B*, 53:10841–10845, Apr 1996.

[100] Arkadiusz Wojs and Pawel Hawrylak. Theory of photoluminescence from modulation-doped self-assembled quantum dots in a magnetic field. *Phys. Rev. B*, 55:13066–13071, May 1997.

[101] M. Ediger, G. Bester, A. Badolato, P. M. Petroff, K. Karrai, A. Zunger, and R. J. Warburton. Peculiar many-body effects revealed in the spectroscopy of highly charged quantum dots. *Nat. Phys.*, 3:774–779, 2007.

[102] Gustavo A. Narvaez and Pawel Hawrylak. Effects of electron-electron interactions on excitonic absorption in charged self-assembled quantum dots. *Phys. Rev. B*, 61:13753–13762, May 2000.

[103] Massimo Rontani, Fausto Rossi, Franca Manghi, and Elisa Molinari. Multiple quantum phases in artificial double-dot molecules. *Solid State Communications*, 3:151, Apr 1999.

[104] L P Kouwenhoven, D G Austing, and S Tarucha. Few-electron quantum dots. *Reports on Progress in Physics*, 64(6):701–736, may 2001.

[105] P. Hawrylak. Excitonic artificial atoms: Engineering optical properties of quantum dots. *Phys. Rev. B*, 60:5597–5608, 1999.

[106] S. Raymond, S. Studenikin, A. Sachrajda, Z. Wasilewski, S. J. Cheng, W. Sheng, P. Hawrylak, A. Babinski, M. Potemski, G. Ortner, and M. Bayer. Excitonic energy shell structure of self-assembled ingaas gaas quantum dots. *Phys. Rev. Lett.*, 92:187402, May 2004.

[107] M. Bayer, P. Hawrylak, K. Hinzer, S. Fafard, M. Korkusinski, Z. R. Wasilewski, O. Stern, and A. Forchel. Coupling and entangling of quantum states in quantum dot molecules. *Science*, 291(5503):451–453, 2001.

[108] Juan José Palacios and Pawel Hawrylak. Correlated few-electron states in vertical double-quantum-dot systems. *Phys. Rev. B*, 51:1769–1777, Jan 1995.

[109] Marek Korkusiński and Pawel Hawrylak. Electronic structure of vertically stacked self-assembled quantum disks. *Phys. Rev. B*, 63:195311, Apr 2001.

[110] Weidong Sheng and Pawel Hawrylak. Atomistic theory of electronic and optical properties of InAsInP self-assembled quantum dots on patterned substrates. *Phys. Rev. B*, 72:035326, Jul 2005.

[111] Moritz Cygorek, Matthew Otten, Marek Korkusinski, and Pawel Hawrylak. Accurate and efficient description of interacting carriers in quantum nanostructures by selected configuration interaction and perturbation theory. *Phys. Rev. B*, 101:205308, May 2020.

[112] C. Delerue, M. Lannoo, and G. Allan. Concept of dielectric constant for nanosized systems. *Phys. Rev. B*, 68:115411, Sep 2003.

[113] Iwan Moreels, Guy Allan, Bram De Geyter, Ludger Wirtz, Christophe Delerue, and Zeger Hens. Dielectric function of colloidal lead chalcogenide quantum dots

obtained by a kramers-krönig analysis of the absorbance spectrum. *Phys. Rev. B*, 81:235319, Jun 2010.

[114] A. Kogan, G. Granger, M. A. Kastner, D. Goldhaber-Gordon, and Hadas Shtrikman. Singlet–triplet transition in a single-electron transistor at zero magnetic field. *Phys. Rev. B*, 67:113309, Mar 2003.

[115] F. Simmel, David Abusch-Magder, D. A. Wharam, M. A. Kastner, and J. P. Kotthaus. Statistics of the coulomb-blockade peak spacings of a silicon quantum dot. *Phys. Rev. B*, 59:R10441–R10444, Apr 1999.

[116] Irene Puerto Gimenez, Marek Korkusinski, and Pawel Hawrylak. Linear combination of harmonic orbitals and configuration interaction method for the voltage control of exchange interaction in gated lateral quantum dot networks. *Phys. Rev. B*, 76:075336, Aug 2007.

[117] M. F. Doty, J. I. Climente, M. Korkusinski, M. Scheibner, A. S. Bracker, P. Hawrylak, and D. Gammon. Antibonding ground states in inas quantum-dot molecules. *Phys. Rev. Lett.*, 102:047401, Jan 2009.

[118] Błażej Jaworowski. *Electron correlations in topological flat bands*. Ph.D. thesis, Wrocław University of Science and Technology, September 2018.

[119] O. Benson. *Semiconductor Quantum Bits*, chapter 1, pages 3–32. Pan Stanford Publishing, 2008.

[120] Adam Alfieri, Surendra B. Anantharaman, Huiqin Zhang, and Deep Jariwala. Nanomaterials for quantum information science and engineering. *Advanced Materials*, page 2109621, 2022.

[121] Christoph Kloeffel and Daniel Loss. Prospects for spin-based quantum computing in quantum dots. *Annual Review of Condensed Matter Physics*, 4(1):51–81, 2013.

[122] T. E. Northup and R. Blatt. Quantum information transfer using photons. *Nature Photonics*, 8(5):356–363, May 2014.

[123] Takashi Kobayashi, Joseph Salfi, Cassandra Chua, Joost van der Heijden, Matthew G. House, Dimitrie Culcer, Wayne D. Hutchison, Brett C. Johnson, Jeff C. McCallum, Helge Riemann, Nikolay V. Abrosimov, Peter Becker, Hans-Joachim Pohl, Michelle Y. Simmons, and Sven Rogge. Engineering long spin coherence times of spin–orbit qubits in silicon. *Nature Materials*, 20(1):38–42, Jan 2021.

[124] F. H. L. Koppens, C. Buizert, K. J. Tielrooij, I. T. Vink, K. C. Nowack, T. Meunier, L. P. Kouwenhoven, and L. M. K. Vandersypen. Driven coherent oscillations of a single electron spin in a quantum dot. *Nature*, 442(7104):766–771, Aug 2006.

[125] A. H. Myerson, D. J. Szwer, S. C. Webster, D. T. C. Allcock, M. J. Curtis, G. Imreh, J. A. Sherman, D. N. Stacey, A. M. Steane, and D. M. Lucas. High-fidelity readout of trapped-ion qubits. *Phys. Rev. Lett.*, 100:200502, May 2008.

[126] F Hassler, A R Akhmerov, and C W J Beenakker. The top-transmon: a hybrid superconducting qubit for parity-protected quantum computation. *New Journal of Physics*, 13(9):095004, sep 2011.

[127] Ana Martin, Bruno Candelas, Ángel Rodríguez-Rozas, José D. Martín-Guerrero, Xi Chen, Lucas Lamata, Román Orús, Enrique Solano, and Mikel Sanz. Toward pricing financial derivatives with an ibm quantum computer. *Phys. Rev. Research*, 3:013167, Feb 2021.

[128] Jay D. Sau and S. Das Sarma. Realizing a robust practical majorana chain in a quantum-dot-superconductor linear array. *Nature Communications*, 3(1):964, Jul 2012.

[129] R. M. Lutchyn, E. P. A. M. Bakkers, L. P. Kouwenhoven, P. Krogstrup, C. M. Marcus, and Y. Oreg. Majorana zero modes in superconductor–semiconductor heterostructures. *Nature Reviews Materials*, 3(5):52–68, May 2018.

[130] F.D.M. Haldane. Continuum dynamics of the 1-d heisenberg antiferromagnet: Identification with the o(3) nonlinear sigma model. *Physics Letters A*, 93(9):464–468, 1983.

[131] Yun-Pil Shim, Anand Sharma, Chang-Yu Hsieh, and Pawel Hawrylak. Artificial haldane gap material on a semiconductor chip. *Solid State Comm*, 150:2065, 2010.

[132] Alev Devrim Guclu, Pawel Potasz, Marek Korkusinski, and Pawel Hawrylak. *Graphene Quantum Dots*. Springer Berlin, Heidelberg, 2014.

[133] Shantanu Mishra, Gonçalo Catarina, Fupeng Wu, Ricardo Ortiz, David Jacob, Kristjan Eimre, Ji Ma, Carlo A. Pignedoli, Xinliang Feng, Pascal Ruffieux, Joaquín Fernández-Rossier, and Roman Fasel. Observation of fractional edge excitations in nanographene spin chains. *Nature*, 598(7880):287–292, Oct 2021.

[134] G. Catarina and J. Fernández-Rossier. Hubbard model for spin-1 haldane chains. *Phys. Rev. B*, 105:L081116, Feb 2022.

[135] F. Verstraete, D. Porras, and J. I. Cirac. Density matrix renormalization group and periodic boundary conditions: A quantum information perspective. *Phys. Rev. Lett.*, 93:227205, Nov 2004.

[136] Matthew Fishman, Steven R. White, and E. Miles Stoudenmire. The ITensor software library for tensor network calculations, 2020.

[137] Jacob Manalo and Daniel Miravet. Python matrix product states dmrg tool, 2021.

[138] Błażej Jaworowski. *Electron correlations in topological flat bands*. PhD thesis, Wroclaw University of Science and Technology, 2018.

[139] Nicolás Morales-Durán, Nai Chao Hu, Pawel Potasz, and Allan H. MacDonald. Nonlocal interactions in moiré hubbard systems. *Phys. Rev. Lett.*, 128:217202, May 2022.

[140] S M Girvin and Daniel P Arovas. Hidden topological order in integer quantum spin chains. *Physica Scripta*, T27:156–159, jan 1989.